



UNIVERSITY
OF OSLO

Master's thesis

Gravitational waves from topological defects

Signatures of late-time first-order phase transitions

Nanna Bryne

Computational Science: Astrophysics
60 ECTS study points

Institute of Theoretical Astrophysics, Department of Physics
Faculty of Mathematics and Natural Sciences

Autumn 2024



Nanna Bryne

Gravitational waves from topological defects

Signatures of late-time first-order phase transitions

Supervisor:
David Fonseca Mota

Abstract

Topological defects predicted by extensions of general relativity can manifest in gravitational-wave observations on Earth. As a working example, we present symmetron domain walls formed at redshift ~ 2 with structural ripples and investigate how gravitational radiation carries information about the symmetry-breaking theory. Future broadband gravitational-wave observations **COMPLETE THIS!**

Contents

Preface	ix
Notation	xi
1 Introduction	1
1.1 Overview	2
1.1.1 Key literature	3
1.2 Preliminaries	3
1.2.1 Special relativity	3
1.2.2 Classical field theory	4
1.2.3 Mathematical tools	4
1.2.4 Cosmic chronology	5
1.2.5 Cosmological simulations	5
I Background	7
2 General Relativity	9
2.1 Differential geometry	9
2.1.1 Hypersurfaces	10
2.1.2 Conformal geometry	11
2.2 Einstein's equation	12
2.2.1 Energy–momentum tensor	12
2.2.2 Linearised gravity	13
2.3 Modern cosmology	14
2.3.1 Cosmological perturbation theory	15
2.4 Gravitational waves	15
2.4.1 Expanding universe	16
3 Symmetry-Breaking Dark Energy	19
3.1 Cosmological defects	19
3.1.1 Example: (stationary) \mathbb{Z}_2 kinks	20
3.1.2 Domain walls	21
3.1.3 Defect formation	21
3.2 TITLE (Quintessence/Scalar field theories)	22
3.2.1 General framework	22
3.2.2 Asymmetron model	24
3.3 Classification of topological defects	25

II	Methodology	27
4	Imperfect Defects	29
4.1	Formal treatment of defect dynamics	29
4.1.1	Linearised perturbations	31
4.1.2	Energy and momentum	31
4.2	Domain wall dynamics	31
4.2.1	Planar walls in expanding spacetime	32
4.2.2	Time-dependent surface tension	33
4.3	Symmetron walls	33
4.3.1	Solution in matter-dominated universe	34
4.3.2	TITLE (Review)	35
4.4	From domain wall wiggles to spacetime ripples	35
4.4.1	Gravitational waves in expanding universe	36
4.4.2	Fourier-space stress–energy tensor	36
5	Cosmic Phase Transitions	39
5.1	\mathbb{Z}_2 symmetry-break	39
5.1.1	Quasi-static limit	40
5.1.2	Asymptotic limit	40
5.2	Dynamic modelling	41
5.2.1	Equations	41
5.3	TITLE (Toy model design)	42
5.3.1	Initial configuration	42
5.3.2	Energy and momentum	43
5.3.3	Ripples in matter-dominated spacetime	44
5.3.4	Code output and interpretation	45
5.4	Simulation setups	45
5.4.1	Catalogue	46
III	Findings	49
6	TITLE (Toy Model Trials)	51
6.1	Symmetron field	51
6.1.1	Holistic review	53
6.2	Domain wall dynamics	53
6.2.1	Holistic review	55
6.3	Gravitational waves	56
6.3.1	Gravitational radiation	57
6.3.2	Comparison with analytical results	57
6.3.3	Holistic review	59
6.4	Hindsight	61
7	TITLE (Ifs, buts and maybes)	63
7.1	Project reflection	63
7.1.1	Open questions	63
7.1.2	Flat-space analogy	64
7.1.3	Continued assessment	64
7.2	Limitations and possibilities	65
7.2.1	Improvements	66

Summary	69
8 Conclusion and Outlook	71
8.1 Applications.	71
8.2 Future work.	71
Bibliography	80
 Appendices	 81
A TITLE (Cylinder Functions)	83
A.1 Explicit formulas	84
A.1.1 Integer order	84
A.1.2 Half-integer order	84
A.2 Properties	84
A.2.1 Some notable identities	84
A.2.2 Asymptotic behaviour	85
B Derivations.	87
B.1 Linearised gravity	87
B.2 Surface tension of thin domain walls	87
B.2.1 Symmetron example	87
B.2.2 Adjusting the boundaries	87
B.3 Variation of Nambu–Goto action	88
B.3.1 Stress–energy tensor	88
B.4 Fourier space stress–energy tensor: sinusoidal	89
C TITLE (Stable Symmetron)	91
C.1 Idealised path	91
C.1.1 Optimal path	92
C.2 Field initialisation.	92

Contents

List of Figures

1.1	Sensitivity curves for present and future gravitational-wave experiments, created with gwplotter.com (November 2024). The black curves represent the characteristic strain of present detectors European Pulsar Timing Arrays (EPTA), Laser Interferometer Gravitational-wave Observatory (LIGO) and Advanced LIGO O1 (aLIGO (O1)), and future detectors Square Kilometer Array (SKA), evolving Laser Interferometer Space Antenna (eLISA), Decihertz Interferometer Gravitational-wave Observatory (DECIGO), aLIGO design (aLIGO), Einstein Telescope (ET) and Cosmic Explorer (CE).	1
3.1	Demonstration of the \mathbb{Z}_2 kink and its energy content for $\eta = 1$ and $\lambda = 2$. The green dotted graph is a Gaussian around $x = x_0$ with standard deviation $w/\sqrt{2}$. Inspiration from Vachaspati [35].	21
3.2	The evolution of the (a)symmetron effective potential in (dashed red) solid blue. Describe time. IF TIME: ADD TWO BALLS.	24
3.3	Schematic of the symmetron screening mechanism. It is clear that the vacuum expectation value goes to zero in dense regions. This example assumes a symmetron with Compton length scale $L_c \sim \mathcal{O}(\text{kpc})$ [7]. Illustration based on Christiansen [9].	25
4.1	Schematic demonstrating how the analytical solution to the equation of motion for $\varepsilon(s)$. The numerical solution is included, both in the case with constant (“naive”) and time-varying (numerical) surface tension.	36
5.1	Demonstration of the periodicity of $\chi(a_i, z)$ on the lattice. The shaded region represents the box coordinates.	43
5.2	Visual representation of initial configurations listed in Table 5.1.	46
6.1	The evolution of the symmetron field in the asymptotic limit. The symmetron parameters are the fiducial ones. The simulation results are from the simulation with no walls. We see χ_+ in solid grey, $\check{\chi}_{\text{opt.}}$ in solid blue, $\langle \check{\chi} \rangle$ in solid red and $\check{\chi}^{\text{ideal}}$ in dashed yellow.	51
6.2	Background quantities. Not too happy about this plot... FIX LABELS!	52
6.3	The asymptotic symmetron field $\check{\chi}$ and its time derivative $\dot{\check{\chi}}$	53
6.4	Demonstration of the interpretation of the results from simulation 1.	54
6.5	Functions of the scaled time parameter $t_\omega = \omega(s-1) = p(\tau-\tau_*)$. <i>Top panel:</i> The wall extremal position normalised to the initial amplitude, $e = \varepsilon/\varepsilon_*$. <i>Bottom panel:</i> The absolute difference between the wall position from calculations and simulations, $\Delta e = \varepsilon^{\text{NG}} - \varepsilon^\phi /\varepsilon_*$	55

List of Figures

- 6.6 The box-averaged gravitational wave radiation, normalised to the critical density today. Note the logarithmic y -axes. *Left panel:* ρ_{gw} as function of $s = \tau/\tau_*$. *Right panel:* ρ_{gw} as function of $t_\omega = \omega(s - 1) = p(\tau - \tau_*)$ 57
- 6.7 Monochromatic plus-waves evolving over conformal time $s = \tau/\tau_*$, normalised to unity. The lower right panel is explanatory for all panels: Green dash-dotted graphs represent \tilde{h}_+^{NG} , orange solid ones represent \tilde{h}_+^ϕ and in blue are \tilde{h}_+ . The wave vector is given in the lower left corner of each plot, as (v, w) . The secondary above x -axis represents scaled time $t_\omega = p(\tau - \tau_*)$ 59
- 6.8 The one-dimensional power spectrum as functions of angle ϑ , in arbitrary units. Green dash-dotted graphs represent \tilde{h}_+^{NG} , orange solid ones represent \tilde{h}_+^ϕ and in blue are \tilde{h}_+ 60

Preface

Here comes your preface, including acknowledgments and thanks.

Notation

Constants and units

We use natural units where the speed of light in vacuum is $c = 1$ and the reduced Planck mass is $M_{\text{Pl}} = 1/\sqrt{8\pi G_N} = 1$. G_N is the Newtonian constant of gravitation. Comoving lengths are usually given in units of megaparsec per Hubble constant Mpc/h_0 , where $1 \text{ pc} = 3.26156 \text{ light-years}$.

Tensors

Indices. Greek indices run from 0 to N , and Latin i, j, k, \dots from 1 to N , in an $(N + 1)$ -dimensional spacetime. Indices a, b, c are reserved for auxiliary coordinate systems. We adopt Einstein's summing convention in which repeated indices are summed over, e.g. $x^\mu x_\mu = \sum_{\mu=0}^N x^\mu x_\mu$.

Metric. The metric signature $(-, +, \dots, +)$ is considered. The Minkowski metric is denoted $\eta_{\mu\nu}$, whereas a general metric is denoted $g_{\mu\nu}$. The metric raises and lowers indices of tensors, e.g. $x^\mu = g^{\mu\nu} x_\nu$.

Derivatives. We sometimes adopt the comma-notation for partial derivatives ∂_μ and covariant derivatives ∇_μ . For a scalar ϕ , we have:

$$\phi_{,\mu} \equiv \partial_\mu \phi = \frac{\partial \phi}{\partial x^\mu} = (\partial_0, \partial_i), \quad (1a)$$

$$\phi_{;\mu} \equiv \nabla_\mu \phi = \partial_\mu \phi. \quad (1b)$$

The d'Alembertian reads

$$\square \phi = \nabla^\mu \nabla_\mu \phi = \frac{1}{\sqrt{-g}} \partial_\mu (\sqrt{-g} \partial^\mu \phi), \quad (2)$$

and we use $\square_M \equiv \partial^\mu \partial_\mu$ to specify the Minkowski box operator.

Miscellanea. We make use of the notation

$$T_{(\mu\nu)} \equiv \frac{1}{2} (T_{\mu\nu} + T_{\nu\mu}), \quad (3a)$$

$$T_{[\mu\nu]} \equiv \frac{1}{2} (T_{\mu\nu} - T_{\nu\mu}). \quad (3b)$$

We write $T_{\mu\nu} = T_{(\mu\nu)} + T_{[\mu\nu]}$.

Special symbols and tensors. The Kronecker delta is defined as

$$\delta_{ij} = \begin{cases} 1 & \text{if } i = j, \\ 0 & \text{else.} \end{cases} \quad (4)$$

The Christoffel symbols (also called connection coefficients) are given by

$$\Gamma_{\mu\nu}^{\rho} = \frac{1}{2} g^{\rho\sigma} (g_{\mu\sigma,\nu} + g_{\mu\sigma,\nu} - g_{\mu\nu,\sigma}). \quad (5)$$

The Riemann curvature tensor is

$$\mathcal{R}^{\rho}{}_{\sigma\mu\nu} = \partial_{\mu}\Gamma_{\nu\sigma}^{\rho} - \partial_{\nu}\Gamma_{\mu\sigma}^{\rho} + \Gamma_{\mu\lambda}^{\rho}\Gamma_{\nu\sigma}^{\lambda} - \Gamma_{\nu\lambda}^{\rho}\Gamma_{\mu\sigma}^{\lambda}. \quad (6)$$

We express the *Lambda tensor*—sometimes called the “projection operator” or “spin-2 operator”—that projects a symmetric tensor onto the TT gauge as

$$\Lambda_{ij}^{kl}(\mathbf{k}) = P_i^k(\mathbf{k})P_j^l(\mathbf{k}) - \frac{1}{2}P_{ij}(\mathbf{k})P^{kl}(\mathbf{k}); \quad P_{ij}(\mathbf{k}) = \delta_{ij} - k_i k_j / k^2, \quad (7)$$

where \mathbf{k} is the propagation direction (see Section 2.4).

Fourier transforms

We use the following convention for the Fourier transform of $f(x)$, $\tilde{f}(k)$, and its inverse, where x and k are Lorentz four-vectors:

$$\begin{aligned} f(x) &= \int \frac{d^4k}{(2\pi)^4} e^{-ik \cdot x} \tilde{f}(k), \\ \tilde{f}(k) &= \int d^4x e^{ik \cdot x} f(x). \end{aligned} \quad (8)$$

Here, $k \cdot x = k_{\sigma} x^{\sigma} = g_{\rho\sigma} k^{\rho} x^{\sigma}$.

Special functions

「Will fix this.」 We will denote various cylinder functions by **blah blah** [...] see Appendix A

regular Bessel functions: Z ; $Z_{\nu}^{(i)}(x)$

spherical Bessel functions: z ; $z_n^{(i)}(x) = \sqrt{\pi/(2x)} Z_{n+1/2}^{(i)}(x)$

Riccati–Bessel functions: R ; $R_n^{(i)}(x) = -(-1)^i \cdot x Z_n^{(i)}(x)$

Here, $\nu \in \mathbb{C}$ and $n \in \mathbb{Z}$ denotes order, while $i = 1, 2$ refers to the *ith kind*. **Too messy!**

Acronyms

CDM	<i>cold dark matter</i>
CMB	<i>cosmic microwave background</i> [radiation]
DFT	<i>discrete Fourier transform</i>
F(L)RW	<i>Friedmann(–Lemaître)–Robertson–Walker</i> [metric]
GR	<i>general relativity</i>
HPC	<i>high performance computing</i>
MPI	<i>Message Passing Interface</i>
NG	<i>Nambu–Goto</i> [action]
ODE	<i>ordinary differential equation</i>
PDE	<i>partial differential equation</i>
PT	<i>phase transition</i>
PTA	<i>pulsar timing arrays</i>
SE	<i>stress–energy</i> [tensor]
SR	<i>special relativity</i>
(S)SB	<i>(spontaneous) symmetry breaking</i>
TT	<i>transverse–traceless</i> [gauge]
VEV	<i>vacuum expectation value</i>
Λ CDM	<i>Lambda (Λ) cold dark matter model; standard model of cosmology</i>

Nomenclature

Some title	
<i>Constants</i> 「SORT!」	
G_N	Newton’s gravitation constant.
M_{Pl}	Reduced Planck mass $1/\sqrt{8\pi G_N}$.
<i>Background physics</i>	
a	Scale factor.
τ	Conformal time.
$\dot{}$	Conformal time derivative $d/d\tau$.
\mathcal{H}	Conformal Hubble factor \dot{a}/a .
z	Cosmic redshift.
α	Exponent blah blah [...]
$\eta_{\mu\nu}$	Metric tensor, Minkowski.
$g_{\mu\nu}$	Metric tensor, FLRW.
\mathbf{x}	Comoving coordinate (x, y, z) .
\mathbf{k}	Comoving wavevector (k_x, k_y, k_z) .
\mathcal{M}	Riemannian manifold.
$\mathcal{R}_{\mu\nu}$	Ricci tensor.
$\mathcal{G}_{\mu\nu}$	Einstein tensor.
\vdots	\vdots
Some title	
\vdots	\vdots
\vdots	\vdots
\vdots	\vdots
\mathbb{Z}_n	Symmetry XXX.
\vdots	\vdots
\vdots	\vdots
ν	Time variable $(a_*/a)^{3\alpha}$.
s	Dimensionless conformal time τ/τ_*
<i>Subscripts</i>	
m	Non-relativistic matter.
0	Today ($a_0 = 1$ is the scale factor today).
*	Time of phase transition.

Table 1: Variables **blah blah [...]**

Chapter 1

Introduction

From the first gravitational-wave observation by the ground-based Laser Interferometer Gravitational-wave Observatory (LIGO) in 2015 [1], and until the detection of stochastic nHz-frequency gravitational waves by the North American Nanohertz Observatory for Gravitational Waves (NANOGrav) released in 2023 [4], astrophysical sources have been the primary focus of the community [26]. The latter pulsar timing array (PTA) data (called *NANOGrav 15 yr*) allows for cosmological scales, and together with other planned gravitational-wave experiments has the potential of probing new physics. Figure 1.1 illustrates relations between detector sensitivities, bandwidths and gravitational sources.

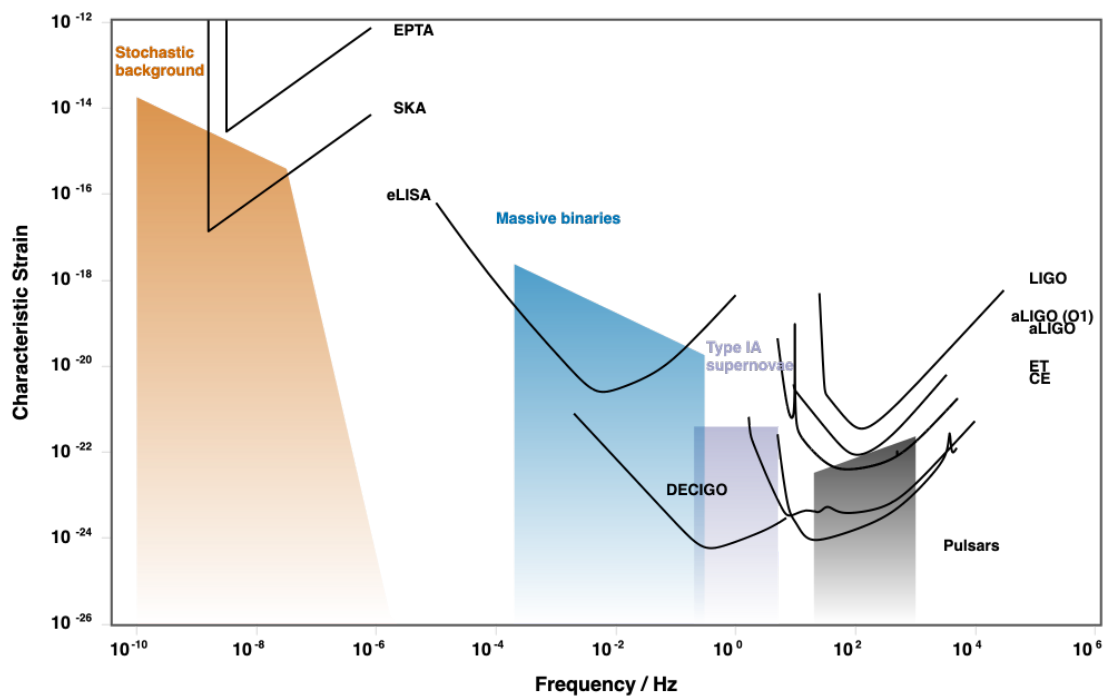


Figure 1.1: Sensitivity curves for present and future gravitational-wave experiments, created with gwplotter.com (November 2024). The black curves represent the characteristic strain of present detectors European Pulsar Timing Arrays (EPTA), Laser Interferometer Gravitational-wave Observatory (LIGO) and Advanced LIGO O1 (aLIGO (O1)), and future detectors Square Kilometer Array (SKA), evolving Laser Interferometer Space Antenna (eLISA), Deci-hertz Interferometer Gravitational-wave Observatory (DECIGO), aLIGO design (aLIGO), Einstein Telescope (ET) and Cosmic Explorer (CE).

Speculative topological defects in cosmology are generally remnants of phase transitions and

potential sources of gravitational waves [11, 33]. Dynamical ranges of cosmological simulations are limited, so resolving broad-frequency gravitational-wave spectra computationally is challenging [33]. This calls for novel analytical analyses of dynamics and gravitational-wave signals of candidate sources of a stochastic gravitational wave background (GWB). This search for cosmological gravitational waves can have great implications for both high-energy physics and cosmology alike, and even non-observations can help constrain beyond-standard model particle-physics models [24].

Nanohertz frequencies today correspond to the horizon size in the early, very hot (temperature $\mathcal{O}(10^{12} \text{ K})$) universe [11]. Therefore, high-energy phase transitions, argued to manifest in these frequencies, has been interest of recent studies [5, 26, 33]. It is claimed [3] that *NANOGrav 15 yr* [4] can constrain domain wall models. Babichev et al. [5] show that gravitational waves from melting domain walls—walls with time-dependent surface tension—show characteristics consistent with *NANOGrav 15 yr* [4].

In this work we put emphasis on theoretical aspects of domain-wall formation in late-time phase transitions following Christiansen et al. [11, 12]. Cosmic domain walls are defects predicted by discrete symmetry-breaking scalar field theories such as the symmetron model [21]. Their dynamics is well-understood in idealised scenarios [6, 18, 19, 22, 35], but self-contained, rigorous analytical frameworks connecting properties of topological defects and gravitational waves are lacking [33]. One of the aims of this thesis is to test the limits of the analytical solvability of such toy scenarios and discuss its potential as substitute for computationally expensive simulations.

We will use mathematics (topology and geometry) and physics (general relativity and cosmology) to study the dynamics of topological defects and to compute tensor perturbations sourced by infinitely thin, planar domain walls. Similar works [6, 18, 22] explore the thin-wall approximation when the energy density is constant, and most thoroughly analysed are walls in Minkowski space. Extensions to non-thin walls has also been considered [13].

This work concludes in a framework that describes the motion of a small perturbation to the normal coordinate of a planar domain wall in a matter-dominated universe, with possibility for generalisation. The model assumes the symmetron potential, but this is easily changed to another scalar field model with discrete symmetry by changing the surface tension. The equations are tested by comparison to toy scenarios in cosmological simulations using *gevolution* [2]. The final part—the resulting tensor perturbations to the metric—has room for improvement, or at least needs to be better tested more thoroughly against simulations. The pattern detected in simulations do resemble that of the analytical model, but there are also large deviations between the results.

Thesis outline. The thesis is divided into three main parts. Part I presents the relevant background theory, including concepts from differential geometry and topological defects. In Part II we describe how the framework was designed and the way it is to be tested in simulations. Finally, in Part III we present the results from simulations and calculations, with comparisons and discussions. Prior to all of this, we describe some basic concepts in the coming sections.

1.1 Overview

General relativity (GR) is a fundamental theory of gravitation proposed by Albert Einstein (1979–1955) in 1915. It describes gravity not as a force, but as a curvature of spacetime caused by mass and energy, fundamentally altering our understanding of both space and time. The theory is supported by numerous experiments and observations, such as the bending of light

around massive objects (gravitational lensing) and the precise orbit of Mercury. Additionally, GR is essential for the accurate functioning of the Global Positioning System (GPS), as it allows for the necessary corrections to account for the differences in the passage of time between satellites in orbit and receivers on Earth. Special relativity (SR)—proposed by the same physicist in 1905—is understood as a special case of GR where the background spacetime is Minkowski.

In cosmology, GR forms the backbone of our understanding of the universe on large scales. The theory predicts the expanding universe, which has been confirmed by the redshift observations of distant galaxies, leading to the development of the Big Bang theory. GR also accounts for the formation of large-scale structures like galaxies and galaxy clusters, and provides the framework for understanding cosmic phenomena such as black holes and gravitational waves. The solutions to Einstein’s field equations under various conditions have led to a rich set of predictions and observations, including the cosmic microwave background radiation (CMB), which is a relic from the early universe and a critical piece of evidence supporting the Big Bang model.

The standard model of cosmology is the Lambda cold dark matter model (Λ CDM) that postulates the existence of a cosmological constant (Λ), widely used synonymously with dark energy, and cold dark matter (CDM), besides normal matter. Dark energy is used to explain the contemporary accelerated expansion of the universe, whereas dark matter accounts for the observed gravitational effects that ordinary matter alone cannot elucidate.

Besides the explanation of dark matter and dark energy, there are other shortcomings to these theories. Of most cosmological relevance are the smallness (“vacuum catastrophe”) and coincidence problems associated with the cosmological constant, as well as the Hubble tension (Section 2.3). We will address some of these in this thesis.

Amongst the more popular strategies to overcome the problems of modern cosmology, is to add extra degrees of freedom. Speculative scalar fields that possess certain symmetries tend to predict phase transitions, which in turn can produce topological defects. **Two–three sentences about domain walls.**

1.1.1 Key literature

Let us mention a few foundational works that have been instrumental in shaping the theoretical and methodological approach in this project. *Spacetime and Geometry* by Carroll (2019) is the baseline for the majority of the differential-geometry analyses and GR discussions. A large part of the gravitational-wave discussion is inspired by *Gravitational Waves* volumes 1 and 2 by Maggiore (2007, 2018). *Kinks and Domain Walls* by Vachaspati (2006) provide the basis for our understanding of topological defects.

1.2 Preliminaries

We assume that the reader is familiar with basic concepts from mathematical methods in physics such as the variational principle, tensors, Green’s functions and cylindrical functions. Classical field theory and linear perturbation theory will not be covered from ground level. Other than this, the thesis will be relatively self-contained, but understanding of basic modern cosmology will be an advantage. For reference, we cover a few of these concepts in the subsections below.

1.2.1 Special relativity

The **four-vector** $x^\mu = (t, \mathbf{x})$ in Minkowski space $\mathbb{R}^{3,1}$ encompasses time $t = x^0$ and position $\mathbf{x} = x^i = (x^1, x^2, x^3)$. The **metric tensor** in SR is $g_{\mu\nu} = \eta_{\mu\nu} \equiv \text{diag}(-1, +1, +1, +1)$. The

four-vector x^μ is “naturally raised,” whereas the derivative

$$\partial_\mu \equiv \frac{\partial}{\partial x^\mu} = \left(\frac{\partial}{\partial t}, \nabla \right) \quad (1.1)$$

is “naturally lowered.” **「Lorentz invariance.」**

1.2.2 Classical field theory

We formulate a theory of fields $\Phi(x)$ in four-dimensional Minkowski spacetime in terms of the Lorentz invariant action

$$S = \int d^4x \mathcal{L}(\Phi, \partial_\mu \Phi), \quad (1.2)$$

with \mathcal{L} being the *Lagrangian density* of the theory, a function of the set of fields Φ and its first derivatives. We will refer to \mathcal{L} simply as the Lagrangian, as is customary when working with fields.

This translates to a general (i.e. curved) spacetime through the construction of a Lorentz-invariant Lagrangian,

$$S = \int d^4x \underbrace{\mathcal{L}(\Phi, \nabla_\mu \Phi)}_{\text{not scalar}} = \int \underbrace{d^4x \sqrt{-g}}_{\text{scalar}} \underbrace{\hat{\mathcal{L}}(\Phi, \nabla_\mu \Phi)}_{\text{scalar}}, \quad (1.3)$$

where $g = \det(g)$ is the determinant of the metric. What was applied here, was the **minimal-coupling principle**, and we may refer to \mathcal{L} as the minimally-coupled Lagrangian (density). Loosely speaking, this principle involves replacing the Minkowski metric with the curved-spacetime metric ($\eta_{\mu\nu} \rightarrow g_{\mu\nu}$), and partial derivatives to covariant derivatives ($\partial_\mu \rightarrow \nabla_\mu$).

Action principle. We use variational calculus to obtain the fields’ equations of motion. For a scalar field ϕ , we consider the change $\phi \rightarrow \phi + \delta\phi$ and apply this to the action, s.t. $S \rightarrow S + \delta S$. After isolating S and gathering terms up to leading order, we set $\delta S = 0$ and obtain an equation for ϕ in terms of first and second derivatives.

Often it is necessary to use **「Stokes’ theorem」**, to set certain terms to zero. The argument **blah blah [...]** **「Fix or remove!」**

Newtonian gravity

blah blah [...]

1.2.3 Mathematical tools

Perturbation theory

We write that to order o in some small parameter ϵ , we have

$$\dot{q} \equiv \sum_{i=0}^o \delta^{(i)} q = q^{(0)} + \epsilon q^{(1)} + \epsilon^2 q^{(2)} + \cdots + \epsilon^o q^{(o)}, \quad (1.4)$$

where

Consider $Q(q)$. We write

$$\dot{Q} \equiv \sum_{i=0}^o {}^{(i)}Q, \quad (1.5)$$

where ${}^{(i)}Q$ is the i th order perturbation of Q , not necessarily $\epsilon^i Q$

「Fix or remove.」

Method of Green's functions

A linear ordinary differential equation (ODE) $L_x f(x) = g(x)$ assumes a linear differential operator L , a 「continuous」⁷, unknown function f , and a right-hand side g that forms the inhomogeneous part of the ODE. The **Green's function** G for the ODE (or L) manifests as any solution to $L_x G(x, y) = \delta(x - y)$. Now

$$f(x) = \int dy G(x, y)g(y) \quad (1.6)$$

solves the original ODE.

DELETE ME: (If L is translation invariant (invariant under $x \mapsto x + a$)—which is equivalent to L having constant coefficients—we can write $G(x, y) = G(x - y)$ and

$$f(x) = (G * g)(x) = \int dy G(x - y)g(y) \quad (1.7)$$

solves $L_x f(x) = g(x)$. >

DELETE ME: (Let $f_i^{(0)}$, $i = 1, 2, 3, \dots$ be solutions to the homogeneous ODE, i.e. $L_x f_i^{(0)} = 0$. Then, by the superposition principle, $f(x) + \sum_i c_i f_i^{(0)}$ is also a solution of the original, inhomogeneous equation.)

DELETE ME: <

Pulse signal. Consider the very common scenario where the source is a temporary pulse;

$$g(x) = \begin{cases} g(x), & x_0 \leq x \leq x_1, \\ 0, & x \geq x_1. \end{cases} \quad (1.8)$$

>

「Fix or remove.」

1.2.4 Cosmic chronology

The standard model of cosmology provides multiple time measurements that are useful for different applications. Cosmic time t is often impractical to use in physical cosmology. The Doppler shift arising from the recession of distant objects is the **cosmic redshift** z ,¹ defined through

$$1 + z = a(t_0)/a(t), \quad (1.9)$$

where $t_0 \approx 13.8$ gigayears means today, and a is the dimensionless **cosmic scale factor**. The cosmic-time term is defined via $a(t \equiv 0) = 0$, which is to say that we define the time of Big Bang as the time blah blah [...] 「Fix!」

In this project we make use of **conformal time** τ for which $dt = a d\tau$ holds.

1.2.5 Cosmological simulations

PHANTOM PARAGRAPH: NYQUIST FREQUENCY, FUNDAMENTAL FREQUENCY, DFTs

High-performance computing

There are two main parallelisation techniques blah blah [...]

¹We will use z to distinguish the cosmic redshift from the Cartesian spatial coordinate z in $\mathbf{x} = (x, y, z)$, as they will both be used frequently.

Part I

Background

Chapter 2

General Relativity

Alongside quantum mechanics, Einstein's theory of gravity—general relativity—is widely accepted as the most accurate description of our surroundings. GR can be formulated from a geometrical point of view, or it can be viewed as a classical field theory. In the former approach we meet geometrical tools such as the geodesic equation, whereas the latter allows the application of field-theoretical methods. Considering both perspectives can be insightful and provide a better overall understanding of concepts in GR.

This chapter will cover the parts of GR that are most relevant for this project. In Section 2.1 we will introduce relevant terminology from differential geometry and elaborate on some techniques for handling hypersurfaces and conformal spaces. We move on to discuss in broad terms the Einstein's equation in Section 2.2. A brief introduction to modern cosmology is found in Section 2.3, before we address gravitational waves in Section 2.4. Hopefully, this will be sufficient to obtain a basic understanding of standard GR.

2.1 Differential geometry

Einstein formulated GR in terms of spacetime geometries, using the mathematical discipline known as differential geometry. Whilst most prominent in physics, differential geometry knows many applications in natural sciences. This section briefly introduces basic concepts and terminology of this mathematical branch. For formal definitions, see e.g. Carroll [8].

Manifolds are topological spaces that locally *look like* Euclidean space. They are characterised by metric tensors that describe their geometries. For example, the Minkowski spacetime from special relativity is described by the metric tensor (defined shortly) $\eta_{\mu\nu}$ which is related to the line element through

$$ds^2|_M = \eta_{\mu\nu} dx^\mu dx^\nu = -dt^2 + \delta_{ij} dx^i dx^j, \quad (2.1)$$

where δ_{ij} is the Kronecker delta (Eq. (4)). In the standard picture, the coordinates are $x^\mu = (t, x, y, z)$ such that the last term above is the three-dimensional Euclidean line element in Cartesian coordinates. Minkowski manifolds are special cases of pseudo-Riemannian manifolds (discussed below).

Metric tensor

The **metric tensor** $g_{\mu\nu}$ is a symmetric rank (0, 2) tensor that is non-degenerate ($\det(g) \neq 0$) and relates to the line element as

$$ds^2 = g_{\mu\nu} dx^\mu dx^\nu. \quad (2.2)$$

Its inverse satisfies $g^{\mu\kappa}g_{\kappa\nu} = \delta^\mu_\nu$, and we usually denote the determinant by $g = \det(g)$. The metric tensor is used to raise and lower indices of other tensors, e.g. $A_\mu = g_{\mu\nu}A^\nu$.

Pseudo-Riemannian manifolds

A manifold \mathcal{M} with a metric $g_{\mu\nu}$ that put into its *canonical form* is $\text{diag}(-1, +1, +1, \dots, +1)$ is called Lorentzian or **pseudo-Riemannian**. For all practical purposes, it is to say that the spacetime has one time dimension and arbitrary number (d) of spatial dimensions. We say that \mathcal{M} has $d + 1$ dimensions with coordinates x^μ , and emphasise that Greek indices runs from $\mu = 0, i$ and Latin ones $i = 1, \dots, d$. Now, there exists a unique connection $\Gamma_{\mu\nu}^\rho$ constructed from the metric, called the **Christoffel symbols** (see Eq. (5)). From this we get important structures such as the **covariant derivative** ∇_μ and the **Riemann curvature tensor** $\mathcal{R}^\rho_{\sigma\mu\nu}$ (see Eq. (6)). Further, one can construct the **Ricci tensor** $\mathcal{R}_{\mu\nu} = \mathcal{R}^\lambda_{\mu\lambda\nu}$, the contraction of which is the **Ricci scalar** $\mathcal{R} = g^{\mu\nu}\mathcal{R}_{\mu\nu}$. The **Bianchi identities**,

$$\mathcal{R}_{\mu\nu\alpha\beta;\gamma} + \mathcal{R}_{\mu\nu\gamma\alpha;\beta} + \mathcal{R}_{\mu\nu\beta\gamma;\alpha} = 0, \quad (2.3)$$

in GR reduce to $\mathcal{G}_{\mu\nu}{}^{;\nu} = 0$, where

$$\mathcal{G}_{\mu\nu} = \mathcal{R}_{\mu\nu} - \frac{1}{2}g_{\mu\nu}\mathcal{R} \quad (2.4)$$

is the **Einstein tensor**. IF TIME! WRITE BETTER.

2.1.1 Hypersurfaces

A manifold Σ *embedded* (contained within) in another manifold \mathcal{M} is a submanifold of the ambient spacetime. We define an **induced metric**

$$\gamma_{ab} = X^\mu_{,a}X^\nu_{,b}g_{\mu\nu} \quad (2.5)$$

where $X^\mu(\xi^a)$ is the embedding function describing the mapping $\Sigma \rightarrow \mathcal{M}$, and ξ^a are the coordinates on Σ .

A **hypersurface** of a $(p + q)$ -dimensional manifold \mathcal{M} is a submanifold of codimension 1, i.e. with $p + q - 1$ dimensions. We write the metric in **Gaussian normal coordinates** $\{Y, \xi^a\}$ as

$$ds^2 = \varsigma dY^2 + \gamma_{ab}d\xi^a d\xi^b, \quad (2.6)$$

where γ_{ab} is the induced metric in Eq. (2.5) [8]. We have

$$\varsigma = n_\mu n^\mu = \begin{cases} -1 & \text{if } \Sigma \text{ is spacelike,} \\ +1 & \text{if } \Sigma \text{ is timelike,} \end{cases} \quad (2.7)$$

where $n^\mu = (\partial_Y)^\mu$ is the normal vector. This means that spacelike hypersurfaces have timelike normal vectors, and vice versa.

We will define the **extrinsic curvature** as a tensor \widehat{K}_{ab} on Σ by

$$\widehat{K}_{ab} \equiv -X^\mu_{,a}X^\nu_{,b}\nabla_\nu n_\mu. \quad (2.8)$$

Note that this definition tends to vary in references [8].

2.1.2 Conformal geometry

The class of transformation called **conformal transformations** are in all essence local changes of scale. They are written

$$\tilde{g}_{\mu\nu} = \Upsilon^2(x)g_{\mu\nu}, \quad \exists \Upsilon(x) > 0, \quad (2.9)$$

where x denotes spacetime events on \mathcal{M} , and Υ is called the **conformal factor**. The convenience of conformal equivalence comes from the simple fact that any function of $g_{\mu\nu}$ can be thought of as a function of $\tilde{g}_{\mu\nu}$ and $\Upsilon(x)$.

The inverse transformation is trivial, $g_{\mu\nu} = \Upsilon^{-2}(x)\tilde{g}_{\mu\nu}$, and the determinant transforms as $\sqrt{-\tilde{g}} = \Upsilon^d \sqrt{-g}$, where d is the dimension of the spacetime. The conformally-transformed Christoffel symbols take the form

$$\tilde{\Gamma}_{\mu\nu}^\rho = \Gamma_{\mu\nu}^\rho + C_{\mu\nu}^\rho, \quad (2.10)$$

where

$$C_{\mu\nu}^\rho = \Upsilon^{-1} \left(2\delta_{(\mu}^\rho \Upsilon_{,\nu)} - g_{\mu\nu} g^{\rho\sigma} \Upsilon_{,\sigma} \right). \quad (2.11)$$

We obtain neat expressions for the Riemann and Ricci tensors and the Ricci scalar, which we will not list here.¹

Consider a scalar field ϕ . We get $\phi_{;\mu} = \phi_{,\mu} = \phi_{,\mu}$ for the covariant derivative, and as for the d'Alembertian,

$$\tilde{\square}\phi = \Upsilon^{-2} \square\phi + (d-2)g^{\rho\sigma}\Upsilon^{-3}\Upsilon_{,\rho}\phi_{,\sigma}. \quad (2.12)$$

We consider two special cases of such relations that will be of use in this thesis.

Expanding universe

If $\Upsilon(x) = a(\tau)$ and $ds^2 = -d\tau^2 + d\Sigma^2$, where Σ is a space-like hypersurface with a given Gaussian curvature, then $\tilde{ds}^2 = a^2 ds^2$ is the FLRW line element (see Section 2.3). If $\Sigma = \mathbb{R}^3$, the metric $\tilde{g}_{\mu\nu}$ is said to be conformally flat. We define the Fourier transform of a function $f(\mathbf{x})$ of comoving coordinates \mathbf{x} as

$$\tilde{f}(\mathbf{k}) = \int d^3x f(\mathbf{x}) e^{i\mathbf{k}\cdot\mathbf{x}}, \quad (2.13a)$$

and its inverse

$$f(\mathbf{x}) = \int \frac{d^3k}{(2\pi)^3} \tilde{f}(\mathbf{k}) e^{-i\mathbf{k}\cdot\mathbf{x}}, \quad (2.13b)$$

where \mathbf{k} is the comoving wavevector. The comoving frame relates these coordinates to physical coordinates by $\mathbf{x}_{\text{ph}} = a\mathbf{x}$ and $\mathbf{k}_{\text{ph}} = \mathbf{k}/a$.

The d'Alembertian is

$$\tilde{\square}\phi = a^{-2}(\square_M\phi - 2\mathcal{H}\partial_\tau\phi), \quad (2.14)$$

where $\mathcal{H} = a^{-1}\partial_\tau a$ and $\square_M \equiv \partial^\mu\partial_\mu$.

Note that more often than not, the tilde will be reserved for other quantities, and the metric $g_{\mu\nu}$ will refer to the generalised metric or FLRW if specified.

Scalar–tensor theories

A scalar–tensor theory (see Section 3.2) with auxiliary field $\phi(x)$ can be formulated (mathematically) equivalently in two different reference frames related by $\tilde{g}_{\mu\nu} = A^2(\phi)g_{\mu\nu}$. Here, $g_{\mu\nu}$ defines what is known as the **Einstein frame**, and $\tilde{g}_{\mu\nu}$ the **Jordan frame**.

¹COMMENT?

2.2 Einstein's equation

How does the gravitational field affect how matter behaves, and in what way is matter controlling the gravitational field? Newtonian gravity proposes very good answers to these questions: The acceleration of an object in a gravitational potential Φ is

$$\mathbf{a} = -\nabla\Phi, \quad (2.15)$$

and said field is governed by the matter density ρ through the Poisson equation

$$\nabla^2\Phi = 4\pi G_N \rho. \quad (2.16)$$

[In physics, the answer to a question is highly dependent on *how the question was asked*. A common misconception is that Newtonian gravity was disproven by Einstein. Newton was simply telling a different story; a story about dynamics in non-relativistic systems.² Einstein confronted gravitational physics with different but analogous questions, and subsequently more complex answers than Newton. General relativity explains how curvature of spacetime influences matter, manifesting as gravity, and in what way energy and momentum affects spacetime to create curvature.] In mathematical terms, these are the **geodesic equation**

$$\frac{d^2 x^\mu}{d\lambda^2} = -\Gamma_{\rho\sigma}^\mu \frac{dx^\rho}{d\lambda} \frac{dx^\sigma}{d\lambda} \quad (2.17)$$

and **Einstein's equation**

$$\mathcal{G}_{\mu\nu} = 8\pi G_N T_{\mu\nu}. \quad (2.18)$$

One can arrive at this equation by use of the minimal coupling principle and Bianchi identities (Eq. (2.3)), as explained in Carroll [8, Ch. 4]. A more tangible way to obtain the same equation is to vary the combined matter and Einstein–Hilbert actions $S = S_{\text{EH}} + S_{\text{m}}$, where

$$S_{\text{EH}} = \frac{M_{\text{Pl}}^2}{2} \int d^4x \sqrt{-g} \mathcal{R}. \quad (2.19)$$

The result is

$$\mathcal{R}_{\mu\nu} - \frac{1}{2} g_{\mu\nu} \mathcal{R} = -\frac{1}{M_{\text{Pl}}^2} \frac{2}{\sqrt{-g}} \frac{\delta S_{\text{m}}}{\delta g^{\mu\nu}}, \quad (2.20)$$

where the right-hand side is identified as proportional the energy–momentum tensor, $8\pi G_N T_{\mu\nu}$, and the left-hand side is the Einstein tensor $\mathcal{G}_{\mu\nu}$ (Eq. (2.4)). We see that Eqs. (2.18) and (2.20) are equivalent. **[(d + 1) dimensions?]**

2.2.1 Energy–momentum tensor

The (Hilbert) **stress–energy (SE) tensor**, also known as the energy–momentum tensor, constitute the non-geometrical part of the Einstein equation—the right-hand side of Eq. (2.18). It encodes information about the energy and momentum contained in the system.

For a perfect fluid, the SE tensor in the fluid rest frame is $T^\mu_\nu = \text{diag}(-\rho, p, p, p)$ where ρ is the homogeneous energy density and p the isotropic pressure. We will address this in a cosmological context in the next section.

²Which, to be fair, are most common on Earth.

Conformal transformations

Let us comment on the energy–momentum tensor under conformal transformations Eq. (2.9). Consider the matter action in d spacetime dimensions

$$\widetilde{S}_m = \int d^d x \sqrt{-\widetilde{g}} \widetilde{\mathcal{L}}_m = \int d^d x \sqrt{-g} \mathcal{L}_m = S_m, \quad (2.21)$$

where the Lagrangian $\widetilde{\mathcal{L}}_m = \Upsilon^{-d} \mathcal{L}_m$ [14]. [We let ${}^{(m)}T \triangleq T$ and ${}^{(m)}\widetilde{T} \triangleq \widetilde{T}$ denote the matter energy and momentum in the two frames for notational ease.] Under Eq. (2.9), the *matter* SE tensor transforms as

$$\widetilde{T}^\mu{}_\nu = \Upsilon^{-d} T^\mu{}_\nu, \quad (2.22)$$

and thus the trace $T \equiv g^{\mu\nu} T_{\mu\nu}$ transforms as $\widetilde{T} = \Upsilon^{-d} T$.

As a result, we get different conservation laws in the two frames:

$$T^{\mu\nu}{}_{;\nu} = 0 \quad \Rightarrow \quad \widetilde{T}^{\mu\nu}{}_{;\nu} = -\Upsilon^{-1} \Upsilon^{,\mu} \widetilde{T}, \quad (2.23)$$

or vice versa:

$$\widetilde{T}^{\mu\nu}{}_{;\nu} = 0 \quad \Rightarrow \quad T^{\mu\nu}{}_{;\nu} = \Upsilon^{-1} \Upsilon^{,\mu} T. \quad (2.24)$$

2.2.2 Linearised gravity

Applying perturbation theory to the metric gives rise to a new set of equations, often referred to as the “linearised Einstein field equations.” The general starting point is to expand the metric to the order o in question,

$$\mathring{g}_{\mu\nu} = g_{\mu\nu} + \sum_{i=1}^o (\delta^i g)_{\mu\nu}. \quad (2.25)$$

Consequently, the perturbed Einstein reads

$$\mathring{\mathcal{G}}_{\mu\nu} = 8\pi G_N \mathring{T}_{\mu\nu}, \quad (2.26)$$

where $\mathring{\mathcal{G}}_{\mu\nu}$ and $\mathring{T}_{\mu\nu}$ are the o th order perturbed Einstein and SE tensor, respectively. Equation (2.26) is then solved order by order.

For first-order perturbations to the metric, we get [23]

$${}^{(0)}\mathcal{G}^\mu{}_\nu = 8\pi G_N {}^{(0)}T^\mu{}_\nu, \quad (2.27a)$$

$${}^{(1)}\mathcal{G}^\mu{}_\nu = 8\pi G_N {}^{(1)}T^\mu{}_\nu, \quad (2.27b)$$

where superscript ${}^{(i)}$ refers to perturbative order i . Equation (2.27a) is the background equation. With $\nabla^\mu q_{\mu\nu} = 0$, Eq. (2.27b) now reads [23]

$$\square q_{\mu\nu} - 2\mathcal{R}_{\rho\mu\nu\sigma} q^{\rho\sigma} - 2\mathcal{R}^\rho{}_{(\mu} q_{\nu)\rho} - g_{\mu\nu} q^{\rho\sigma} \mathcal{R}_{\rho\sigma} + q_{\mu\nu} \mathcal{R} = -16\pi G_N {}^{(1)}T_{\mu\nu} \quad (2.28)$$

where

$$q_{\mu\nu} \triangleq (\delta^1 g)_{\mu\nu} - \frac{1}{2} g_{\mu\nu} (\delta^1 g)^\rho{}_\rho \quad (2.29)$$

and

$${}^{(1)}T_{\mu\nu} = {}^{(1)}(g_{\mu\rho} T^{\rho\nu}) = (\delta^1 g)_{\mu\rho} T^\rho{}_\nu + g_{\mu\rho} (\delta^1 T)^\rho{}_\nu. \quad (2.30)$$

Possibly unnecessary...

2.3 Modern cosmology

Employing the cosmological principle (CP) to the Einstein equation, simplifies them drastically. The cosmological principle states that the universe is spatially homogeneous and isotropic, or equivalently that the line element of the universe takes the form $ds^2 = -dt^2 + a^2(t)d\Sigma^2$ where $d\Sigma^2$ is a three-dimensional metric with a specified Gaussian curvature. The scale factor a describing the universe's expansion is

$$a = \frac{1}{1 + \mathfrak{z}}, \quad (2.31)$$

where \mathfrak{z} is the cosmic redshift. This was the starting point for Alexander Friedmann (1888–1925) when he developed the Friedmann equations. If CP holds—which is widely accepted as a good approximation at large scales, typically orders larger than $\mathcal{O}(100 \text{ Mpc})$ —any constituent s behaves as a perfect fluid, and the Hubble parameter H reads

$$H^2 = H_0^2 \sum_s \Omega_{s0} a^{-3(1+w_s)}, \quad (2.32)$$

where $\Omega_{s0} \equiv \rho_{s0}/\rho_{\text{cr}0}$ is a dimensionless present-day energy density parameter, normalised to the critical density today, $\rho_{\text{cr}0} = 3H_0^2 M_{\text{pl}}^2$. w_s is the equation-of-state parameter of s , i.e.

isotropic pressure = $w \cdot$ homogeneous density.

- Relativistic matter (radiation, neutrinos): $w_{\text{r}} = 1/3$
- Non-relativistic matter (baryons, CDM): $w_{\text{m}} = 0$
- Effective curvature: $w_{\text{K}} = -1/3$
- Domain wall network: $w_{\text{dw}} = -2/3$
- Vacuum energy (Λ): $w_{\Lambda} = -1$

Note that we define Big Bang as the time when $a = 0$ and today as the time when $a = a_0 = 1$.

We will work with conformal time τ that relates to cosmic time t such that the metric is

$$ds^2 = a^2(-d\tau^2 + d\Sigma^2). \quad (2.33)$$

Subsequently, we make use of the conformal Hubble factor $\mathcal{H} \equiv aH$, given by

$$\mathcal{H}^2 = H_0^2 \sum_s \Omega_{s0} a^{-(1+3w_s)}, \quad (2.34)$$

To get simplified—or simply analytically solvable—equations, we often assume $a \sim \tau^\alpha$ that corresponds to a universe dominated by a single substance. α is ultimately determined by the equation-of-state parameter w_s associated with the substance s in question,

$$\alpha = \frac{2}{1 + 3w_s}. \quad (2.35)$$

This means that $\alpha = 1$ and $\alpha = 2$ for radiation (RD) and matter domination (MD), respectively.

With fiducial observed values for $\Omega_{\text{r}0}$, $\Omega_{\text{m}0}$ and $\Omega_{\Lambda 0}$, it is understood that our universe was dominated by radiation in its early stages, after inflation and until before $a = \Omega_{\text{r}0}/\Omega_{\text{m}0}$ (when $\rho_{\text{m}} = \rho_{\text{r}}$, about 50 thousand years after Big Bang). The universe entered a matter-dominated era after this, until $a = (\Omega_{\text{m}0}/\Omega_{\Lambda 0})^{1/3}$ (when $\rho_{\Lambda} = \rho_{\text{m}}$, about 10 billion years after Big Bang). The universe started accelerating, and is currently on steady course to a vacuum dominated era.

Hubble trouble

The **Hubble tension** refers to a discrepancy between measurements of the Hubble constant describing the expansion rate of the universe. Different methods yield conflicting values of $H_0 = 100h_0 \text{ km s}^{-1} \text{ Mpc}^{-1}$. Local measurements involving for example distant supernovae suggest $h_0 \approx 0.73$ [e.g. 29]. In contrast, the other approach, derived from CMB observations by the Planck satellite, indicates $h_0 \approx 0.67$ [e.g. 29]. Their confidence intervals do not overlap, thus necessitating new measurements [e.g. 29]. [This citing seems excessive...](#)

Many argue that revision of Λ CDM is necessary. The accelerated expansion is a late-universe phenomenon conservatively made clear by the dark-energy/cosmological-constant duality, with $w_{\text{de}} = w_\Lambda = -1$. Introducing instead a time-dependent “phantom” equation-of-state parameter $w_{\text{de}}(a)$ can harmonise the two measurements [29]. ★

[More details?](#)

2.3.1 Cosmological perturbation theory

Just look around you—the universe is definitely *not* homogeneous and isotropic. The story of structure formation as we know it is told through cosmological perturbation theory. The leading-order perturbed metric $\hat{g}_{\mu\nu} = g_{\mu\nu} + \delta g_{\mu\nu}$ can be written in terms of functions A , B_i and C_{ij} ,

$$ds^2 = a^2 \left[-(1 + 2A)d\tau^2 + 2B_i dx^i d\tau + (\delta_{ij} + C_{ij})dx^i dx^j \right]. \quad (2.36)$$

It is convenient to adopt the convention that spatial vectors and tensors are raised and lowered with δ , e.g. $C^{ij} = \delta^{ik}\delta^{jl}C_{kl}$. The symmetric metric has ten degrees of freedom, and a scalar-vector-tensor (SVT) decomposition separates these into four scalar, four vector and two tensor degrees of freedom:

$$A \rightarrow A, \quad (2.37a)$$

$$B_i \rightarrow \partial_i B + F_i, \quad (2.37b)$$

$$C_{ij} \rightarrow (2\delta_{ij}C + 2\partial_i \partial_j D - (2/3)\delta_{ij}\nabla^2 D) + 2\partial_{(i} G_{j)} + 2E_{ij}. \quad (2.37c)$$

This is extremely useful since in the first-order linearised Einstein equation for scalars, vectors and tensors do not mix. We treat these separately and assume they originate from inflation.

- Scalar perturbations (A , B , C , D) are density perturbations and describe structure formation.
- Vector perturbations (F_i , G_i) are not predicted by inflation, and would in any case only have decaying solutions, and are thus cosmologically irrelevant.
- Tensor perturbations (E_{ij})—gravitational waves—are predicted by inflation.

This thesis focuses solely on the tensorial part of the metric perturbation. Therefore, we will consider the divergence- and traceless $h_{ij} = 2E_{ij}$. This particular choice is called the **transverse-traceless (TT) gauge**, and will be addressed in the next section. Plugging this into the linearised Einstein equation Eq. (2.26), we get the equation of motion for the tensor perturbations h_{ij} , which (spoiler alert) are in fact the gravitational waves.

2.4 Gravitational waves

Gauge freedom, in a general context, refers to the invariance of a physical theory under certain transformations that do not alter the observable quantities or physical content of the theory. In

GR, gauge freedom manifests as invariance under coordinate transformations, which is used to simplify the metric or solve Einstein's equation more easily. By choosing an appropriate gauge we can eliminate redundancies.

Metric perturbations on a homogeneous and isotropic background leaves two tensor degrees of freedom. We isolate the physical, observable components of metric tensor perturbation by selecting the TT gauge.

If the symmetric 4×4 -tensor $h_{\mu\nu}$ fulfils the TT conditions

$$h_{0\mu} = 0, \quad h^i_i = 0, \quad h_{ij}{}^{,i} = 0, \quad (2.38)$$

there are necessarily only two degrees of freedom to this quantity. We can therefore choose a polarisation basis to represent the gravitational waves. In the **linear polarisation basis** we consider plus- (+) and cross- (×) polarised states. 「Comment about spin 2.」 The tensor representation is written as a superposition of these states,

$$h_{ij} = h_+ e_{ij}^+ + h_\times e_{ij}^\times, \quad (2.39)$$

with polarisation tensors

$$\begin{aligned} e^+(\mathbf{k}) &= \hat{\mathbf{m}} \otimes \hat{\mathbf{m}} - \hat{\mathbf{n}} \otimes \hat{\mathbf{n}} \quad \text{and} \\ e^\times(\mathbf{k}) &= \hat{\mathbf{m}} \otimes \hat{\mathbf{n}} - \hat{\mathbf{n}} \otimes \hat{\mathbf{m}}. \end{aligned} \quad (2.40)$$

[Here, $\mathbf{k} = k\hat{\mathbf{\Omega}}$ is the momentum vector, $\hat{\mathbf{\Omega}}$ is propagation direction of the gravitational waves, $\{\hat{\mathbf{m}}, \hat{\mathbf{n}}, \hat{\mathbf{\Omega}}\}$ is a right-handed orthonormal basis, and

$$e_{ij}^P e_{P'}^{ij} = 2\delta_{P'}^P. \quad (2.41)$$

┐ Note that

$$|h^2| = h^{ij} h_{ij} = 2 \sum_P h_P^2. \quad (2.42)$$

We extract the TT-part of a symmetric 3×3 tensor by use of the projection tensor in Eq. (7). The spin-2 projector is non-local in space, and we define the TT-projected tensor in coordinate space as

$$h_{ij}(\tau, \mathbf{x}) = \int \frac{d^3k}{(2\pi)^3} e^{-i\mathbf{k}\cdot\mathbf{x}} \Lambda_{ij}^{kl}(\mathbf{k}) \tilde{h}_{kl}(\tau, \mathbf{k}) = \sum_{P=\pm, \times} \int \frac{d^3k}{(2\pi)^3} e^{-i\mathbf{k}\cdot\mathbf{x}} \tilde{h}_P(\tau, \mathbf{k}) e_{ij}^P(\mathbf{k}). \quad (2.43)$$

Note that the TT conditions in Eq. (2.38) becomes

$$\tilde{h}_{0\mu} = 0, \quad \tilde{h}^i_i = 0, \quad k^i \tilde{h}_{ij} = 0, \quad (2.44)$$

in Fourier space.

2.4.1 Expanding universe

We are interested in a flat FRLW background plus first order in perturbations, and define the perturbed metric as $\hat{g}_{\mu\nu} = a^2(\eta_{\mu\nu} + h_{\mu\nu})$. Furthermore, we focus on the tensorial part of the perturbations, leaving

$$ds^2 = a^2(\tau) \left(-d\tau^2 + [\delta_{ij} + h_{ij}(\tau, \mathbf{x})] dx^i dx^j \right) \quad (2.45)$$

for the perturbed line element.

We define an anisotropic stress–energy tensor $\Pi_{ij} \equiv T_{ij} - \delta_{ij}\delta^{kl}T_{kl}$, and project it onto the TT gauge. It is useful to define a stress–energy tensor whose indices are raised and lowered with δ_{ij} . We impose the TT-conditions in Eq. (2.38) on this such that

$$\pi_{ij} = \pi^{ij} = \pi^i_j \equiv \Pi^i_j|_{\text{TT}} = a^{-2}\Pi_{ij}^{\text{TT}} = a^{-2}\Lambda_{ij}^{kl}\Pi_{kl}. \quad (2.46)$$

Note that $\Pi_{ij}^{\text{TT}} = T_{ij}^{\text{TT}}$. We consider the linearised Einstein equation (Eq. (2.26)) in this gauge. Now, to first order we have $\delta\mathcal{G}^i_j = 8\pi G_N\delta T^i_j$ as the only non-vanishing components, giving [29]

$$-\frac{1}{2}\square h_{ij} = 8\pi G_N\pi_{ij}. \quad (2.47)$$

The equation of motion for h_{ij} is

$$\ddot{h}_{ij} + 2\mathcal{H}\dot{h}_{ij} - \nabla^2 h_{ij} = 16\pi G_N a^2 \pi_{ij} \quad (2.48)$$

where a dot signifies the conformal time derivative, $\dot{} \equiv d/d\tau$.

It is convenient to introduce a scaled strain $\psi \equiv ah$ and transform to Fourier space. The equation now reads

$$\ddot{\psi}_P + \left(k^2 - \frac{\ddot{a}}{a}\right)\tilde{\psi}_P = k^2 f_P; \quad P = +, \times, \quad (2.49)$$

where

$$f_P \equiv \frac{16\pi G_N a^3 \tilde{\pi}_P(\tau, \mathbf{k})}{k^2}. \quad (2.50)$$

Homogeneous solution. We see that for large modes $k \gg \ddot{a}/a \sim \tau^{-2}$, the linear operator is approximately $\partial_\tau^2 + k^2$, i.e. the harmonic oscillator, with plane wave solutions for $f_P = 0$. That is to say, small-scale gravitational waves, in the absence of a source, propagate free waves in an FRW spacetime (divided by the scale factor). On larger scales, the propagation is damped in accordance with the expansion of the universe. This damping term generally depends on expansion history.

Inhomogeneous solution. The method of Green's functions presents a suitable recipe for determining the dynamics of tensor perturbations on an expanding background. There are some limitations, however, as to the analytical solvability of the system. In the small-scale limit, the damping is neglected, and we only need the retarded Green's function associated with the harmonic oscillator, $\sin(k(\tau - \tau'))/k$. Otherwise, an equation of the form $L_{u=k\tau}\tilde{\psi}_P = f_P$, where

$$L_u = \frac{d^2}{du^2} + \left(1 - \frac{(\alpha - 1)\alpha}{u^2}\right) \quad (2.51)$$

has a Green's function in terms of Bessel functions $\sqrt{u}Z_{\alpha-1/2}(u)$, which is the case in a single-substance universe with $a \propto \tau^\alpha$. On an even more compact form, if $n \equiv \alpha - 1 \in \mathbb{Z}$, we can use the Green's function

$$G(u, v) = S_n(u)C_n(v) - C_n(u)S_n(v) \quad (2.52)$$

where $S_n(x)$ and $C_n(x)$ are the Riccati–Bessel and –Neumann functions (given in Appendix A).

Assume homogeneous initial conditions $\tilde{\psi}_P(\tau_i, \mathbf{k}) = \dot{\tilde{\psi}}_P(\tau_i, \mathbf{k}) = 0$. The full solution is as follows:

$$a(\tau)\tilde{h}_{ij}(\tau, \mathbf{k}) = \frac{16\pi G_N}{k^2} \int_{\tau_i}^{\tau} d\hat{\tau} G(k\tau, k\hat{\tau}) a^3(\hat{\tau}) \tilde{\pi}_{ij}(\hat{\tau}, \mathbf{k}). \quad (2.53)$$

If the source disappears after $\tau_f - \tau_i$, we may write the solution as

$$\tilde{\psi}_{ij}(\tau, \mathbf{k}) = S_n(k\tau)F_2(\mathbf{k}) - C_n(k\tau)F_1(\mathbf{k}) \quad (2.54)$$

with

$$F_i(\mathbf{k}) = \int_{\tau_i}^{\tau_f} d\hat{\tau} R_n^{(i)}(k\hat{\tau})f_P(\hat{\tau}, \mathbf{k}), \quad (2.55)$$

where $R^{(i)}$ refers to the Riccati–Bessel function of i th kind.

Chapter 3

Symmetry-Breaking Dark Energy

When a system spontaneously changes from one physical state to another due to external conditions such as temperature or pressure reach certain critical points, it is said to undergo a **phase transition**. Water for example changes from liquid to gas at the critical temperature 100°C , given atmospheric pressure. Spontaneous symmetry breaking (SSB), an important concept in especially particle physics and cosmology, occurs when the physical laws possess a certain symmetry, but the vacuum state does not [25].

Topological defects, or topological solitons, are ubiquitous and manifest in a variety of forms across different scales and systems. Their hypothesised existence in exotic environments such as the early universe is further motivated by proofs of their existence in everyday life, such as whorls, loops and arches in our fingerprints [17]. It was in fact a very mundane event in 1834 that induced the first formal description of a **soliton**; John Russell Scott (1808–1882) keenly observed a hump of water moving from the prow of a boat rapidly down a canal whilst preserving its shape [35]. Such solitary waves that can interact with others and restore its shape were later named “solitons”.

3.1 Cosmological defects

Solitons are remarkably stable “humps” of energy. The simplest soliton is the topological soliton best known as the **kink**. Kink solutions placed in spacetime with more than one spatial dimension, they become extended, planar structures (or membranes), that which we call “domain walls” [35]. Domain walls possess richer dynamics than kinks, and these are quite well understood in Minkowski spacetimes. In contrast to higher codimension defects like strings and monopoles, kinks and domain walls are of codimension one and therefore also hypersurfaces, at least approximately. **W- TIME!** COMMENT ABOUT APPLICABILITY... The study of kinks and domain walls can to some extent be applied to other topological defects.

Domain walls are of particular interest in this project, specifically the \mathbb{Z}_2 type. These two-dimensional topological defects that occurs where a discrete symmetry is broken.¹ To give an idea of the basic properties of topological defects, we present an example. More thorough derivations can be found in Vachaspati [35].

¹Likewise, cosmic strings and monopoles are products of axial/cylindrical and spherical symmetry breaking, respectively.

3.1.1 Example: (stationary) \mathbb{Z}_2 kinks

The king of kinks, the so-called “ \mathbb{Z}_2 kink,” can be described through a scalar field ϕ with the action $S = S_{\text{EH}} + S_{\mathbb{Z}_2}$,

$$S_{\mathbb{Z}_2} = \int d^{n+1}x \sqrt{-g} \left\{ -\frac{1}{2} g^{\mu\nu} \partial_\mu \phi \partial_\nu \phi - V(\phi) \right\}, \quad (3.1)$$

where $V(\phi)$ is the two-fold degenerate potential $V(\phi) = \lambda(\phi^2 - \eta^2)^2$. The equation of motion $\square\phi = V_{,\phi}$ can be derived from variation of S with respect to ϕ . For simplicity, we consider Minkowski spacetime with 1 + 1 dimensions where $\eta_{\mu\nu} = \text{diag} = (-1, 1)$ is the metric. The equation of motion reads

$$-\partial_t^2 \phi + \partial_x^2 \phi = \lambda(\phi^2 - \eta^2)\phi. \quad (3.2)$$

Setting time derivatives to zero, and imposing boundary conditions $\phi(x \rightarrow \pm\infty) = \pm\eta$, we obtain a class of static solutions

$$\phi_k(x - x_0) = \eta \tanh\left(\sqrt{\frac{\lambda}{2}} \eta(x - x_0)\right), \quad (3.3)$$

where x_0 is the position of the kink. IF TIME! WRITE ABOUT TRANSLATIONAL INVARIANCE.

Multi-kink field. Without commenting further, we state that this kink has *topological charge* $Q = 1$ (Vachaspati [see 35, Ch. 1] for discussion). This comes from the boundary conditions, and thus similar arguments constructs solutions with $Q = -1$ by swapping the boundaries; $\phi(x \rightarrow \pm\infty) = \mp\eta$. This is the *antikink* solution $\bar{\phi}_k(x) = -\phi_k(x)$. A feature of the \mathbb{Z}_2 kinks is that one cannot have a system with topological charge $|Q| > 1$. For sufficiently separated kinks and antikinks located at x_i and \bar{x}_j , respectively, we write [35]:

$$\phi(x) = \frac{\eta}{\eta^{N+M}} \prod_i^N \phi_k(x - x_i) \prod_j^M \bar{\phi}_k(x - \bar{x}_j), \quad (3.4)$$

where $|N - M| \leq 1$ and $x_i < \bar{x}_j < x_{i+1}$. This describes the allowed system of N kinks and M antikinks aligned in an alternating structure.

Basic properties

The energy of the kink is obtained integrating over the energy density, i.e.

$$E = - \int dx T^0_0 = \frac{2\sqrt{2}}{3} \lambda \eta^3. \quad (3.5)$$

We define the half-width of the kink to be

$$w = \frac{1}{\eta \sqrt{\lambda}}. \quad (3.6)$$

Most of the energy is confined within $x \in x_0 \pm w$. See Fig. 3.1 for illustrative explanation accompanied by a demonstration of how a Gaussian with standard deviation $w/\sqrt{2}$ tracks the kink's energy profile.

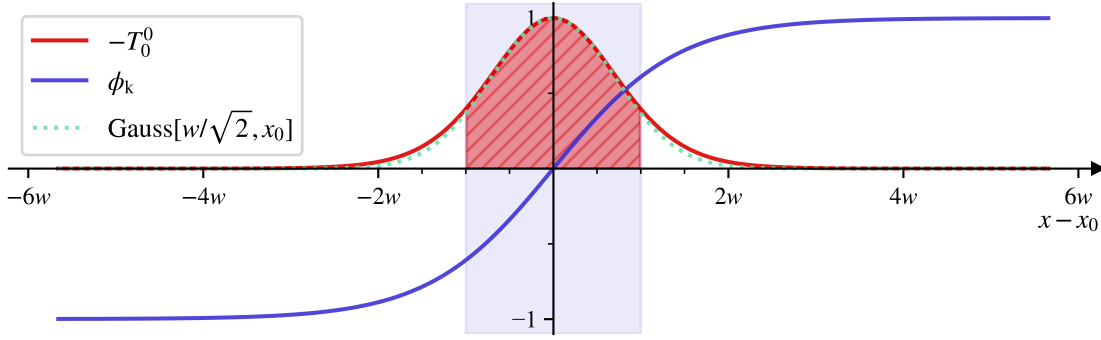


Figure 3.1: Demonstration of the \mathbb{Z}_2 kink and its energy content for $\eta = 1$ and $\lambda = 2$. The green dotted graph is a Gaussian around $x = x_0$ with standard deviation $w/\sqrt{2}$. Inspiration from Vachaspati [35].

3.1.2 Domain walls

The kink solution in Section 3.1.1 put in two more spatial dimensions (setting $\eta_{\mu\nu} = \text{diag}(-1, 1, 1, 1)$) is a planar \mathbb{Z}_2 domain wall. The volume integral in Eq. (3.5) is instead an integral over one axis, which means the result is a surface energy density. This is better known as the **surface tension** of the wall, denoted σ , and reads $\sigma = -\int dz T_0^0$ for a wall in the xy -plane. In analogy with the width parameter, we will refer to δ as the **wall thickness** (parameter), and we see from Fig. 3.1 that a Gaussian with standard deviation δ tracks the energy density well.

For later convenience, we define σ_∞ and δ_∞ as the surface tension and wall thickness as their solutions in the stationary \mathbb{Z}_2 scenario, respectively. In terms of the mass scale $\mu = \eta\sqrt{\lambda}$,² this amounts to

$$\sigma_\infty \equiv \frac{2\sqrt{2}}{3} \frac{\mu^3}{\lambda} \quad \text{and} \quad \delta_\infty \equiv \frac{1}{\mu}. \quad (3.7)$$

Cosmological implications

We can model a network of domain walls a perfect fluid with equation-of-state parameter $w_{\text{dw}} = -2/3$.³ This implies that in the absence of a greater cosmological constant (if $\Omega_{\Lambda 0} < \Omega_{\text{dw}0}$), even a tiny energy contribution from this network would eventually dominate the energy density in the universe. As this overclosing of the universe happens before matter–dark-energy equality, this contradicts observations.

The prototypical defect is manifestly stable (robust against perturbations) and dissipationless (survive indefinitely). One way to surpass the overclosing problem is to introduce an **energy bias** between the two vacua, so that the system eventually converges to the true minima and the walls disappear [33]. Another method is to let σ decrease with time (melting domain walls), which is considered in Babichev et al. [5].

3.1.3 Defect formation

Cosmological defects typically form during a phase transition, and it is the nature of the associated (broken) symmetry that decides what type of defect we have at hand. We mention cosmic strings and monopoles arising from axial and spherical symmetry breaking, respectively. Domain walls—the main interest of this thesis—form when *discrete* symmetries are broken.

²In Part II, we set $\phi_\infty = \eta$.

³This is easily seen from the trace Nambu–Goto stress–energy tensor in Minkowski space.

To study phase transitions it is helpful to use the **effective potential** that takes into account the interaction between some field and a background. [An effective potential can ensure that a scalar field does not really show itself until some critical temperature. The global minimum at high temperatures turns local at low temperatures. The false vacuum state is metastable, and external perturbations can trigger the system's transition to the true vacuum. This is the prototypical formulation of a first-order phase transition [35].] We will demonstrate this in Section 3.2 in the asymmetron scenario.

Energy bias

Existence of discrete vacua implicates existence of domain walls. The degeneracy of these vacua ensures the stability of such walls. If we imagine a slight break in this degeneracy, that is, if one vacuum is favoured over another, biased domain walls form [35]. Some models employ an energy gap directly into the potential. A generalisation of the symmetron model—the *asymmetron*—include a cubic term that also changes the vacuum expectation value. We will discuss the latter in Section 3.2.2.

3.2 TITLE (Quintessence/Scalar field theories)

The general picture interprets quintessence as a group of scalar–tensor theories; a subgroup of modifications to gravity in which a scalar field is added to the total action. By going through all possible covariants with maximum second order time derivatives in four dimensional spacetime, one arrives at the most general formulation of these type of theories, the *Hordenski theory*. Said theory is summed up by the total Lagrangian density $\mathcal{L}_H = \mathcal{L}_m + M_{\text{pl}}^2 \sum_{i=2}^5 \mathcal{L}_i$, where \mathcal{L}_i are built up by derivatives of the scalar field, the Einstein tensor and arbitrary functionals of the scalar field ϕ and its kinetic term $X = -\frac{1}{2}\phi^{;\mu}\phi_{;\mu}$.⁴ Let $\mathcal{L}_i = 0$ as a starting point. General relativity—represented by the Einstein–Hilbert action—is retrieved with $\mathcal{L}_4 = \mathcal{R}/2$. By also setting $\mathcal{L}_2 = X(\phi) - V(\phi)$, we get a quintessence model. Performing relevant variations eventually gives an equation of motion that is indistinguishable from standard GR with $\mathcal{L}_m \rightarrow \mathcal{L}_m + \mathcal{L}_2$ in the stress–energy tensor on the right-hand side of the Einstein equation. Thus, quintessence models are not actually modified gravity theories, but adds to the total matter in the universe, and should be classified as a scalar field theory rather than a scalar–tensor theory.

3.2.1 General framework

We go through the dynamics of a bosonic quintessence field ϕ that is associated with a kinetic term $X = -\frac{1}{2}\phi^{;\mu}\phi_{;\mu}$ and potential energy $V(\phi)$ in [rough stages]. This will lay the foundation for our treatment of the (a)symmetron model in Section 3.2.2.

⁴With the usual notation convention and arbitrary functionals G_i , the Lagrangian densities \mathcal{L}_i are given by the following:

$$\begin{aligned}\mathcal{L}_2 &= G_2(\phi, X), \\ \mathcal{L}_3 &= G_3(\phi, X)\square\phi, \\ \mathcal{L}_4 &= G_4(\phi, X)\mathcal{R} + G_{4,X}(\phi, X)((\square\phi)^2 - \phi_{;\mu\nu}\phi^{;\mu\nu}), \\ \mathcal{L}_5 &= G_5\mathcal{G}_{\mu\nu}\phi^{;\mu\nu} - 1/6G_{5,X}(\phi, X)((\square\phi)^3 + 2\phi^{\nu}_{;\mu}\phi^{\mu}_{;\nu} - 3\phi_{;\mu\nu}\phi^{;\mu\nu}\square\phi),\end{aligned}$$

where $G_{i,X} = \partial G_i / \partial X$.

The dynamics of the quintessence field ϕ is described by the Einstein-frame action (see Section 2.1.2)

$$S = \int d^4x \sqrt{-g} \left\{ \frac{M_{\text{Pl}}^2}{2} \mathcal{R} + X(\phi) - V(\phi) \right\} + S_{\text{m}}[\tilde{g}_{\mu\nu}, \Psi], \quad (3.8)$$

where Ψ collects all matter fields, which couple minimally to the Jordan-frame metric,

$$\tilde{g}_{\mu\nu} = A^2(\phi) g_{\mu\nu} \quad (3.9)$$

and S_{m} is the total matter action. Without the presence of this last term, the equation of motion for the scalar field is $\square\phi = V_{,\phi}$. The minimal coupling to matter contributes s.t. $\square\phi \supset -A^3 A_{,\phi} \tilde{T}_{\text{m}}$, where $\tilde{T}_{\text{m}} = {}^{(\text{m})}\tilde{T}_{\mu\nu} \tilde{g}^{\mu\nu}$ is the trace of the Jordan-frame matter SE tensor [10, 21]. In particular,

$$\square\phi = V_{,\phi}(\phi) - A^3(\phi) A_{,\phi}(\phi) \tilde{T}_{\text{m}}. \quad (3.10)$$

We model the matter content as non-interacting, perfect fluids indexed s with equation-of-state parameter w_s such that the trace becomes $\tilde{T}_{\text{m}}|_{\text{p.f.}} = \sum_s (3w_s - 1) \tilde{\rho}_s$. We have $\tilde{\rho}_s \propto (Aa)^{-3(1+w_s)} \equiv A^{-3(1+w_s)} \rho_s$, where $\rho_s = a^{-3(1+w_s)}$ defines a scaled energy density, conserved in the Einstein frame, and a the Einstein-frame scale factor. Now

$$\square\phi = V_{,\phi}(\phi) - A_{,\phi}(\phi) \sum_s A^{-3w_s}(\phi) (3w_s - 1) \rho_s, \quad (3.11)$$

which for near-constant ρ_s reduces to $\square\phi = V_{\text{eff},\phi}$ where [21]

$$V_{\text{eff}} = V(\phi) + \sum_s A^{1-3w_s}(\phi) \rho_s \quad (3.12)$$

is the effective potential \star .

Check if this is only symmetron.

Review

Matter particles in the Jordan frame obey the simple geodesic equation as there is no coupling to ϕ . On the other hand, particles in the Einstein frame matter sector experience a **fifth force** due to the universal coupling. The fifth force concept captures the non-trivial right-hand side of in the geodesic equation,†

$$\mathbf{x}_{,tt} \supset \frac{\mathbf{F}_5}{m} = -\frac{\beta}{M_{\text{Pl}}} \nabla\phi. \quad (3.13)$$

‡ β is then a measure of the strength of the fifth force relative to the Newtonian gravitational force.

The dynamic equation-of-state parameter is

$$w_\phi = \frac{\rho_\phi}{p_\phi} = \frac{\frac{1}{2a^2} \dot{\phi}^2 - V(\phi)}{\frac{1}{2a^2} \dot{\phi}^2 + V(\phi)}, \quad (3.14)$$

for which $\lim_{\dot{\phi} \rightarrow 0} w_\phi = w_\Lambda = -1$. These models are thus often proposed in context of dark-energy models to explain the accelerated cosmic expansion. We will not consider this directly in this project.

3.2.2 Asymmetron model

The particular quintessence model characterised by the symmetric Mexican-hat potential

$$V(\phi) = \frac{\lambda}{4}\phi^4 - \frac{\mu^2}{2}\phi^2 + V_0 \quad (3.15)$$

is called the **symmetron** model [21]. This theory is invariant under reflection, $\phi \rightarrow -\phi$, (ϕ is \mathbb{Z}_2 symmetric) a **requirement from quantum theory**.[©] (IF TIME? COMMENT ON THIS.) Not equally well-established is the generalisation of this model called the **asymmetron** [30], in which the potential is given an additional cubic term, $V(\phi) \supset -\kappa\phi^3/3$. Here, one of the domains is favoured over the other.

Now, why would we want this asymmetry in the first place? It complicates things by breaking the \mathbb{Z}_2 symmetry of the symmetron, so the theory only holds approximately. However, this asymmetry can aid in overcoming the domain wall problem, manifest in the inevitable biased domain wall collapse. We mentioned this briefly in Section 3.1.2. We stress that introducing asymmetry in this way is different from energy bias in the sense that not only is the energy in the two domains different, but the expectation values for ϕ are shifted.

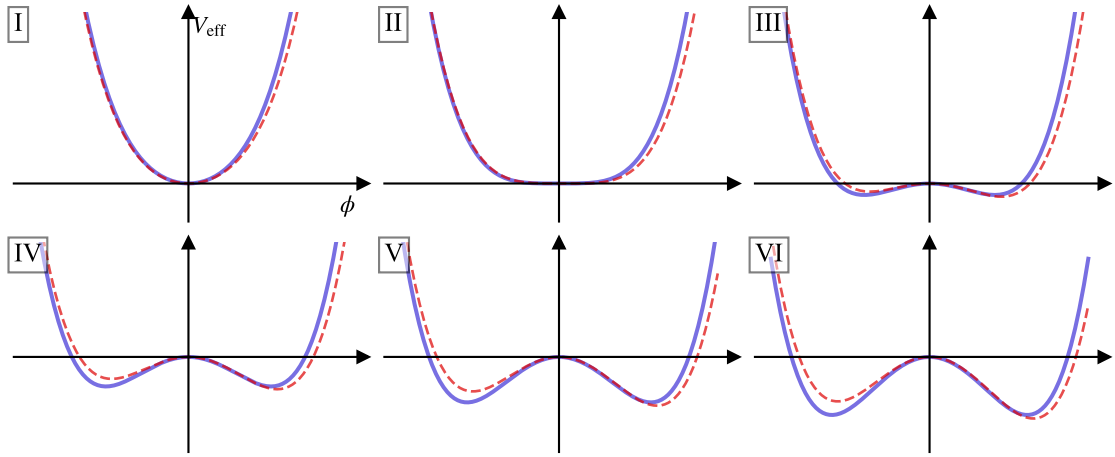


Figure 3.2: The evolution of the (a)symmetron effective potential in (dashed red) solid blue. **Describe time.** (IF TIME? ADD TWO BALLS.

The simplest symmetron model has the quadratic coupling

$$A(\phi) = 1 + \frac{1}{2}\left(\frac{\phi}{M}\right)^2 + \mathcal{O}\left((\phi/M)^4\right). \quad (3.16)$$

We consider the matter content to be dust-like, so that $\tilde{T}_m \simeq -\tilde{\rho}$. The effective potential is then given by [21]★

$$V_{\text{eff}}(\phi) = \frac{\lambda}{4}\phi^4 - \frac{\kappa}{3}\phi^3 + \frac{\mu^2}{2}\left(\frac{\rho}{\mu^2 M^2} - 1\right)\phi^2 + V_0. \quad (3.17)$$

This potential becomes unstable when $\rho \leq \mu^2 M^2 \equiv \rho_*$, and the field rolls into either of the two vacua. From the cosmological perspective, ignoring κ , we imagine an initially dense region in the universe where a scalar field oscillates slightly around zero. The energy density dilutes and eventually reaches $\rho = \rho_*$, spontaneously breaking the \mathbb{Z}_2 symmetry, and separates the scalar field into domains according to their sign at the time. A schematic of this evolution is shown in Fig. 3.2. The potential barriers created at this *phase transition* correspond to the topological solitons discussed in Section 3.1.2; namely cosmic domain walls.

Let $v \equiv \rho/(\mu^2 M^2)$. By setting $V_{\text{eff},\phi} = 0$, we find the vacuum expectation values (VEVs)

$$\phi_0 = 0 \quad \vee \quad \phi_{\pm} = \phi_{\infty} \left(\bar{\kappa} \pm \sqrt{\bar{\kappa}^2 + 1 - v} \right), \quad (3.18)$$

where we defined $\bar{\kappa} = \kappa/(2\mu\sqrt{\lambda})$ and $\phi_{\infty} = \mu/\sqrt{\lambda}$. Note that for the symmetron ($\kappa = 0$), since the field is real, VEV is zero before SSB. We determine the stability of these vacua by evaluating $V_{\text{eff},\phi\phi}$ at $\phi = \phi_0, \phi_{\pm}$ and see that ϕ_0 remains stable until $\rho = \rho_*$.⁵

Screening

In this context, a **screening mechanism** is a property of the model that removes the effect of the extra scalar field in the appropriate environment. The symmetron scalar field mediates fifth forces in low-density environments while being screened in dense regions. We illustrate this in Fig. 3.3.

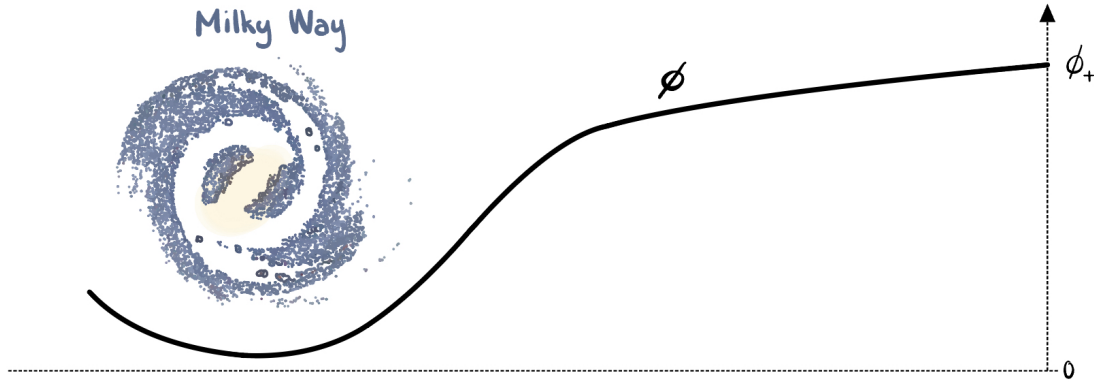


Figure 3.3: Schematic of the symmetron screening mechanism. It is clear that the vacuum expectation value goes to zero in dense regions. This example assumes a symmetron with Compton length scale $L_C \sim \mathcal{O}(\text{kpc})$ [7]. Illustration based on Christiansen [9].

Free parameters

The quartic coupling constant λ measures the scalar self-interactions and μ defines the bare mass of the (a)symmetron. The cubic coupling κ is a measure of the difference between the two vacua, and is zero in the symmetron case. The constant V_0 can be interpreted as a cosmological constant Λ [10], but we will not discuss this here. The conformal coupling scale M governs the matter coupling strength [7]. We introduce the **symmetron Compton wavelength**

$$L_C = \frac{1}{\sqrt{2}\mu} \quad (3.19)$$

which defines the range of the symmetron forces. Local tests of gravity require $M \lesssim 10^{-3} M_{\text{Pl}}$ for the quadratic coupling [7, 20, 21]. This is to say that fifth forces is mediated within a range $L_C \lesssim \text{Mpc}$ [20].

3.3 Classification of topological defects

IF TIME: WRITE SHORT ABOUT CLASSIFICATION, HOMOTOPY GROUP, ETC., [17, 36]

⁵This is not entirely true for the asymmetron, but we will not discuss this here.

Part II

Methodology

Chapter 4

Imperfect Defects

Any cosmologically relevant domain wall will be thin compared to the horizon [31]. Are they sufficiently thin so that the thin-wall approximation holds? If so, we should be able to study the dynamics of such walls by viewing them as $(2 + 1)$ -dimensional timelike hypersurfaces in a spacetime of $3 + 1$ dimensions. By Nambu–Goto theory and an action principle, one can derive an equation governing the dynamics of this worldsheet [36]. In fact, this is the same for any hypersurface of d dimensions, thus relevant for several types of defects. In particular, this concerns the codimension-one defects, as higher-codimension defects cannot generally be thought of as hypersurfaces, but submanifolds in any case [35].

To substantiate the applicability of this theory, we begin in a more general picture than what we eventually will require. We consider a d -dimensional timelike ($\zeta = +1$ in Eq. (2.7)) submanifold Σ embedded in smooth Riemannian manifold \mathcal{M} of one time dimension and $n - 1$ spatial dimensions. We let Σ have codimension one ($d = n - 1$) and split the ambient space into two separate hypervolumes. Now, Σ is a timelike hypersurface of \mathcal{M} that can be interpreted as the d -dimensional analogue of an infinitely thin domain wall.

We will use this to explore the dynamics of domain walls in the thin-wall limit, where the emphasis is not on the symmetry-breaking scalar field ϕ , but of the position and evolution of the domain wall itself. There exists analytical solutions to the equation of motion for linear perturbations to the *planar* wall position in expanding spacetime. We derive this equation for conventional, static walls and propose a version of this applicable to the defect during phase transition (when the surface energy density is changing).

Now, static, symmetric walls do not produce gravitational radiation by themselves. We will use the dynamics of a wiggly domain wall as source to tensorial metric perturbations, a.k.a. gravitational waves.

The chapter is outlined as follows. In Section 4.1 we review the general formula for dynamics of topological defects. In Section 4.2 we look at domain walls in a general spacetime, as well as perturbations to planar domain walls in an FLRW universe. We implement the symmetron description of these walls in Section 4.3 and solve the linear perturbation in a matter-dominated universe. In Section 4.4 we review the gravitational waves sourced by the Nambu–Goto stress–energy tensor.

4.1 Formal treatment of defect dynamics

In this fairly technical section we follow Garriga and Vilenkin [18] and Ishibashi and Ishihara [22]. In mathematical terms, we consider a smooth spacetime

$$\mathcal{M} = (\mathbb{R}^{n-1,1}, g_{\mu\nu}) \supset \Sigma = (\mathbb{R}^{d-1,1}, \gamma_{ab}) \quad (4.1)$$

where $d = n - 1$ and indices $a, b, c = 0, 1, \dots, d - 1$, while Greek indices as usual runs from 0 to $n - 1$. Let the world sheet Σ divide \mathcal{M} into two hypervolumes \mathcal{M}_\pm such that $\mathcal{M} = \mathcal{M}_+ \cup \Sigma \cup \mathcal{M}_-$. We invoke a smooth coordinate system $\{x^\mu\}$ of the spacetime in a neighbourhood of Σ . The embedding of Σ in \mathcal{M} is $x^\mu = X^\mu(\xi^a)$, where the coordinate system $\{\xi^a\}$ parametrises Σ . The induced metric on Σ is

$$\gamma_{ab} = g_{\mu\nu} e_a^\mu e_b^\nu, \quad e_a^\mu \equiv X^\mu_{,a} = \partial X^\mu / \partial \xi^a. \quad (4.2)$$

e_a^μ are the tangent vectors and n^μ the unit normal vector pointing from Σ to \mathcal{M}_+ , obeying

$$g_{\mu\nu} n^\mu n^\nu = 1 \quad \text{and} \quad g_{\mu\nu} e_a^\mu n^\nu = 0. \quad (4.3)$$

The action for the system is [22]

$$S = -\sigma \int_\Sigma d^d \xi \sqrt{-\gamma} - v_+ \int_{\mathcal{M}_+} d^n x \sqrt{-g} - v_- \int_{\mathcal{M}_-} d^n x \sqrt{-g}. \quad (4.4)$$

The first term is called the Nambu–Goto action S_{NG} , with σ representing the constant positive energy density of the defect in its rest frame. The rest is the vacuum action S_{vac} given through the constant potential energy densities v_\pm of \mathcal{M}_\pm .

Let us consider the variation of S under small changes in the world sheet, $X^\mu \rightarrow X^\mu + \delta X^\mu$. Since only transverse motion is physically relevant, we can write the variation in terms of the small, but otherwise arbitrary, function $\psi(\xi^a)$;

$$X^\mu \rightarrow X^\mu + \psi n^\mu. \quad (4.5)$$

The equation of motion for the normal coordinate is then [18, 22]

$$n_\mu \widehat{\square} X^\mu + n_\mu \Gamma_{\kappa\tau}^\mu \gamma^{ab} X^\kappa_{,a} X^\tau_{,b} + \frac{v}{\sigma} = 0, \quad (4.6)$$

where $v = v_+ - v_-$ is the difference in vacuum energies,

$$\widehat{\square} = \widehat{\nabla}^a \widehat{\nabla}_a = \frac{1}{\sqrt{-\gamma}} \partial_a (\sqrt{-\gamma} \gamma^{ab} \partial_b) \quad (4.7)$$

is the d'Alembertian associated with Σ , and $\Gamma_{\kappa\tau}^\mu$ are the spacetime Christoffel symbols. This can be written in the simple form

$$\gamma^{ab} \widehat{K}_{ab} = -\frac{v}{\sigma}, \quad (4.8)$$

where the extrinsic curvature tensor (Eq. (2.8)) is

$$\widehat{K}_{ab} = -e_a^\mu e_b^\nu \nabla_\nu n_\mu. \quad (4.9)$$

Exact solutions

IF TIME: MENTION MINKOWSKI, $v = 0$, STRINGS, GAUGE INVARIANCE.

Minkowski. In Garriga and Vilenkin [18] it is shown that a planar domain wall oriented perpendicular to the z axis in Minkowski space follows the trajectory $z = z(t)$ whose equation of motion is

$$\frac{z_{,tt}}{(1 - z_{,t}^2)^{3/2}} = \frac{v}{\sigma}. \quad (4.10)$$

With $v = 0$ the solution is $z(t) = 0$ in a suitable Lorentz frame. With non-degenerate vacua, the solution is the hyperbola [18].

Strings in expanding spacetime. IF TIMES FILL IN.

4.1.1 Linearised perturbations

Let X^μ solve the equation of motion for the defect. We denote the perturbed solution \hat{X}^μ . Only transverse motion is physically observable, and so

$$\hat{X}^\mu = X^\mu + \delta X^\mu = X^\mu + \epsilon(\xi^a)n^\mu,^1 \quad (4.11)$$

where the wall displacement variable ϵ is a linear perturbation ($\epsilon^2 \simeq 0$), and n^μ is the unit normal vector to the *unperturbed* worldsheet [36]. To find the equation of motion for ϵ s we apply Eq. (4.11) to Eq. (4.8) and solve order by order. If the ambient space is Minkowski, this amounts to [18]

$$\widehat{\square}\epsilon + \widehat{K}^{ab}\widehat{K}_{ab}\epsilon = 0; \quad g_{\mu\nu} = \eta_{\mu\nu}. \quad (4.12)$$

4.1.2 Energy and momentum

From the Nambu–Goto action S_{NG} , we can construct an effective energy–momentum tensor associated with the defect

$$T^{\mu\nu}|_{\text{NG}} = \frac{2}{\sqrt{-g}} \frac{\delta S_{\text{NG}}}{\delta g_{\mu\nu}}. \quad (4.13)$$

Consider $X^\mu = \xi^a e_a^\mu + X_\perp n^\mu$. By rewriting the action to the spacetime integral

$$S_{\text{NG}} = -\sigma \int_{\mathcal{M}} d^n x \sqrt{-\gamma} \delta(r); \quad r \equiv n_\mu x^\mu - X_\perp, \quad (4.14)$$

where the Dirac delta function essentially eliminates any spacetime event that is *not* the defect. The variation $g_{\mu\nu} \rightarrow g_{\mu\nu} + \delta g_{\mu\nu}$ gives [35, 36]

$$T^{\mu\nu}|_{\text{NG}} = \frac{\sigma}{\sqrt{-g}} \int d^d \xi \sqrt{-\gamma} \gamma^{ab} X_{,a}^\mu X_{,b}^\nu \delta(r), \quad (4.15)$$

or equivalently

$$T^{\mu\nu}|_{\text{NG}} = \frac{\sigma \delta(r)}{\sqrt{-g} \sqrt{-\gamma}} \frac{\delta \gamma}{\delta g_{\mu\nu}}. \quad (4.16)$$

Maybe mention $d\gamma = \gamma \gamma^{ab} d\gamma_{ab}$?

4.2 Domain wall dynamics

So far, we have addressed the very general Nambu–Goto picture. From here, we turn our attention to $(2 + 1)$ -dimensional topological defects living in $(3 + 1)$ -dimensional spacetime, i.e. domain walls. Let $v = v_+ - v_- = 0$. We describe the wall position in \mathcal{M} with $x^\mu = X^\mu(\xi^a)$ where $\mu = 0, 1, 2, 3$ and $a = 0, 1, 2$., and impose coordinates that satisfy

$$ds^2 = dY^2 + \gamma_{ab} d\xi^a d\xi^b, \quad (4.17)$$

where Y is the normal distance Σ [36]. With Eq. (4.2) and the identity $\delta \gamma = \gamma \gamma^{ab} \delta \gamma_{ab}$, we obtain [36]

$$\widehat{\square} X^\mu + \Gamma_{\kappa\tau}^\mu \gamma^{ab} X_{,a}^\kappa X_{,b}^\tau = 0, \quad (4.18)$$

¹Formally, this is the same as the variation above, but now we are dealing with a physical perturbation as opposed to a mathematical variation.

which is a repetition of Eq. (4.6) with degenerate vacua. According to Vilenkin and Shellard [36] (This was 1994, so maybe outdated?), no known gauge choice can reduce Eq. (4.18) to an exactly solvable linear equation. If X^μ is a known solution, we can study a linear perturbation to this instead, with the perturbed wall trajectory in Eq. (4.11).

4.2.1 Planar walls in expanding spacetime

Assume we have the unperturbed wall parallel to the xy -plane of an expanding spacetime

$$ds^2 = a^2 ds^2|_M = a^2(-d\tau^2 + d\mathbf{x}^2), \quad (4.19)$$

where $\mathbf{x} = (x, y, z)$ are the comoving Cartesian coordinates. We fix the gauge $\xi^a = (\tau, x, y)$ so that $z = z_w = z_0 + \epsilon(\tau, x, y)$ uniquely describes the wall motion. The Nambu–Goto action reads

$$S_{\text{NG}} = -\sigma \int d^3\xi \sqrt{-\gamma} = -\sigma \int d\tau a^3(\tau) \int dx \int dy h(\tau, x, y) \quad (4.20)$$

where

$$h \triangleq a^{-3} \sqrt{-\gamma} = \sqrt{1 + \epsilon^{,a} \epsilon_{,a}}. \quad (4.21)$$

The equation of motion for the wall becomes [36]

$$-\partial^a(\epsilon_{,a}/h) + 3\mathcal{H}\epsilon_{,\tau}/h = 0, \quad (4.22)$$

where $\mathcal{H} = a_{,\tau}/a$ is the conformal Hubble factor. We let ϵ be a linear perturbation such that $\epsilon^2 \rightarrow 0$ and consider power-law expansion, $a \propto \tau^\alpha$. Now,

$$\epsilon_{,\tau\tau} + 3\mathcal{H}\epsilon_{,\tau} - \epsilon_{,xx} - \epsilon_{,yy} = 0 \quad (4.23)$$

is the equation for the first-order displacement field. This is a separable partial differential equation (PDE) and we assume solutions of the form $\epsilon(\tau, x, y) = \varepsilon(\tau)\mathcal{E}(x, y)$. Now, we separate Eq. (4.23) into

$$\ddot{\varepsilon} + \mathcal{D}(\tau)\dot{\varepsilon} + p^2\varepsilon = 0 \quad \text{and} \quad \mathcal{E}_{,xx} + \mathcal{E}_{,yy} + p^2\mathcal{E} = 0, \quad (4.24)$$

where $\mathcal{D}(\tau) = \mathcal{H}(\tau)$. The spatial part has solutions that are linear combinations of $\sin(p_x x + p_y y)$ and $\cos(p_x x + p_y y)$, with $p_x^2 + p_y^2 = p^2$. The solutions to this equation are of the form $\varepsilon = \tau^\nu Z_\nu(p\tau)$ with $\nu = (1 - 3\alpha)/2$ (see Appendix A).

Energy and momentum

To some extent, we can account for a possibly non-vanishing wall half-width $l \sim \delta$ by choosing a Gaussian function instead of a Dirac delta distribution. Simply substituting

$$\delta(r) \rightarrow \Phi_l(r) \equiv \frac{1}{\sqrt{2\pi}l} \exp\left\{-\frac{r^2}{2l^2}\right\} \quad (4.25)$$

in Eq. (4.16) does the trick, and restores $\delta(r)$ in the limit where $l \rightarrow 0$. This is understood in context with Section 3.1.2, where we argue that $l = \delta/\sqrt{2}$ gives a suitable Gaussian profile. Note that this is not the same as going beyond the thin-wall limit, but rather an approximation that includes a thickness that is small enough to not alter the dynamics. Domain walls of cosmological relevance will have thickness much smaller than the horizon [18]. However, some models will have instances in time when this is not true, and the thickness in fact varies.

We perform the variation in Eq. (4.16) for the scenario in question to find the SE tensor associated with the wall motion. The detailed calculation is found in Appendix B.3.1. The non-vanishing spatial components are

$$\begin{aligned} W_{ab} &= -a\sigma_w \Phi_l(z - z_w) \cdot \eta_{ab}, \\ W_{(i3)} &= -a\sigma_w \Phi_l(z - z_w) \cdot \epsilon_{,i}, \end{aligned} \quad (4.26)$$

where indices $a, b = 0, 1, 2$ and $z_w = z_0 + \epsilon$. The tensor $W^{\mu\nu}$ refers to the stress–energy tensor associated with a particular domain wall by Eq. (4.16).

4.2.2 Time-dependent surface tension

Until now, the theory is model-independent in the sense that we have not assumed any particular type of domain wall (or defect, in general). This dependence is encoded in the *constant* surface tension σ and difference in vacuum energies $v = v_+ - v_-$. It is plain to see from Eq. (4.8) that the absence of energy bias removes the surface-tension dependence. But what if the surface tension is not constant?

If we allow the surface tension to vary, $\sigma = \sigma(\tau)$, we need to put this inside of the integral in the Nambu–Goto action in Eq. (4.20). The calculation is presented in Appendix B.3. We immediately see that this is equivalent to letting $a^3 \rightarrow a^3 \sigma$, which amounts to

$$\mathcal{D}(\tau) = \frac{3}{a\sigma^{1/3}} \frac{da\sigma^{1/3}}{d\tau} = 3\frac{\dot{a}}{a} + \frac{\dot{\sigma}}{\sigma} = 3\frac{d \ln a}{d\tau} + \frac{d \ln \sigma}{d\tau} \quad (4.27)$$

in Eq. (4.24). We get

$$\ddot{\epsilon} + (3\dot{a}/a + \dot{\sigma}/\sigma)\dot{\epsilon} + p^2\epsilon = 0. \quad (4.28)$$

This extra term will introduce the model-dependence. We show in Appendix B.2 that the surface tension in the thin-wall approximation is

$$\sigma_w \simeq \int_{\phi_-}^{\phi_+} d\phi \sqrt{2V_{\text{eff}}(\phi) - 2V_{\text{eff}}(\phi_{\pm})}, \quad (4.29)$$

where $V_{\text{eff}}(\phi)$ is the effective potential of the scalar field theory.

4.3 Symmetron walls

The symmetron effective potential in Eq. (3.17) is designed to induce phase transition at conformal time τ_* , or scale factor a_* . Inserting this into Eq. (4.29), we find that the surface tension of a thin symmetron domain wall is

$$\sigma = \sigma_\infty(1 - v)^{3/2}; \quad v = (a_*/a)^3, \quad (4.30)$$

where σ_∞ is the vacuum surface energy density (Eq. (3.7)).

From here it becomes advantageous to introduce some new, dimensionless variables. We will use $s \equiv \tau/\tau_*$ as our time variable, and $\omega \equiv p\tau_*$ as the eigenvalue, when it comes to that. In a universe with $a = a_* s^\alpha$ we have $v = s^{-3\alpha}$ and thus

$$\frac{\sigma'}{\sigma} = \frac{d \ln \sigma}{ds} = \frac{9\alpha}{2s(s^{3\alpha} - 1)}, \quad (4.31)$$

where primes mean derivatives with respect to s . Finally, the equation of motion for the scalar perturbation to the wall normal coordinate is

$$\varepsilon'' + \left(\frac{3\alpha}{s} + 2d(s) \right) \varepsilon' + \omega^2 \varepsilon = 0; \quad d(s) \equiv \frac{9\alpha}{4s(s^{3\alpha} - 1)}. \quad (4.32)$$

TO-DO: Check if this is a misunderstanding, as ρ in effective potential is manifestly dust-like?

4.3.1 Solution in matter-dominated universe

This work only truly experiments in a universe with, and only with, homogeneous matter distribution, i.e. $\alpha = 2$ and $\sum_s \Omega_{s0} = \Omega_{m0} = 1$. Generalisation of the following to other α should in principle be trivial, but at some point in the following we require $\alpha \geq 1/3$, and so a different analysis would be required for smaller α .

So, restricting our discussion to $\alpha = 2$, we continue with the planar domain wall placed parallel to the xy -plane, spontaneously formed at symmetry break, $s = 1$. Assume an initial perturbation of amplitude ε_* was given to the wall. We consider the solution to Eq. (4.32) that has eigenvalue $\omega = p\tau_*$ and restrict $\max |\mathcal{E}(x, y)| = 1$ for the spatial part. With initial conditions $\varepsilon(s = 1) = \varepsilon_*$ and $\varepsilon'(s = 1) = 0$, we shall solve

$$\varepsilon'' + \left(\frac{6}{s} + \frac{9}{2s(s^6 - 1)} \right) \varepsilon' + \omega^2 \varepsilon = 0 \quad (4.33)$$

analytically in two regimes, and sow these solutions together in the region where they overlap. For notational ease, we write $\varepsilon(s) = \varepsilon_* e(s)$.

Shortly after symmetry breaking. We begin by solving the equation of motion for $s \sim 1$. As our equation has a singularity at $s = 1$, the natural way to go is through a Laurent expansion around this point of the damping term in Eq. (4.33). We find

$$\frac{6}{s} + \frac{9}{s(s^6 - 1)} = \frac{3}{2}(s - 1) + \frac{3}{4} + \frac{29}{8}(s - 1) - \frac{93}{16}(s - 1)^2 + \mathcal{O}((s - 1)^3). \quad (4.34)$$

Now $e(s)$ is also subject to an expansion around $s = 1$;

$$e^{(0)}(s) = \left[1 + c_1(s - 1) + c_2(s - 1)^2 + c_3(s - 1)^3 + \dots \right]. \quad (4.35)$$

When put together, we get a polynomial in $(s - 1)$ on the left-hand side of Eq. (4.33), for which all coefficients must vanish. We solve the system of equations for $\{c_1, c_2, c_3\}$ and find

$$e^{(0)}(s) = \left[1 - \frac{\omega^2}{5}(s - 1)^2 + \frac{\omega^2}{35}(s - 1)^3 \right] + \mathcal{O}((s - 1)^4). \quad (4.36)$$

Adiabatic evolution. The extra damping term $2d(s) = 9/(2s(s^6 - 1))$ initially changes extremely rapidly from very large values, before it becomes very small compared to $3a'/a = 6/s$. We expect the solution to quickly approach that of Eq. (4.24) as $s \gg 1$. Said damping term is not completely negligible, however, as it causes a *damping envelope* that is considered much like in the case of a damped harmonic oscillator. We write

$$e^{(m)}(s) \simeq \zeta(s) \cdot \exp \left\{ - \int^s dt d(t) \right\}. \quad (4.37)$$

Employing this ansatz in the equation of motion gives

$$\zeta'' + \frac{6}{s}\zeta' + (\omega^2 - \theta(s))\zeta = 0; \quad \theta(s) = d'(s) + d^2(s) + \frac{6}{s}d(s), \quad (4.38)$$

whose solution is $\zeta(s) \simeq s^{-5/2}Z_{-5/2}(\omega s)$ when the phase shift introduced by $\theta(s)$ is negligible.² Now, we find that $\exp\{-\int^s dt d(t)\} = s^{9/2}(s^6 - 1)^{-3/4} \cdot \text{constant}$. Thus,

$$e^{(\text{III})}(s) \simeq \frac{AJ_{-5/2}(\omega s) + BY_{-5/2}(\omega s)}{s^{5/2}} \frac{s^{9/2}}{(s^6 - 1)^{3/4}}, \quad (4.39)$$

where A and B are constants to be determined.

Complete evolution. We use a computer algebra system, namely *SageMath* [34], to determine A and B from the system of equations

$$\begin{aligned} e^{(\text{I})}(s = s_{\text{sow}}) &= e^{(\text{III})}(s = s_{\text{sow}}), \\ e^{(\text{I})'}(s = s_{\text{sow}}) &= e^{(\text{III})'}(s = s_{\text{sow}}), \end{aligned} \quad (4.40)$$

⌈maybe put expressions in appendix?⌋ where we choose $s_{\text{sow}} = 1 + \omega^{-1}$, since only subhorizon modes, $\omega \gg 1$, are of interest. Now,

$$\mathcal{E}(s) = \varepsilon_* \cdot \begin{cases} e^{(\text{I})}(s) & \text{if } s \leq s_{\text{sow}}, \\ e^{(\text{III})}(s) & \text{if } s \geq s_{\text{sow}}. \end{cases} \quad (4.41)$$

In Fig. 4.1 we demonstrate how this solution looks like for arbitrary ω , in the different steps described above.

4.3.2 TITLE (Review)

We see that the initial amplitude ε_* can be factored out and does not affect the evolution of the wall. However, we need to keep in mind that this should be small enough to satisfy $(\varepsilon_*/\tau_*)^2 \simeq 0$.

We ignore x -dependence in ϵ and impose Dirichlet boundary conditions $\mathcal{E}(y = 0) = \mathcal{E}(y = \tau_*) = 0$. We write the complete solution in terms of eigenvalues $p^{(n)} = \pi n/\tau_*$,

$$\epsilon(\tau, y) = \varepsilon_* \sum_{n=0}^{\infty} \{a_n F_a(s; \pi n) + b_n F_b(s; \pi n)\} \sin(p^{(n)}y); \quad \max \epsilon(\tau_*, y) = \varepsilon_*, \quad (4.42)$$

where $F_{a,b}(s; \omega^{(n)})$ are the linearly independent solutions to Eq. (4.33). This makes $\epsilon = \varepsilon(\tau) \sin py$ a simple solution to the full equation, where ε solves Eq. (4.33).

IF TIME1 SCALING WHEN $t_\omega = \omega(s - 1)$ IS USED AS A TIME VARIABLE

IF TIME1 ASYMMETRON, $v > 0$

4.4 From domain wall wiggles to spacetime ripples

Planar domain walls do not themselves produce gravitational radiation. Introducing asymmetry to the system, as we do when adding perturbations, can give rise to non-vanishing stress–energy tensor components in the TT gauge. In this section we present the gravitational-wave calculations in the case of a planar, thin domain wall in a conformally flat universe with expansion rate a . We neglect back-reaction, that is we assume that the defect does not change the unperturbed background metric.

²In fact, it is possible to show that $\lim_{\omega \rightarrow \infty} [\sqrt{\omega^2 - \theta(1 + \omega^{-1})} - \omega]/\omega = \sqrt{19}/4 - 1 \approx 0.09$.

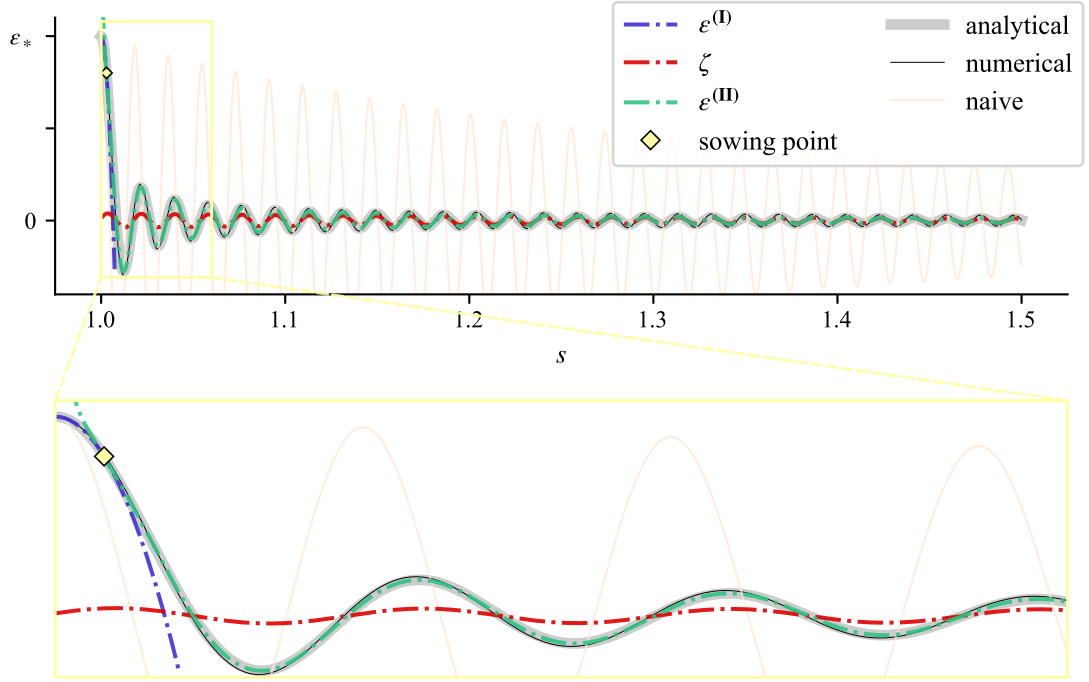


Figure 4.1: Schematic demonstrating how the analytical solution to the equation of motion for $\varepsilon(s)$. The numerical solution is included, both in the case with constant (“naive”) and time-varying (numerical) surface tension.

4.4.1 Gravitational waves in expanding universe

From Section 2.4.1 we have the calculation of $\tilde{h}_{ij}(\tau, \mathbf{k})$ in a universe with $a \propto \tau^\alpha$, specified for $\alpha \in \mathbb{Z}$. Assuming homogeneous initial conditions at $\tau_i = \tau_*$, the tensor perturbations are given by Eq. (2.53) and Eq. (2.52) with $n = \alpha - 1$. For convenience, we use a linear polarisation basis (see Section 2.4) and the decomposition $\tilde{\psi}_P = a\tilde{h}_P = H_P^1 + H_P^2$, $P = +, \times$, such that [24]

$$H_P^{1,2}(\tau, \mathbf{k}) = \pm R_n^{(1,2)}(k\tau) \int_{\tau_*}^{\tau} d\hat{\tau} R_n^{(2,1)}(k\hat{\tau}) f_P(\hat{\tau}, \mathbf{k}). \quad (4.43)$$

The function f_P , given in Eq. (2.50), contains the TT-projected, Fourier-transformed stress–energy tensor. The conformal time derivative $\dot{\psi} = \dot{H}_P^1 + \dot{H}_P^2$ is given by

$$\dot{H}_P^{1,2}(\tau, \mathbf{k}) = \pm k \left[R_\alpha^{(1,2)}(k\tau) - n Z_n^{(1,2)}(k\tau) \right] \int_{\tau_*}^{\tau} d\hat{\tau} R_n^{(2,1)}(k\hat{\tau}) f_P(\hat{\tau}, \mathbf{k}). \quad (4.44)$$

Note that $\dot{h} = a^{-1}(\dot{\psi} - \dot{a}\psi)$ is the conformal time derivative of the gravitational waves. We repeat that $R^{(i)}$ and $Z^{(i)}$ are the Riccati– and spherical Bessel functions of i th kind, respectively, reported in Appendix A.

4.4.2 Fourier-space stress–energy tensor

In Section 4.2 we found that the SE tensor of a thin domain wall in an expanding universe looks like Eq. (4.26). For the case of a wall in the xy -plane, this reduces to

$$\begin{aligned} W_{ab}(\tau, \mathbf{x}) &= -a(\tau)\sigma_w(\tau)\Phi_l(z - z_w)\eta_{ab}, \\ W_{iz}(\tau, \mathbf{x}) &= -a(\tau)\sigma_w(\tau)\Phi_l(z - z_w)\epsilon_{,i}, \end{aligned} \quad (4.45)$$

where σ_w is the wall's surface tension, $z_w = z_0 + \epsilon(x^d)$ the wall normal coordinate and Φ_l is a Gaussian with standard deviation $l = l_w \triangleq \delta_w / \sqrt{2}$. We go further and look at this quantity in Fourier space:

$$\begin{aligned}\tilde{W}_{ab}(\tau, \mathbf{k}) &= -a(\tau)\sigma_w(\tau)\eta_{ab}\mathcal{D}_w(\tau, k_z)\int d^2x e^{ik_z\epsilon}e^{i(k_x x + k_y y)}, \\ \tilde{W}_{iz}(\tau, \mathbf{k}) &= -a(\tau)\sigma_w(\tau)\mathcal{D}_w(\tau, k_z)\int d^2x \epsilon_i e^{ik_z\epsilon}e^{i(k_x x + k_y y)},\end{aligned}\quad (4.46)$$

where $\mathcal{D}_w = \exp\{ik_z z_0 - (k_z l_w)^2/2\}$ adjusts for wall width and unperturbed distance from the xy -plane. Let us assume $\epsilon_{,x} = 0$ s.t. $\epsilon(\tau, x, y) = \epsilon(\tau)\mathcal{E}(y)$ with eigenvalue p^2 . Now

$$\underbrace{\int dy e^{ik_z\epsilon(\tau)\cdot\mathcal{E}(y)}e^{ik_y y}}_{\equiv I_s} \quad \text{and} \quad \underbrace{\epsilon(\tau)\int dy \partial_y \mathcal{E} e^{ik_z\epsilon(\tau)\cdot\mathcal{E}(y)}e^{ik_y y}}_{\equiv I_a} \quad (4.47)$$

are all we need to solve to have a completely analytic expression for \tilde{W}_{ij} .

We choose a linear polarisation basis (Section 2.4). As there is no dependence on x in real space, there is a proportionality to $\delta(k_x)$ in Fourier space. Considering $\mathbf{k} = (0, k_y, k_z)$ leaves only one degree of freedom, and we see that

$$\tilde{W}_{ij}|_{\text{TT}} = \Lambda_{ij}^{kl}\tilde{W}_{kl} = \sum_{P=+, \times} \tilde{W}_P e_{ij}^P = \tilde{W}_+ e_{ij}^+. \quad (4.48)$$

In addition, we get $\tilde{W}_+ = \tilde{W}_{xx}|_{\text{TT}}$. From here, we work with $\tilde{\pi}_+^w = \tilde{\pi}_{xx}^w = a^{-2}\Lambda_{xx}^{ij}\tilde{W}_{ij}$. Applying the spin-2 projector (Eq. (7)) and using Eq. (4.46), we find that

$$a^2\tilde{\pi}_+^w = \tilde{W}_+ = \frac{k_y}{2k^2}\{k_y\tilde{W}_{xx} + 2k_z\tilde{W}_{xy}\}. \quad (4.49)$$

DELETE ME:<

$$e_{ij}^+(k) = \frac{1}{k^2} \begin{pmatrix} k^2 & 0 & 0 \\ 0 & -k_z^2 & k_y k_z \\ 0 & k_y k_z & -k_y^2 \end{pmatrix}_{ij} \quad \wedge \quad e_{ij}^\times(k) = \frac{1}{k} \begin{pmatrix} 0 & k_z & -k_y \\ -k_z & 0 & 0 \\ k_y & 0 & 0 \end{pmatrix}_{ij} \quad (4.50)$$

>

Spatial part

For simplicity, we choose $\mathcal{E}(y) = \sin py$. In Appendix B.4 we show that this implies

$$a^2\tilde{\pi}_+^w = -\frac{k_y^2}{2k^2}\tilde{W}_{xx}. \quad (4.51)$$

The explicit calculation gives

$$\tilde{\pi}_+^w = 2\pi^2\delta(k_x)(k_y/k)^2 a^{-1}\sigma_w\mathcal{D}_w \sum_{n \in \mathbb{Z}} \delta(k_y + np)\mathcal{J}_n(k_z\epsilon), \quad (4.52)$$

which we use to compute \tilde{h}_+ .

Chapter 5

Cosmic Phase Transitions

Discrete symmetry breakage leads to formation of domain walls [36]. We may apply thin-wall dynamics when the thickness parameter δ is negligible compared to other dimensions of the problem, primarily the horizon size [36]. Otherwise, we must employ the full field theory. During a phase transition in which the dynamics is governed by a reflection-invariant Lagrangian in $3 + 1$ dimensions, the system quickly divides into alternating positive and negative vacuum domains. Separating these are domain walls, which during transition is thinning from initially (as we will see) infinite thickness.¹

In this chapter we attack the field-theoretical approach to describing the motion of domain walls, during and after phase transition. We eventually take leave of one spatial dimension, and so the framework can also describe strings [6]. Previous work [6] has been done on Minkowski background in the static picture. The following analysis assumes a conformally flat, homogeneous and isotropic background, particularly one with scale factor $a \propto \tau^\alpha$. We consider the entire phase transition, i.e. the actual formation of defects, which alters the dynamics in the Nambu–Goto picture. We build up towards simulations of toy scenarios for which we set $\alpha = 2$.

This chapter first, in Section 5.1, presents the scalar-field formulation of the defect and defect formation. We address the code that was used in Section 5.2 and how we design the simulative experiments in Section 5.3. In Section 5.4 we present details about the particular simulations we perform.

5.1 \mathbb{Z}_2 symmetry-break

Assume the boson ϕ is responsible for symmetry break at $a = a_*$, when the energy density of the universe is $\rho = \rho_*$. From Section 3.2.2 we have the symmetron effective potential Eq. (3.17), and the equation of motion for the scalar field $\square\phi = V_{\text{eff},\phi}$ reads

$$-a^{-2}[\ddot{\phi} + 2\mathcal{H}\dot{\phi} - \nabla^2\phi] = \lambda\phi^3 + \mu^2(\nu - 1)\phi, \quad (5.1)$$

where $\nu = \rho/(\mu M)^2$. To solve this highly nonlinear equation we evaluate it in the quasi-static (time derivatives negligible) and spatially asymptotic (spatial gradients ignored) limits separately.

In the rest of the thesis we use the scaled quantities $\chi = \phi/\phi_\infty$, $\phi_\infty = \mu/\sqrt{\lambda}$ and $\chi_\pm = \pm\sqrt{1-\nu}$. Prior to SSB, the scalar field solution is trivial, and so we move on to consider χ from this critical point where the quartic term turns negative and the \mathbb{Z}_2 symmetry is spontaneously broken. In the following, we only address the regime where $\rho < \rho_*$.

¹Rather a naive extrapolation of the thickness interpretation, in Eq. (5.4).

5.1.1 Quasi-static limit

We can solve

$$\nabla^2 \chi \simeq +\mu^2 \cdot a^2 [\chi^2 - \chi_+^2] \chi \quad (5.2)$$

to obtain the solution in the limit where spatial gradient plays a much larger role than time derivatives. For $a = 1$ and $\chi_+ = 1$ the solution is the canonical soliton from Section 3.1.1. We consider the well-established extension [see e.g. 31] for the corresponding defect in an expanding universe in combination with adjusting for varying minima [27], namely

$$\chi_w(a, z) = \chi_+ \tanh\left(\frac{\chi_+ a z}{2L_c}\right), \quad (5.3)$$

where L_c is the symmetron Compton wavelength (Eq. (3.19)). This scale—dynamically L_c/χ_+ —signifies the range of the fields in regions where $\rho < \rho_*$ [30].

Basic properties. Consider the conventional \mathbb{Z}_2 wall from Section 3.1.2. Extrapolated to expanding spacetime, we get

$$\sigma_w = \sigma_\infty (1 - \nu)^{3/2} \quad \text{and} \quad a\delta_w = \delta_\infty (1 - \nu)^{-1/2} \quad (5.4)$$

as expressions for the comoving thickness δ_w and the surface energy density σ_w , where constants σ_∞ and δ_∞ are given in Eq. (3.7).

5.1.2 Asymptotic limit

We let $\pm\check{\chi}$ denote the field values far away from the wall, well inside the positive and negative domains. Here,

$$\ddot{\check{\chi}} + 2\mathcal{H}\dot{\check{\chi}} = -\mu^2 \cdot a^2 [\check{\chi}^2 + \nu - 1] \check{\chi} \quad (5.5)$$

governs the evolution of the field strength. The trivial solution becomes unstable after phase transition onset, and the field may fall into any of the two vacua, depending on the phase of the a priori fluctuations. Without loss of generality, we take a look at one of the minima. The positive minimum, which was zero at PT, goes as $\chi_+ = \sqrt{1 - \nu}$. Now, the rate at which χ_+ moves from its initial value, blows up at the phase transition, but decays rapidly when approaching the limit value. It makes sense to analyse the equation in the (i) non-adiabatic and (ii) adiabatic regimes separately.

The non-adiabatic regime (i) is a short window around PT in which the effective potential changes faster than what the dynamics of the scalar field allow. That is to say, the asymptotic field value $\check{\chi}$ cannot possibly hope to follow the system's actual minima χ_\pm . When the scalar catches up, the effective potential changes slower than the field in what we call the adiabatic regime (ii). What happens is that the field rolls towards the minimum and begins to oscillate around it whilst following its slow drift. The oscillation amplitude is decided by the initial conditions of the field.

We know that oscillations in the scalar field can themselves produce gravitational waves [24]. Ideally we would get rid of them completely to not contaminate the gravitational waves sourced by domain walls alone. In addition, these oscillations will to some extent affect the surface tension and thickness of the domain wall in Eq. (5.4). This will in turn alter the equations for ϵ and h_{ij} from the Nambu–Goto theory, making them analytically unsolvable. So we should avoid large oscillations in the scalar field at great cost. We present the protocol for finding the optimal path the field can take to minimise fifth-force oscillations in Appendix C.

5.2 Dynamic modelling

As test bed for our theory we use the C++-code `gwasevolution` [10]; an extended version of the massively parallelised relativistic N -body code `gevolution` [2]. `latfield2` [15] is used as backend to this. We will describe the code in broad terms, and refer to Adamek et al. [2], Christiansen et al. [10, 12], Daverio et al. [15] for more detailed explanations.

Prelude

The general setup is a three-dimensional box of equal side lengths $L_\#$ in Mpc/h_0 on a lattice of $N_\#^3$ points, giving a spatial resolution of $\Delta_\# = L_\#/N_\#$. A Cartesian coordinate system defines the comoving coordinate $\mathbf{x} = (x, y, z)$ and wave vector $\mathbf{k} = (k_x, k_y, k_z)$. The mapping from lattice coordinates $\mathbf{n} = (\mathbf{i}, \mathbf{j}, \mathbf{k})$ to comoving is $\mathbf{x} = \mathbf{n} \cdot \Delta_\#$, where $\mathbf{i}, \mathbf{j}, \mathbf{k} \in [0, N_\# - 1] \in \mathbb{Z}$. Correspondingly in Fourier space, we have lattice coordinates $\tilde{\mathbf{n}} = (\mathbf{u}, \mathbf{v}, \mathbf{w})$, where $\mathbf{u}, \mathbf{v}, \mathbf{w} \in \pm[0, N_\#/2 - 1]$, and the mapping $\mathbf{k} = \tilde{\mathbf{n}} \cdot k_\#$. Here, $k_\# = 2\pi/L_\#$ is the fundamental frequency. The box's boundaries are *periodic* which means that $\mathbf{n} = \mathbf{n} + \hat{\mathbf{n}}L_\#$. Furthermore, the box is decomposed in rod domains for MPI-parallelisation.

The code automatically outputs scalar quantities like extremal values of χ and q , as well as their box-averaged values. Besides this, we request two-dimensional snapshots of the field in question at every-something time step. The file type for the snapshots are Hierarchical Data Format (HDF5). Saving this data is a computational cost, and requires available memory.

Fast Fourier transforms. We write the discrete Fourier transform (DFT) $\tilde{f}(\tilde{\mathbf{n}})$ of $f(\mathbf{n})$ as

$$f(\mathbf{n}) = \frac{1}{N_\#^3} \sum_{\tilde{\mathbf{n}}} e^{-2\pi i \tilde{\mathbf{n}} \mathbf{n} / N_\#} \tilde{f}(\tilde{\mathbf{n}}), \quad \tilde{f}(\tilde{\mathbf{n}}) = \sum_{\mathbf{n}} e^{+2\pi i \tilde{\mathbf{n}} \mathbf{n} / N_\#} f(\mathbf{n}). \quad (5.6)$$

The equations are solved using fast Fourier transforms (FFTs), taken care of by the `latfield2` library [15]. Hermitian symmetry gives

$$\tilde{f}(-\tilde{\mathbf{n}}) = \tilde{f}^*(\tilde{\mathbf{n}}), \quad (5.7)$$

where \tilde{f}^* is the complex conjugate.

Units and conventions. The code measures length in units of $L_\#$ and the DFT sign convention is opposite of Eq. (5.6) *and* without normalisation. We need to adjust for this when comparing results to calculations, e.g. $\tilde{f}|_{\text{calc.}} \leftrightarrow \tilde{f}^*|_{\text{code}}$.

5.2.1 Equations

Perturbations to the FLRW background are evolved in accordance with the linearised Einstein equation.² The tensorial part obeys

$$\ddot{h}_{ij} + 2\mathcal{H}\dot{h}_{ij} + k^2 h_{ij} = 2M_{\text{Pl}}^{-2} \tilde{\Pi}_{ij}^{\text{TT}} \quad (5.8)$$

as elaborated in Section 2.4.1. The asymmetron field is evolved in the Einstein frame with the equation

$$\dot{q} = \nabla^2 \chi - a^2 \mu^2 \{ \chi^3 - 2\bar{\kappa} \chi^2 + (\nu - 1) \chi \}, \quad (5.9)$$

where $q \equiv a^2 \dot{\chi} = a^2 d\chi/d\tau$ is the “speed” of the field. As before (Section 3.2.2), μ and $\bar{\kappa} = \kappa/(2\mu\sqrt{\lambda})$ encode the asymmetron parameters.

²For details, see Adamek et al. [2].

`gwasevolution` solves discretised versions of these via a numerical-integration protocol chosen by the user. The fourth-order Runge-Kutta scheme and Leap-frog method are amongst the options. The size of the time step $\Delta\tau^{(\psi)}$ for the solver of the field ψ is given in terms of the Courant factor [12]

$$C_f^{(\psi)} = v_g^{(\psi)} \frac{\Delta\tau^{(\psi)}}{\Delta\#}, \quad (5.10)$$

where $v_g^{(\psi)}$ is the group velocity of said field. ψ here represents CDM or ϕ , and we use $v_g^{(\text{cdm})} \sim 0.02$ and $v_g^{(\phi)} = 1$. 「Maybe just skip this...」

5.3 TITLE (Toy model design)

To accurately compare the soliton's evolution with the Nambu–Goto prediction, it is essential to begin with an initial configuration closely approximating the exact solution to the equations of the full field theory. Without this, any deviations from the Nambu–Goto dynamics might simply result from inaccuracies in the initial setup.

Revise calculation, I forgot it...

That said, we do not actually have these exact solutions in curved spacetime \star . However, with sufficient tweaking, we should be able to design our desired scenario in a `gevolution` simulation box. This section elaborates on the detailed simulation configuration that is the toy model.

5.3.1 Initial configuration

The purpose of the simulations is to test the applicability of the thin-wall approximation for the wall evolution (Eq. (4.41)) and the corresponding gravitational waves (Section 4.4). Therefore, the simulation setup imitates a toy model, not a realistic scenario. To create this idealised cosmological scenario we initialise the simulation box as described below.

We assume wall profiles of the form

$$\chi_w(a_i, z - z_w) = \check{\chi} \tanh\left(\frac{a\check{\chi}}{2L_c}(z - z_w)\right)\bigg|_{a=a_i}, \quad (5.11a)$$

$$q_w(a_i, z - z_w) = a^2 \frac{d\chi_w}{d\tau}\bigg|_{a=a_i}, \quad (5.11b)$$

where a , $\check{\chi}$ and z_w generally depends on time, and z_w also on spatial coordinates x and y . Note that with $\check{\chi} = \chi_+$ we get the familiar quasi-static formula in Eq. (5.3). We refer to Appendix C for details.

In an FLRW universe a (semi-)stable symmetron domain wall is approximated Eq. (5.3) (or Eq. (C.8)). To preserve periodic boundary conditions, there needs to be an even number of walls present, where half are walls and the other half are anti-walls.³ We choose two, and place the wall of interest at $z_0 = L_\# / 2$, and its counterpart at $\bar{z}_0 = 0$, both aligned with the xy -plane.

Now say we add a displacement $\epsilon = \epsilon(\tau, x, y)$ to the middle wall. Assuming sufficient spatial separation, the system of defects is given by (see Eq. (3.4))

$$\chi(a, \mathbf{x}) = \check{\chi}^{1-2N} \prod_{n=-\infty}^{\infty} \chi_w(a, z - z_w^n) \prod_{m=-\infty}^{\infty} \bar{\chi}_w(a, z - \bar{z}_w^m), \quad (5.12)$$

where

$$z_w^n = z_0 + \epsilon + nL_\# \quad \text{and} \quad \bar{z}_w^m = \bar{z}_0 + mL_\#. \quad (5.13)$$

³Made-up term used as the domain-wall analogue of the antikink in Section 3.1.1.

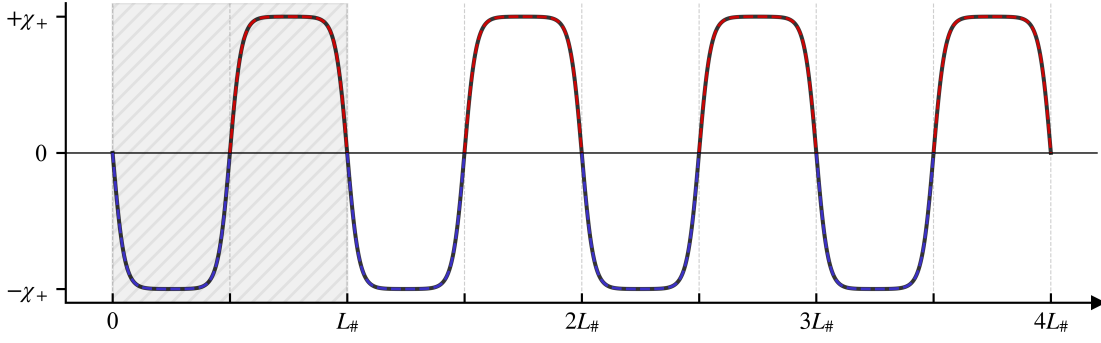


Figure 5.1: Demonstration of the periodicity of $\chi(a_i, z)$ on the lattice. The shaded region represents the box coordinates.

Figure 5.1 demonstrates how $\chi(a_i, z)$ varies with comoving coordinate z , in the absence of wall perturbation.

Setting the initial conditions on the field $q = a^2 \dot{\chi}$ is a matter of algebra. The expression is cleanest when $\dot{z}_w = \dot{\epsilon} = 0$, i.e. for $a_i = a_*$. See Appendix C.2 for detailed explanation.

Initial time. We need to be careful when choosing the exact redshift to initiate the simulation. Clearly, the conventional expression Eq. (5.3) does not work if we set initial redshift $z_i = z_*$. Initiating only a few time steps later allows us to use this after all, but we need to make sure the wall and anti-wall do not collide. Whether this is the case depends on several parameters. Some sets of initial conditions will induce large fifth-force oscillations, and we should try to avoid this.

Using the tweaked initial conditions on the asymptotic fields as boundary conditions on the quasi-static field in Eq. (C.8) opens for the possibility of initialising as close to phase transition as we want. We observe that $\chi^{\text{ideal}} \rightarrow \chi_+$ after some time, and so another strategy to reduce oscillations is to initialise *after* this non-adiabatic phase. The drawbacks are that we might lose important information about the source of the gravitational waves and that $\dot{z}_w \neq 0$.

5.3.2 Energy and momentum

With this exact setup, we can write the total domain-wall SE tensor on the form $T_{\mu\nu} = \sum_n W_{\mu\nu}^n + \sum_m \bar{W}_{\mu\nu}^m$, i.e. as a sum over the SE tensors associated with each wall and anti-wall. Explicitly,

$$\begin{aligned} T_{ab}(\tau, \mathbf{x}) &= -a\sigma\eta_{ab} \sum_n [\Phi_l(z - z_w^n) + \Phi_l(z - \bar{z}_w^n)], \\ T_{iz}(\tau, \mathbf{x}) &= -a\sigma \sum_n [\Phi_l(z - z_w^n) \partial_i z_w^n + \Phi_l(z - \bar{z}_w^n) \partial_i \bar{z}_w^n], \end{aligned} \quad (5.14)$$

from Section 4.4.2, with z_w^n and \bar{z}_w^n are given in Eq. (5.13). Here, σ and $\delta = \sqrt{2}l$ refers to the surface tension and thickness of any wall in the system.

Continuous and discrete Fourier space

The Fourier analogue reads

$$\begin{aligned} \tilde{T}_{ab}(\tau, \mathbf{k}) &= -a\sigma\eta_{ab} \sum_n \left[\mathcal{D}^n(\tau, k_z) \int d^2x e^{ik_z \epsilon} e^{i(k_x x + k_y y)} + (2\pi)^2 \bar{\mathcal{D}}^n(\tau, k_z) \delta(k_x) \delta(k_y) \right], \\ \tilde{T}_{iz}(\tau, \mathbf{k}) &= -a\sigma \sum_n \mathcal{D}^n(\tau, k_z) \int d^2x \epsilon_{,i} e^{ik_z \epsilon} e^{i(k_x x + k_y y)}, \end{aligned} \quad (5.15)$$

where $\mathcal{D}^n = e^{ik_z L_{\#}/2} \cdot \overline{\mathcal{D}}^n$ and $\overline{\mathcal{D}}^n = \exp\{ik_z n L_{\#} - k_z^2 l^2/2\}$ from Section 4.4.2. This essentially gives a periodicity in k_z in the SE tensor that goes as $n \cdot k_{\#}$. We define

$$D(\tau, \mathbf{w}) \equiv \sum_n \delta(\mathbf{w} - n) \mathcal{D}^n(\tau, \mathbf{w} k_{\#}) = \llbracket \mathbf{w} \in \mathbb{Z} \rrbracket (-1)^{\mathbf{w}} \exp\{-\mathbf{w}^2 [k_{\#} \delta(\tau)]^2/4\} \in \mathbb{R}, \quad (5.16)$$

which gives

$$\tilde{T}_{ab} = -a\sigma\eta_{ab} D \cdot \mathcal{F}_{k_x, k_y} \{e^{ik_z \epsilon}\}, \quad \tilde{T}_{iz} = -a\sigma D \cdot \mathcal{F}_{k_x, k_y} \{\epsilon_i e^{ik_z \epsilon}\}, \quad (5.17)$$

as expressions for the walls' displacement field's contribution to the total energy and momentum.

Ref. to some sec.! We used the shorthand notation \mathcal{F}_{k_i} for Fourier transforms \star .

We now get the same result as in Section 4.4.2 in letting $\epsilon = \varepsilon(\tau) \sin py$ and considering $k_y \neq 0$. Substituting $\mathcal{D}_w \rightarrow D$ in Eq. (4.52), we get the TT-projected SE tensor for the whole system, and put into Eq. (4.43) gives the gravitational waves sourced by the displacement in the wall normal coordinate. We elaborate on this for $\alpha = 2$ in the coming subsection.

5.3.3 Ripples in matter-dominated spacetime

Consider matter-domination, $\alpha = 2$, and set $\epsilon = \varepsilon(\tau) \sin py$. The resulting transverse, traceless tensor perturbations are given by $\tilde{h}_{ij} = \tilde{h}_+ e_{ij}^+ + \tilde{h}_\times e_{ij}^\times$. From Section 4.4.2 we have $\tilde{h}_\times = 0$, so the gravitational waves are monochromatic plus-polarised waves given by

$$a(\tau) \tilde{h}_+(\tau, \mathbf{k}) = H_+^1(\tau, \mathbf{k}) + H_+^2(\tau, \mathbf{k}), \quad (5.18a)$$

where

$$\begin{aligned} H_+^1(\tau, \mathbf{k}) &= +S_1(k\tau) \int_{\tau_*}^{\tau} d\hat{\tau} C_1(k\hat{\tau}) f_+(\hat{\tau}, \mathbf{k}), \\ H_+^2(\tau, \mathbf{k}) &= -C_1(k\tau) \int_{\tau_*}^{\tau} d\hat{\tau} S_1(k\hat{\tau}) f_+(\hat{\tau}, \mathbf{k}), \end{aligned} \quad (5.18b)$$

and

$$f_+(\tau, \mathbf{k}) = \frac{16\pi G_N a^3(\tau) \tilde{\pi}_+(\tau, \mathbf{k})}{k^2}. \quad (5.18c)$$

Now consider the TT-projected SE tensor associated with an infinitely thin wall located the origin. We use Eq. (4.52) to write

$$a(\tau) \tilde{\pi}_+^{w0}(\tau, \ell, \vartheta) = 2\pi^2 \sigma_w(\tau) \cos^2 \vartheta \cdot (-1)^\ell J_\ell[\ell \tan \vartheta \cdot p\varepsilon(\tau)], \quad (5.19a)$$

where $\ell = k_y/p \in \mathbb{Z}$ and $\vartheta = \arctan k_z/k_y \in [0, 2\pi)$. We make further use of this parametrisation and write the periodic system's total TT-projected SE tensor as

$$\tilde{\pi}_+(\tau, \mathbf{k}) = \delta(k_x) \delta(k_y - \ell p) \llbracket \ell \in \mathbb{Z} \rrbracket \times \tilde{\pi}_+(\tau, \ell, \vartheta = \arctan k_z/k_y), \quad (5.19b)$$

where

$$\tilde{\pi}_+(\tau, \ell) = D(\tau, \ell \tan \vartheta p/k_{\#}) \times \tilde{\pi}_+^{w0}(\tau, \ell), \quad (5.19c)$$

with $\ell \equiv (\ell, \vartheta)$. Now, Eqs. (5.18) to (5.19) gives \tilde{h}_+ for a given input function $\varepsilon(\tau)$.

5.3.4 Code output and interpretation

We use the outputted two-dimensional snapshots of χ at lattice coordinate $i = 4$ (chosen randomly) to track the simulated wall position, considered as the coordinates (y, z) of the minimum value of $|\chi|$ (ignoring the anti-wall). We define ε^ϕ as the aforementioned quantity at a y -coordinate for which $\sin py = 1$, subtracting the initial position $z_0 = L_\#/2$. The confidence region of this is then $\pm\Delta_\#/2$ in the z -direction. IF TIME: COMMENT ABOUT TEMPORAL RESOLUTION.

The code outputs two-dimensional snapshots of tensor perturbations \tilde{h}_{ij} at the same rate, sliced at $u = 0$. We use only $\tilde{h}_{xx} = \tilde{h}_+$, but sporadically check that $2\tilde{h}_+^2 = \tilde{h}^{ij}\tilde{h}_{ij}$.

The formula for the gravitational waves in the thin-wall limit, Eq. (5.18), allows for any function $\varepsilon(\tau)$ as input. Therefore, we will use both the solution to the equation of motion Eq. (4.33), call it ε^{NG} , and the simulated result ε^ϕ . We will have to keep in mind that the latter is poorly resolved.

The semi-analytical solution \tilde{h}_+ is obtained by means of the simple trapezoidal scheme, specifically the *Numpy* library's `cumptrapz` method ★. We let \tilde{h}_+^{NG} and \tilde{h}_+^ϕ signify the solution to Eqs. (5.18) to (5.19) with ε^{NG} and ε^ϕ as input, respectively. More details?

5.4 Simulation setups

Below, we describe the reasoning behind the choice of parameters. As a starting point, we consider the fiducial set of symmetron parameters $a_* = 0.33$, $\xi_* = 3.33 \times 10^{-4}$ and $\beta_* = 1$, following Christiansen [9]. This gives Compton wavelength $L_c \approx 1 \text{ Mpc}/h_0$ and asymptotic wall thickness $\delta_\infty = \sqrt{2}L_c \sim \sqrt{2} \text{ Mpc}/h_0$.

Simulation box

We use a comoving simulation box size that is comparable to the size of the universe—order $\mathcal{O}(\text{Gpc}/h_0)$ —so that $\delta_w \ll L_\#$ and the separation between the walls is $\sim L_\#/2$. If we want to resolve the Compton wavelength, this requires $N_\# \geq L_\#/L_c \gtrsim L [\text{Mpc}/h_0]$. However, since we are modelling the entire formation, conventional walls (Eq. (5.3)) will initially be infinitely thick and therefore interact with each other.

We will provide the time step sizes in terms of a Courant factor $C_f = \Delta_\tau/\Delta_\#$ for the external loop and a number $N_\phi = \Delta_\tau/\Delta_\tau^{(\phi)}$ that sets the number of times the asymmetron field solver is used per cycle. 「Bad explanation...」

Initial configuration

The normal quasi-static tanh-profile (Eq. (5.3)) approximates the initial configuration to $\check{\chi}_* \rightarrow 0$ and $\check{\chi}'_* \rightarrow \infty$, which does not actually work out. Since $\mathfrak{z}_* = 1/a_* - 1 = 2 + 1/33 > 2$, choosing initial redshift $\mathfrak{z}_i = 2$ leaves wiggle room enough to get simulations started with spatially separated walls.

On the other hand, with the analysis in Section 5.1.2 we can impose suitable initial conditions so that the field rolls into the minima in the most effective way. We need to keep in mind that this affects the surface tension and wall width.

Symmetron parameters

The code uses phenomenological parameters (a_*, ξ_*, β_*) to define the symmetron model. The mapping to Lagrangian parameters (μ, M, λ) is [10]:

$$a_* = \left(\frac{\rho_{\text{cr}0} \Omega_{\text{m}0}}{\mu^2 M^2} \right)^{1/3}, \quad (5.20a)$$

$$\xi_* = \frac{H_0}{\sqrt{2}\mu}, \quad (5.20b)$$

$$\beta_* = \frac{M_{\text{Pl}}}{M^2} \frac{\mu}{\sqrt{\lambda}}. \quad (5.20c)$$

a_* is the cosmic scale factor at symmetry break, as before, $\xi_* = H_0 L_C$ is the Compton wavelength per Hubble length, and β_* measures the strength of the fifth force (see Eq. (3.13)). For $\kappa > 0$, the parameter β_* is modified s.t. $\beta_* \rightarrow \bar{\beta} = (\beta_+ + \beta_-)/2$. Formal definitions are found in Christiansen et al. [10].

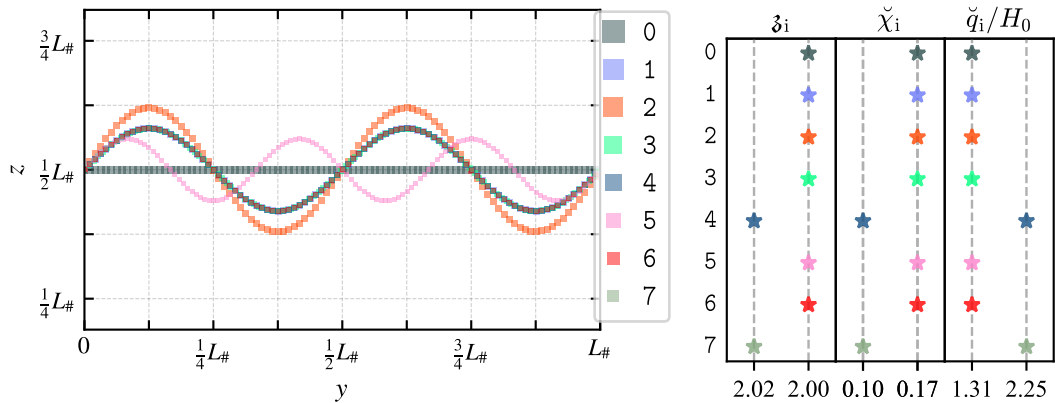
Nature of wall perturbation

We choose to only perturb one wall so that the time of collision between propagating gravitational waves is at $\tau_i + L_\# / 2$ \star .⁴ We would like $\varepsilon_* \ll L_\# / 2$, but with a quick look at Fig. 4.1 we can assume that this would require a very high spatial resolution. As a result, we choose to exaggerate the initial perturbation amplitude and risk higher-order effects. \star

Is this true? Maybe col.
time is double?
Maybe give a length scale?

5.4.1 Catalogue

We present results in Chapter 6 from the eight simulations that are listed in Table 5.1, with supplementary visualisation in Fig. 5.2. We largely use Christiansen et al. [12] to help make parameter choices. Every simulation—labelled 0, 1, ..., 7—uses a 4th order Runge-Kutta solver. We use simulation 1 as a starting point and change one or two parameters at a time for subsequent experiments. The middle wall is unperturbed in simulation 0, and this particular experiment works as a sort of benchmark to separate the wall displacement effect. Each simulation is associated with a characteristic colour (see Table 5.1) that will distinguish it in figures to come.



(a) Schematic of the initial wall position in the yz -plane for each simulation. Note that 1, 3, 4 and 7 are overlapping. (b) Initial redshift, and asymptotic scalar and velocity field values.

Figure 5.2: Visual representation of initial configurations listed in Table 5.1.

⁴Perturbing both walls would give collision time $\tau_i + L_\# / 4$.









Wall–anti-wall simulations								
	0	1	2	3	4	5	6	7
								
<i>Symmetron parameters</i>								
a_*	0.33	0.33	0.33	0.33	0.33	0.33	0.33	0.33
$\xi_* \times 10^4$	3.33	3.33	3.33	3.33	3.33	3.33	1.00	3.33
β_*	1	1	1	1	1	1	1	1
<i>Perturbation parameters ($\varepsilon_* \sin(p_y y)$)</i>								
$\varepsilon_*/L_\#$	0.00	0.08	0.12	0.08	0.08	0.06	0.08	0.08
$p_y/k_\#$	–	2	2	2	2	3	2	2
Υ_*	0	16	24	16	16	18	16	16
<i>Simulation box</i>								
$L_\# [\text{Mpc}/h_0]$	1024	1024	1024	1024	1400	1024	1024	1024
$N_\#$	768	768	768	900	768	900	768	768
$\Delta_\# [\text{Mpc}/h_0]$								
<i>Initial configuration</i>								
\mathfrak{z}_i	2.00	2.00	2.00	2.00	2.02	2.00	2.00	2.02
\mathfrak{z}_f	1.00	1.00	1.00	1.00	1.00	1.00	1.00	1.00
$\check{\chi}_i$	–	–	–	–	–	–	–	–
\check{q}_i	–	–	–	–	–	–	–	–
<i>Numerics</i>								
C_f	0.2	0.2	0.2	0.2	0.2	0.2	0.2	0.2
N_ϕ	4	4	4	4	4	4	4	4

Table 5.1: Details about each simulation addressed in Part III. Each simulation is labelled 0–7. See Sections 5.3 and 5.4 for description of parameters.

An additional, completely homogeneous simulation (no walls present) is run with the same background as simulation 1, except that the symmetron initial conditions are optimised as described Appendix C with $\mathfrak{z}_i = 2.03$.

Part III

Findings

Chapter 6

TITLE (Toy Model Trials)

This chapter provides simulative insights to our theoretical framework. We both present and discuss results from the simulations described in Table 5.1, and compare these to the theory. The analysis is split into three parts: In Section 6.1 we study the background evolution through box-averaged scalar quantities. Less primitive analysis proceeds in Section 6.2 where the domain wall dynamics of the two theories is compared. Finally, in Section 6.3 we look at what sort of gravitational waves we expect from this phenomenon.

We include in Section 6.4 some afterthoughts and comments about the simulations. 「Not sure where it is best placed.」

Simulation 6 is considered unsuccessful as it blows up at around $a \approx 0.45$. Where this is considered in the analysis, the results are shown for only $a \in [a_i, 0.46]$.

6.1 Symmetron field

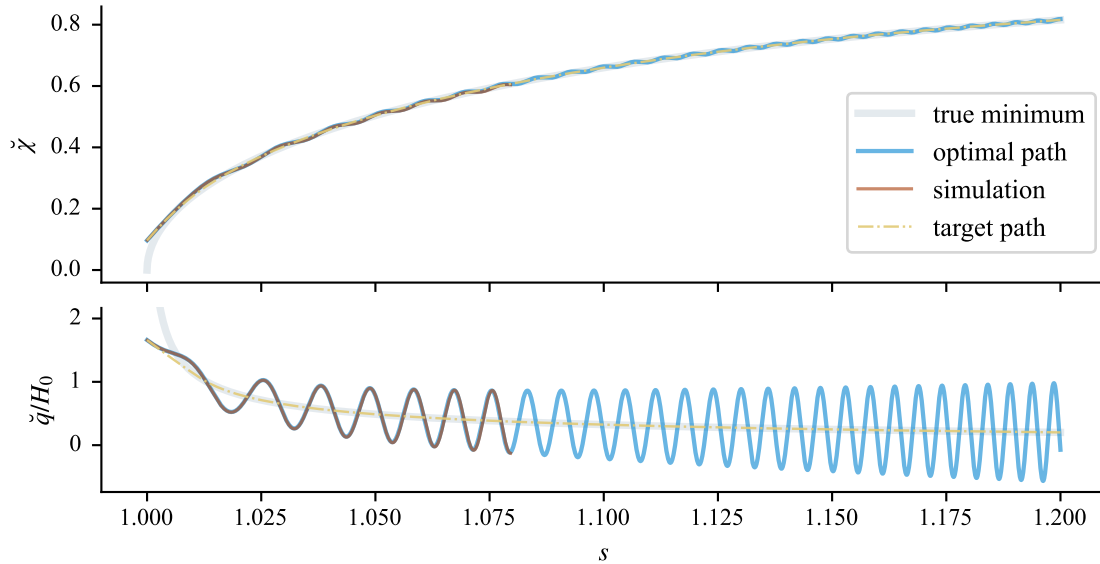


Figure 6.1: The evolution of the symmetron field in the asymptotic limit. The symmetron parameters are the fiducial ones. The simulation results are from the simulation with no walls. We see χ_+ in solid grey, $\tilde{\chi}|_{\text{opt.}}$ in solid blue, $\langle \tilde{\chi} \rangle$ in solid red and $\tilde{\chi}^{\text{ideal}}$ in dashed yellow.

In the simplest case where there are no walls present, and the scalar field takes the same value everywhere, the evolution is described solely by Eq. (5.5). In this case, we expect there to

be good correspondence between theory and simulation. We find that the optimal path for the symmetron to minimise oscillations occurs if initial conditions are given by Eq. (C.7). This result is demonstrated in Fig. 6.1. We distinguish between the idealised path—call it χ^{ideal} —given by Eq. (C.7), and the “optimal” path that solves Eq. (5.5) with initial conditions $\chi|_{a_i} = \chi^{\text{ideal}}|_{a_i}$ (and likewise with derivatives), that differ slightly for different choices of a_i .

With that established, we move on to wall–anti-wall simulations as described in Section 5.3 and Table 5.1. The symmetron field χ will at SSB roll into either minima, depending on the sign of the field right before it happens. The strength of the oscillations around the true minima depend on both the initial field value and its time derivative. We show in Fig. 6.2 a handful of background quantities from various simulations. The simulations with earlier initialisation

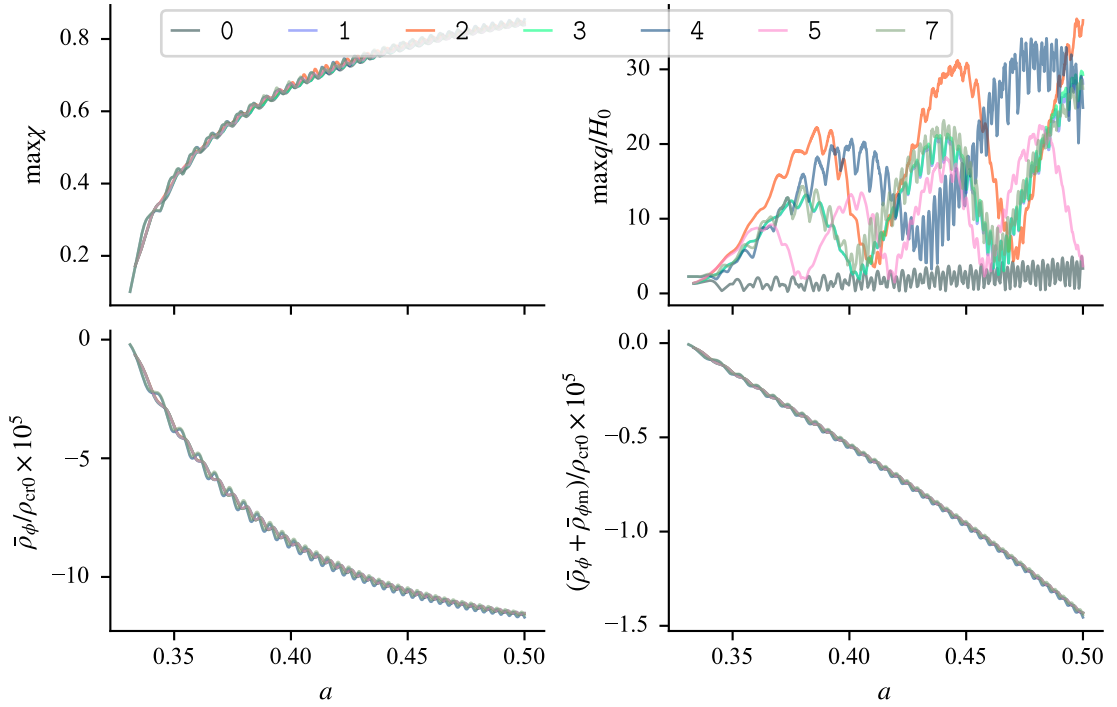
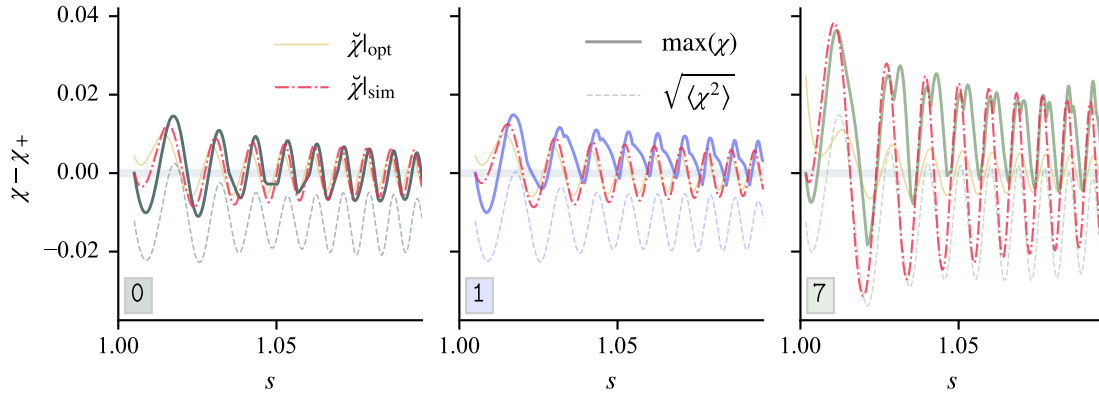


Figure 6.2: Background quantities. 「Not too happy about this plot... FIX LABELS!」

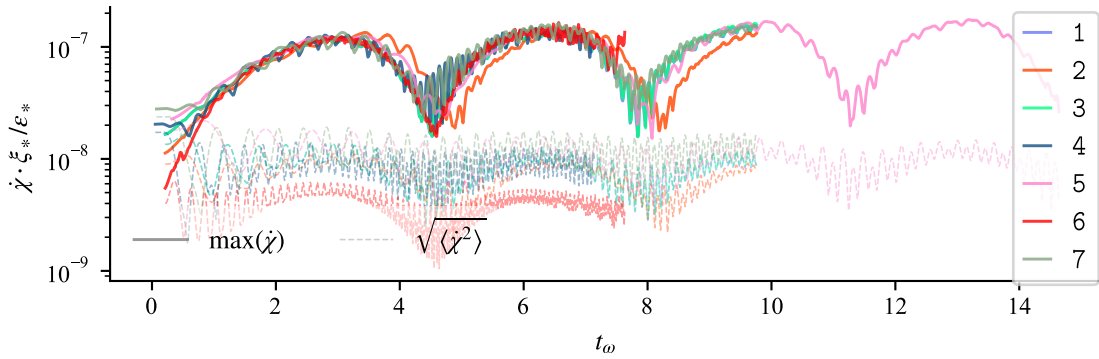
(simulations 4 & 7) do give enhanced fifth-force oscillations. This is consistent with numerical solutions to the asymptotic equations with similar initial conditions. We take a closer look at the symmetron field in Fig. 6.3.

Symmetron field. Figure 6.3a shows two things. First, the asymptotic evolution of the symmetron field from simulations correspond to numerical solutions to Eq. (5.5) with equal initial conditions. We come to this conclusion by combining the maximum value of χ and the smoothness of the averaged χ^2 . Second, the best possible path is very close to the actual evolution in simulations initialised at redshift 2.00, which makes re-runs less useful. On the other hand, we see that simulation 7 (and 4) is expected to benefit quite a lot from such a tweaking of initial conditions.

Velocity field. It turned out to be very convenient to plot certain quantities over the peculiar time parameter $t = \omega(s - 1) = p(\tau - \tau_*)$. One of the quantities that inhabits such a nature is the asymptotic velocity field \tilde{q} , or in actuality the maximum of q . The similarities in Fig. 6.3b are not difficult to spot. We plot the field as $q [a^2 \varepsilon_* / \xi_*]$ to emphasise how the speed scales as the



(a) Yellow solid and red dash-dotted graphs show results from numerically solving the asymptotic Eq. (5.5) with optimal (Eq. (C.7)) and simulation (Table 5.1) initial conditions, respectively. The solid and dashed lines show respective simulation output, in form of maximum and averaged values. All are functions of conformal time $s = \tau/\tau_*$.



(b) The graphs show the outputted maximum (solid) and averaged (dashed) values of q in units $a^2 \varepsilon_* \xi_*^{-1}$, all as functions of $t_\omega = p(\tau - \tau_*)$.

Figure 6.3: The asymptotic symmetron field $\check{\chi}$ and its time derivative $\check{\chi}$.

initial perturbation amplitude (and symmetron length scale). We can look at Fig. 6.2 to see that this is a feature of the perturbation, as simulation 0 lacks said feature. The next section will show how this periodicity is strongly connected to the wall position. The average absolute value tells us more about the fields' stability, where we see a link between these lines' and the asymptotic scalar field's strength of oscillations around minima.

6.1.1 Holistic review

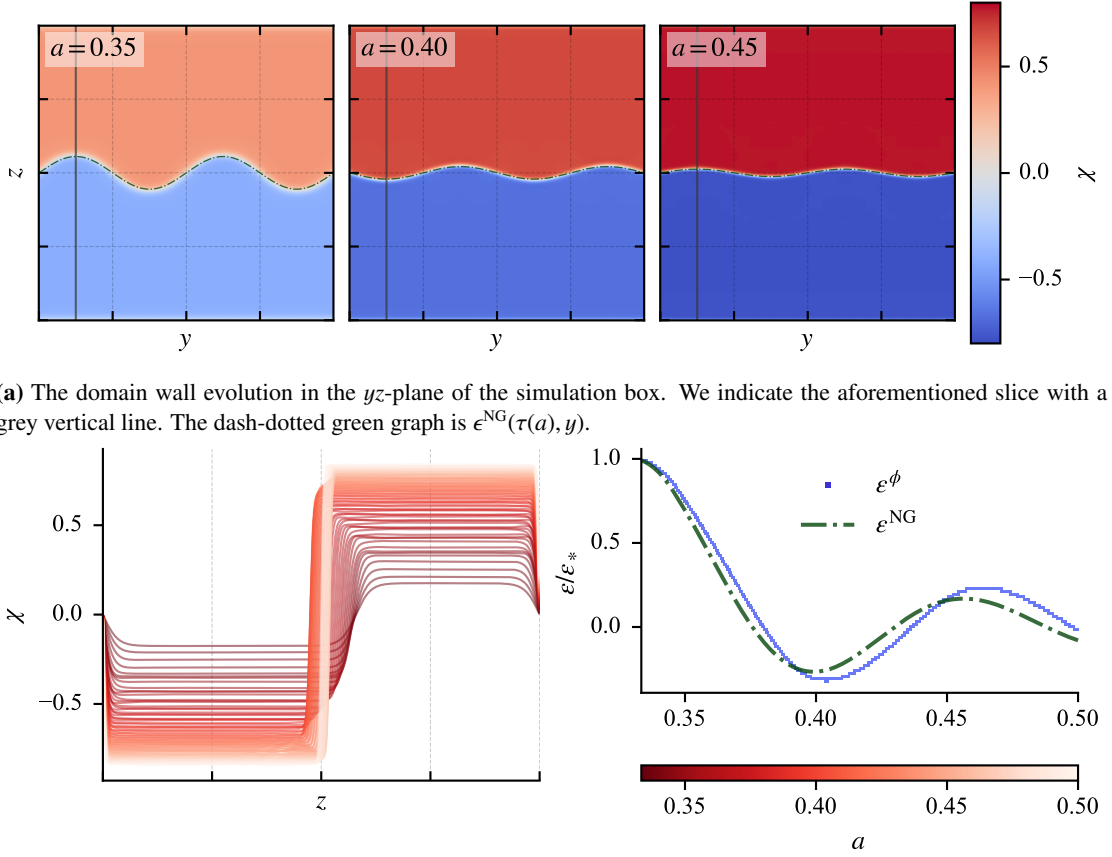
In the absence of topological defects, we see near on perfect correspondence between predicted and simulated scalar field $\chi = \check{\chi}$ (Fig. 6.1). Presence of walls messes with the maximum field value (Fig. 6.2), due to the “bump” in the profile, a feature that is much more prominent when the walls are perturbed (cf. two left-most panels in Fig. 6.3a). In any case, we see from the average squared field value that the overall oscillations are very close to what we expect. The path the field can take that inhabits the smallest possible fifth-force oscillations is close to what happens in simulations 0–3 and 5. The same cannot be said for simulations 4 and 7.

6.2 Domain wall dynamics

Ignore the anti-wall at the box's boundaries. Simulation-wise, the wall's position is tracked by the minimum value of $|\chi|$, i.e. the z -coordinate at which the field is closest to zero. We

keep in mind that we do not expect a perfect match between the simulated and analytical wall perturbation, partly because the analytical equations are only valid for perturbations of leading order, but also because the thin-wall limit is expected to fail at the early stages of the phase transition. A more tangible way to look at it is to consider the unperturbed unit normal vector that we put along the z -axis; just by looking at the simulations (Fig. 6.4a), we can see that this is clearly not the case, at least close to phase transition.

We reduce the problem from three dimensions to two, and then again to one dimension by considering a suitable slice in the y -direction (where $\sin py = 1$) at which we take the z -coordinate of the minimal absolute value of the scalar field χ . An example of the two-dimensional perspective is shown in Fig. 6.4a. This picture is more or less the same for all simulations, at least when comparing by-eye.



(a) The domain wall evolution in the yz -plane of the simulation box. We indicate the aforementioned slice with a grey vertical line. The dash-dotted green graph is $\epsilon^{\text{NG}}(\tau(a), y)$.

(b) *Left panel:* The scalar field value along y -coordinate $y = 96\Delta_{\#}$ at different redshifts following the colour bar in the right panel. *Right panel:* The wall coordinate as function of time.

Figure 6.4: Demonstration of the interpretation of the results from simulation 1.

We observe a “bump” in the quasi-static tanh-solution in each simulation, manifesting in plots like the left panel of Fig. 6.4b around $z \sim z_0, \bar{z}_0$, and in the maximum value of χ in Fig. 6.3a. This effect is seemingly more prominent in simulations with $\epsilon_* > 0$, i.e. everyone except \emptyset .

The simulated wall position graph is not perfectly overlapping with the analytical one, as the right panel of Fig. 6.4b shows. Simulated walls show a tendency to evolve slower, at least initially, realised in a phase difference between ϵ^{ϕ} from simulation and ϵ^{NG} from the thin-wall approximation.

In Fig. 6.5 we show the difference between the Nambu–Goto prediction—which for $e = \epsilon/\epsilon_*$ vs. $t_{\omega} = \omega(s - 1)$ is the same any setup—and the field theory. Simulations with similar

perturbation setup (cf. 1, 2, 4, 7) but different box parameters give similar wall evolution. Note that there is a bump in the simulations with larger scalar field oscillations (4 & 7) \star . Larger initial amplitude (2) increases the difference, as does larger scale parameter (5). The bottom panel of Fig. 6.5 is remarkably alike Fig. 6.3b.

Invisible...

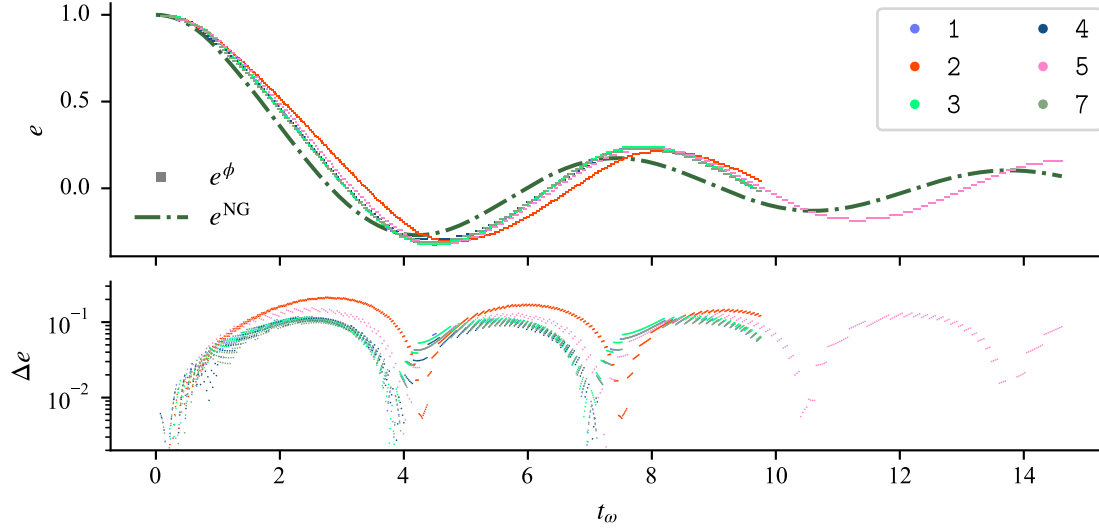


Figure 6.5: Functions of the scaled time parameter $t_\omega = \omega(s - 1) = p(\tau - \tau_*)$. *Top panel:* The wall extremal position normalised to the initial amplitude, $e = \epsilon/\epsilon_*$. *Bottom panel:* The absolute difference between the wall position from calculations and simulations, $\Delta e = |\epsilon^{NG} - \epsilon^\phi|/\epsilon_*$.

We see that initial amplitude actually does matter in simulations, cf. simulation 1 vs. 2. The thin-wall approximation disagrees with this, but it can be argued that this relates to the validity of the linear perturbation size. This points to higher-order effects or resolution issues as candidate explanations for the discrepancy, rather than it being a problem with the damping term in the equation of motion. Otherwise, this can just as easily be a manifestation of the approximation that the Nambu–Goto description actually is \star .

Still bad sentence...

We observe that the initial perturbation amplitudes in simulations 2 and 4 are similar in comoving units, with $\epsilon_* = 0.12L_\# \approx 123 \text{ Mpc}/h_0$ and $\epsilon_* = 0.08L_\# = 112 \text{ Mpc}/h_0$, respectively. The large-box simulation gives results close to those with $\epsilon_* = 0.08L_\#$, whereas simulation 2 shows different wall dynamics. The point is that as far as the linearised-perturbation analysis goes, the order is given relative to the comoving horizon $\tau = \tau_*$. This gives substance to the hypothesis that the discrepancy might be due to interactions with the anti-wall. On the other hand, when factoring in the perturbation scale parameter, we can think of the perturbation in simulation 4 as equal to those of 1, 3, etc. A better upper length scale may then be $\sim L_\#/2$ as opposed to τ_* .

IF TIME! ADD THE FOLLOWING ANALYSIS: “ADJUSTING THE EQUATION OF MOTION”

IF TIME! SHOULD I INCLUDE OLD RESULTS THAT ARE VERY BAD? WHERE $\epsilon_* \sim L/4$.

6.2.1 Holistic review

The full field-theoretical description of the wall evolution agrees with the thin-wall approximation to some level. The general tendency is that the oscillatory behaviour in the Nambu–Goto description is quicker and somewhat weaker than what simulations would have it. Both show characteristics of a damped harmonic oscillator with wavelength $\gtrsim 2\pi/t_\omega$. Upgrading the spatial resolution with about 15%—as done with simulation 1 and 3—does not show significant changes in the evolution of the wall displacement parameter.

Minimising scalar-field oscillations does not seem to affect the wall evolution particularly. This can be seen by comparing simulations 1, 3, 4 and 7 which all have the same relative initial amplitude, but different levels of fifth-force oscillations. However, changing the “curvature” of the wall, seems to change the overall behaviour of the displacement parameter ε . In particular, increasing the parameter Υ_*^\sim from 16 to 18 (simulation 3) or 24 (simulation 5). We use this as a naive quantification of the badness of the equation of motion for ε ; the larger amplitude, the more likely we are to see higher-order effects, and the larger wavenumber, the farther we are from the wall normal coordinate $n^\mu \sim \delta_z^\mu$, roughly speaking \star .

The wall–anti-wall system may inhabit inter-kink forces if the walls are not sufficiently far apart [35], and this could contribute as an external force in the equation of motion for the wall perturbation. Since such forces would be attractive and position-dependent [35], this could explain why ε^ϕ is “slower” and “deeper” than ε^{NG} . There might also be “intra-kink” forces at play, that is interactions between different points on the same wall. The parameter Υ_*^\sim can provide an indication as to the risk of this happening, at least in the y -direction. The walls are not infinitely thin and one can imagine that internal forces may contribute in the z -direction.

It is difficult to see in Fig. 6.5, but we notice that higher levels of scalar field fluctuations (simulations 4 and 7) correspond to simulations where the wall evolution is *discontinuous* in the very beginning. This is apparently not affecting the motion later. The two simulations in question are also characterised by initialisation closer to SSB, a feature that can technically be source of *both* of these phenomena.

We have *not* thoroughly tested whether $\varepsilon^\phi(\tau, x, y) = \varepsilon^\phi(\tau) \sin py$ is a good fit. From Fig. 6.4a, and similar results, we can see that the sine profile seems to be quite well-preserved throughout the evolution.

6.3 Gravitational waves

The gravitational waves from the Nambu–Goto motion are given by a complicated expression. We have not been able to obtain the corresponding expression in configuration space, neither have we found a way to present sensible summary statistics from it.

We list a few key points about the simulated gravitational-wave results in general. The data we get from the code is the averaged squared value of the strain’s conformal time derivative (see below, Eq. (6.1)) at every time step, and the Fourier image of the tensor perturbations for $\tilde{\mathbf{n}} = (0, \mathbf{v}, \mathbf{w})$ at every fourth-or-so time step.

- Zero walls or unperturbed walls (simulation 0) produce no gravitational radiation.
- The predicted periodicity in k_y (that $\tilde{h}_{xx}|_{k_y \neq np} \rightarrow 0$) agrees with simulations.
IF TIME? MAYBE PROVIDE SOME NUMBERS?
- There is decidedly *a* signature of the perturbation in some wave modes. There are characteristics similar to what the thin-wall limit predicts, but the resemblance varies a lot from mode to mode, and also in time.
- Stronger scalar-field fluctuations correspond to noisier gravitational-wave modes.
- Computing the magnitude of the gravitational waves analytically does not agree with corresponding simulative results. IF TIME? SOMEWHERE REPORT AN ESTIMATE OF THE ABSOLUTE DIFFERENCE IN MAGNITUDE?
- The unpredicted *imaginary* parts of the simulated gravitational waves carry much more resemblance to analytically calculated, real ones, than their real counterparts.

6.3.1 Gravitational radiation

We begin by having a look at the energy density of the gravitational waves, which is obtained through the average conformal time derivative of the *real space* tensor perturbations [24],

$$\rho_{\text{gw}} = \frac{1}{32\pi G_N a^2(\tau)} \langle \dot{h}^{ij}(\tau, \mathbf{x}) \dot{h}_{ij}(\tau, \mathbf{x}) \rangle_{\text{box}} = \frac{1}{32\pi G_N a^2(\tau)} \frac{1}{N_{\#}^3} \sum_{ijk} \sum_{ij} [\dot{h}_{ij}(\tau, \mathbf{x}_{i,j,k} \Delta_{\#})]^2. \quad (6.1)$$

We plot this as functions of (scaled) conformal time s and the perturbation time parameter

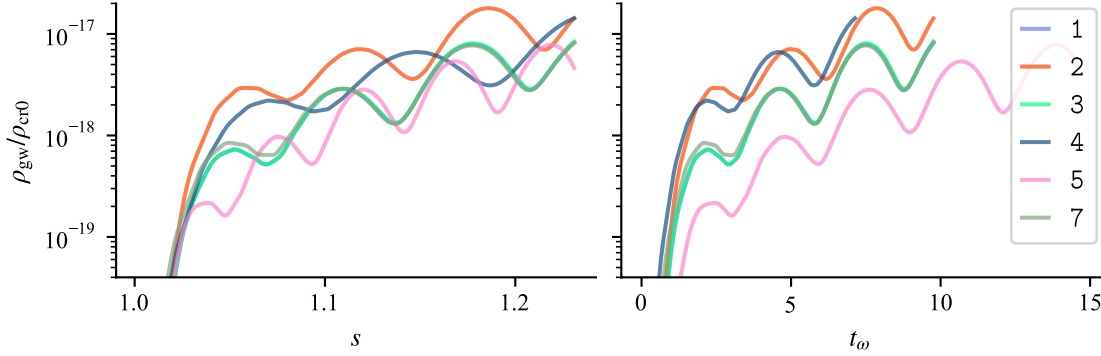


Figure 6.6: The box-averaged gravitational wave radiation, normalised to the critical density today. Note the logarithmic y -axes. *Left panel:* ρ_{gw} as function of $s = \tau/\tau_*$. *Right panel:* ρ_{gw} as function of $t_\omega = \omega(s - 1) = p(\tau - \tau_*)$.

$t_\omega = \omega(s - 1)$ in Fig. 6.6 for a number of simulations. The graphs in the right panel show similar patterns as before, in Fig. 6.3b. The energy is in the range $\log(\rho_{\text{gw}}/\rho_{\text{cr0}}) \sim -18, -17$. In comparison, gravitational radiation from domain wall networks is often approximated as $\rho_{\text{gw}} \sim \sigma^2/(40\pi M_{\text{Pl}}^2)$ [32], which is approximately $\sim 10^{-12}\rho_{\text{cr0}}$ for the symmetron parameters used in every simulation, except for simulation 6.

6.3.2 Comparison with analytical results

We refer to Section 5.3.4 for details about how the data were extracted. Henceforth, \tilde{h}_+ refers to Eq. (5.18), for which inputs ε^{NG} and ε^ϕ give \tilde{h}_+^{NG} and \tilde{h}_+^ϕ , respectively. The output from simulations, the xx -component of the tensor perturbations, is denoted $\tilde{h}_+ = \tilde{h}_+^{\text{R}} + i\tilde{h}_+^{\text{I}}$. We will present our results in terms of scaled wavenumbers that satisfy

$$k_x = 0, \quad k_y = \mathbf{v}k_{\#} = \ell p, \quad k_z = \mathbf{w}k_{\#} = \ell p \tan \vartheta; \quad \ell \in \mathbb{Z}, \quad (6.2)$$

where $\tilde{\mathbf{n}} = (\mathbf{u}, \mathbf{v}, \mathbf{w}) \in \mathbb{Z}^3$ represents the lattice momentum. Note that $\ell = (\ell, \theta)$ and (\mathbf{v}, \mathbf{w}) represent different comoving momenta $(0, k_y, k_z)$ in e.g. simulation 1 and 4. The length of the wave vector is $k = |p \ell \sec \vartheta|$.

The first notable observation is that $\tilde{h}_+ \in \mathbb{R}$, whereas $\tilde{h}_+ \in \mathbb{C}$. In fact, the results consistently show more resemblance between \tilde{h}_+^ϕ and \tilde{h}_+^{I} , than between \tilde{h}_+^ϕ and \tilde{h}_+^{R} . It is clear that the slight offset $\Delta\varepsilon = |\varepsilon^{\text{NG}} - \varepsilon^\phi|$ makes for a significant difference in \tilde{h}_+ .

Figure 6.7 demonstrates this for a number of \mathbf{k} -modes in simulations 1, 3, 7, 2 and 5. The magnitudes are ignored in this analysis. There is a quite remarkable likeness between \tilde{h}_+^ϕ (solid red lines) and \tilde{h}_+^{I} (blue dashed lines). Comparison of Figs. 6.7a to 6.7c suggests that more prominent scalar-field fluctuations disturb the gravitational wave modes a little (blue graphs), and that \tilde{h}_+^ϕ is sensitive to tiny deviations in ε^ϕ (red graphs). The initial size of the perturbation, ε_* , affects the temporal behaviour, as expected, and not just the scale parameter p . This is seen

by comparing Figs. 6.7d and 6.7e to any of Figs. 6.7a to 6.7c. We see from the secondary time axes that the resonance in t_ω -space lives on to some extent, backed by the right panel of Fig. 6.6.

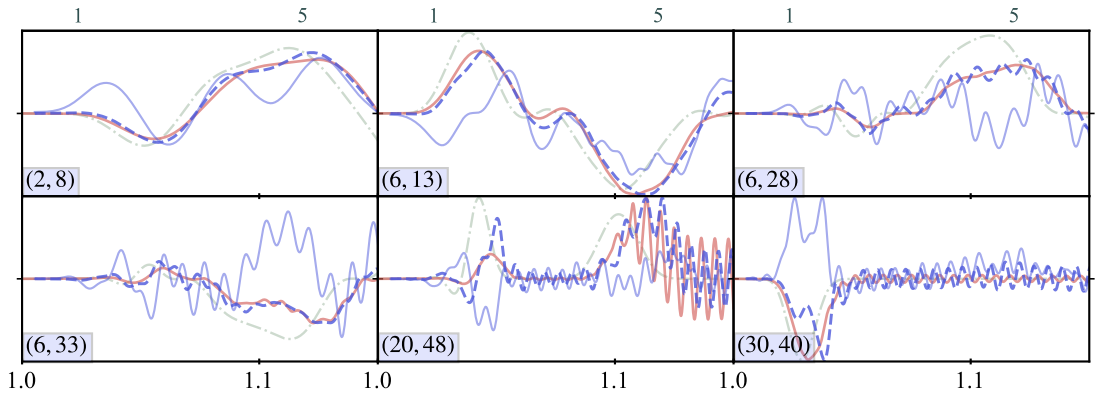
Studying each wave mode's evolution over time does not give as much physical insight as it is time-consuming.¹ Another way to compare the results is through a one-dimensional power spectrum:

$$\delta(k_x)\delta(k_y - \ell p)P_h(\tau, \vartheta; \ell) = h^{ij}(\tau, \mathbf{k})h_{ij}(\tau, \mathbf{k}).^2 \quad (6.3)$$

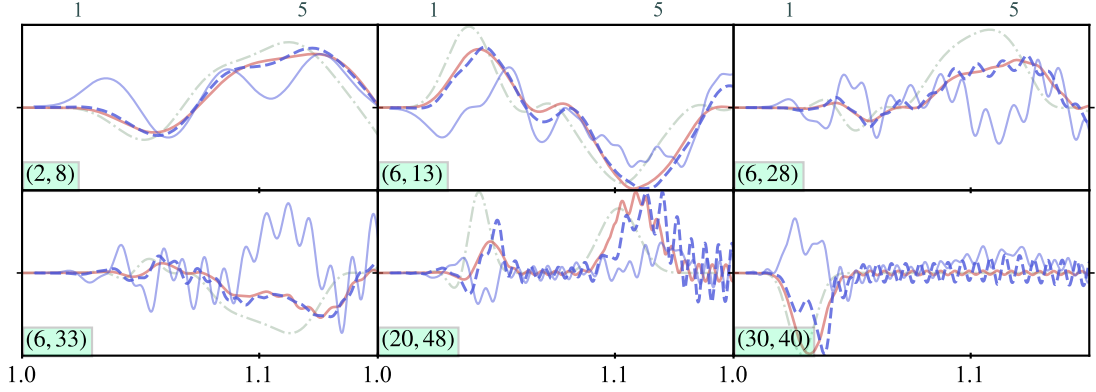
We see from Fig. 6.6 where the intensity of the waves peaks and use this to choose time points for our power-spectrum analysis. It is interesting to compare simulations with different perturbation

¹There are potentially $N_\#^2/2m_j$ different modes for each simulation.

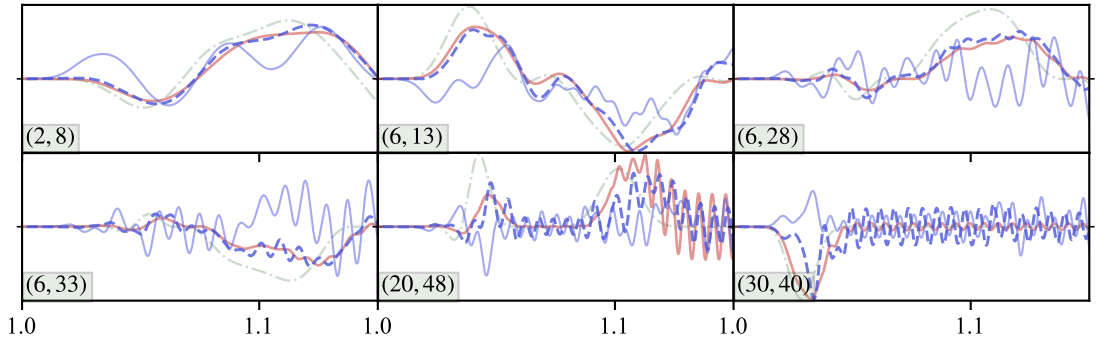
²It would be more conventional to output and analyse \dot{h}_{ij} , but we make the early (arbitrary) unconventional choice.



(a) Simulation 1: $m_j = 2$ and $\varepsilon_* = 0.08L_\#$.



(b) Simulation 3: $m_j = 2$ and $\varepsilon_* = 0.08L_\#$.



(c) Simulation 7: $m_j = 2$ and $\varepsilon_* = 0.08L_\#$.

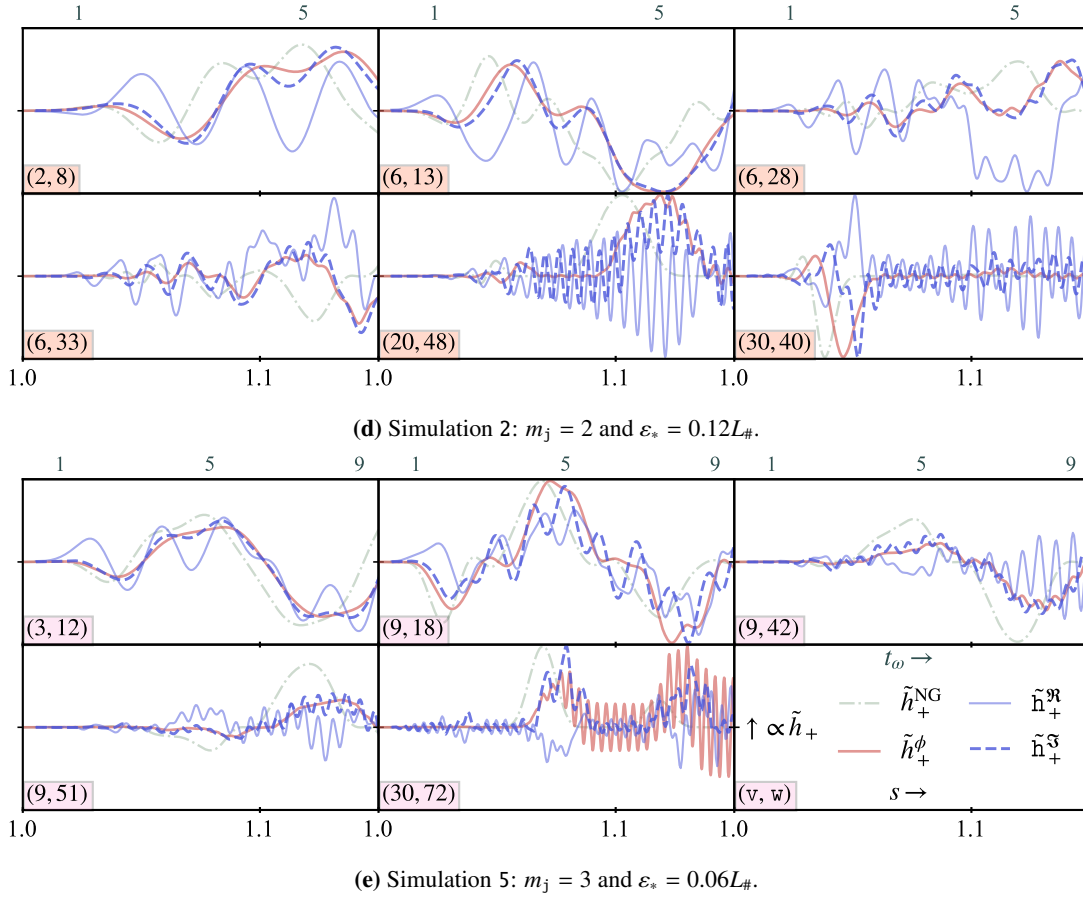


Figure 6.7: Monochromatic plus-waves evolving over conformal time $s = \tau/\tau_*$, normalised to unity. The lower right panel is explanatory for all panels: Green dash-dotted graphs represent \tilde{h}_+^{NG} , orange solid ones represent \tilde{h}_+^ϕ and in blue are \tilde{h}_+ . The wave vector is given in the lower left corner of each plot, as (v, w) . The secondary above x-axis represents scaled time $t_\omega = p(\tau - \tau_*)$.

scale. In Fig. 6.8 we compare the results from the Nambu–Goto theory (Eq. (5.18)) \tilde{h}_+^{NG} and \tilde{h}_+^ϕ , and directly from simulation, \tilde{h}_+ . We stress that the units are arbitrary, and the magnitudes are not reported. Each column represents the same ℓ -mode for different times, whereas each row signifies the same time point but different ℓ 's. The horizontal axes show ϑ , where $\vartheta = 0^\circ$ and $\vartheta \rightarrow 90^\circ$ correspond to $\mathbf{k} = (0, k, 0)$ and $\mathbf{k} \rightarrow (0, 0, k)$, respectively. Note that $\vartheta = 0^\circ$ suggests waves propagating along the domain wall.

The results in Fig. 6.8 show some likeness in the shape and evolution of P_h with \tilde{h}_+^ϕ and \tilde{h}_+ for some values of ℓ . The wave vectors in Fig. 6.8a and Fig. 6.8b are equal, but the time points are different.

6.3.3 Holistic review

Figure 6.7 shows that the perturbation parameters clearly manifest in the gravitational waves. The physical insight of analysing this mode by mode is maybe not too great, but the likeness indicates that there is a pattern to be found, at least. We would have to go further into technicalities regarding the lattice spin-2 operator to conclude anything about what causes $\tilde{h}_+^S \neq 0$. Figure 6.6 agrees that there is a predictable relationship between the wall perturbation in its simplest form ($\varepsilon \sin py$) and gravitational radiation.

There is a large and inconsistent difference in magnitude between \tilde{h}_+^2 and \tilde{h}_+^2 . This thesis

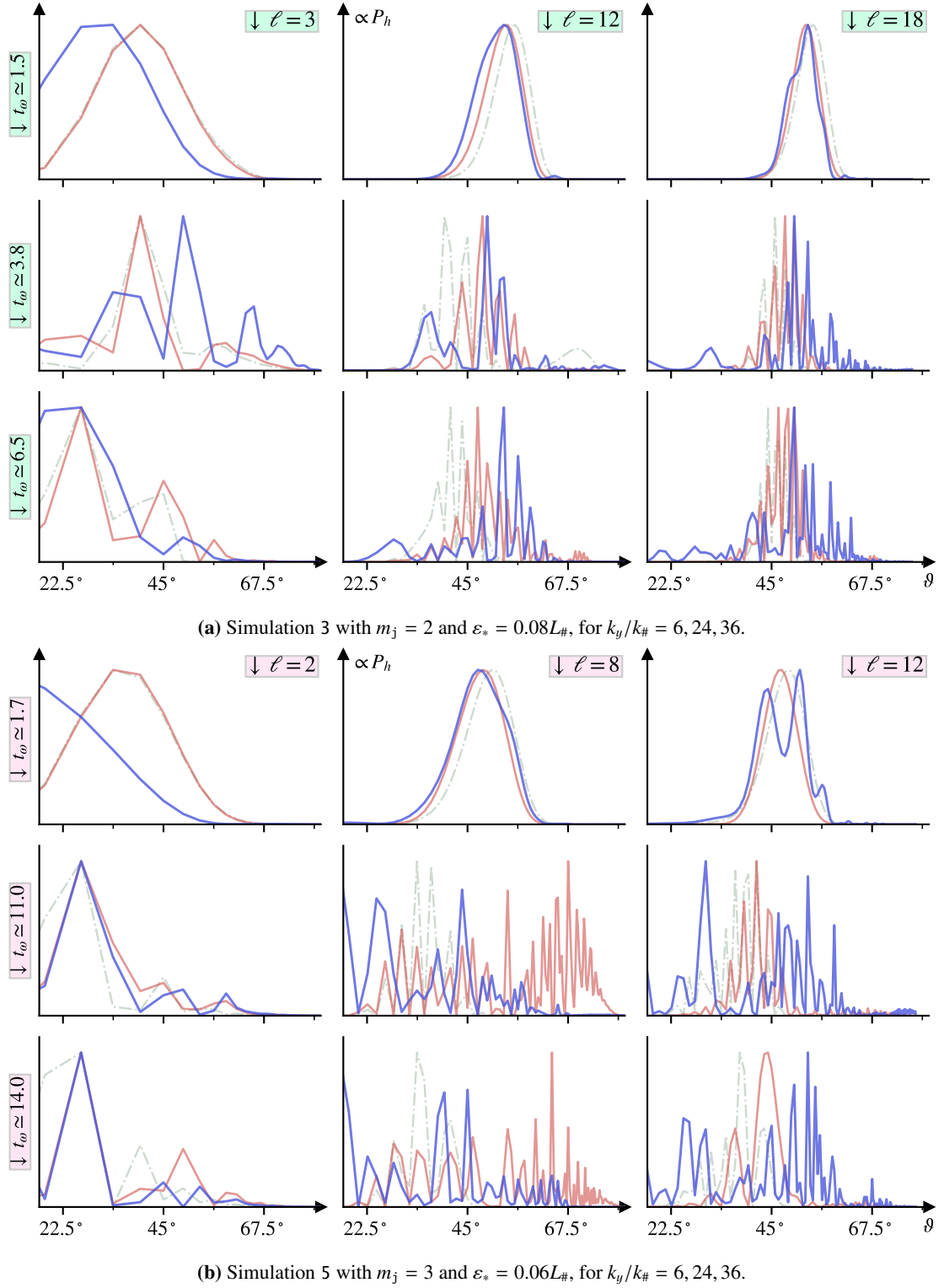


Figure 6.8: The one-dimensional power spectrum as functions of angle ϑ , in arbitrary units. Green dash-dotted graphs represent \tilde{h}_+^{NG} , orange solid ones represent \tilde{h}_+^ϕ and in blue are \tilde{h}_+ .

does not cover this part of the analysis in depth, but we list some issues that are possibly related to this.

- The dimensions of the Fourier-transformed tensor perturbations and SE tensor are

$[k^{-3}] = (\text{length})^3$ and $[k \cdot k^{-3}] = (\text{length})^2$, respectively. There can be a misunderstanding in the unit conversion both from the simulation output and in the computation of $\tilde{\pi}_+$.

IF TIME? COMMENT ABOUT DELTA-FUNCTIONS? A source of confusion may be the transformation from discrete to continuous Fourier transforms.

- The cumulative-trapezoidal scheme that computes \tilde{h}_+ has numerical weaknesses, and the input to \tilde{h}_+^ϕ is originally discrete. Tiny changes in ε can have massive effect for \tilde{h}_+ , and discontinuities often lead to larger values.
- The wall width is defined from convention, and measures scale more than an actual physical observable.

6.4 Hindsight

Some technicalities regarding our choices is necessary to address at this point. ★ Is it OK to suddenly write in past tense...? It seemed natural to begin with a set of parameters that was deemed sensible before, i.e. $a_* = 0.33$, $\xi_* = 3.33 \times 10^{-4}$ and $\beta_* = 1$ from Christiansen et al. [10]. The initial idea was to start simulations at initial redshift $\mathfrak{z}_i = 2.00$ with SSB happening only a few time steps before this, at $\mathfrak{z}_* = 1/a_* - 1 = 2 + 1/33 \simeq 2.0303$. This way, the “true” wall width $\delta_w = (a\mu\chi_+)^{-1}$ is not infinite at the start, and we may use the quasi-static approximation for χ and q with $\tilde{\chi} = \chi_+$. We used the analytical expression for ε and $\dot{\varepsilon}$ to find suitable values at initial time. To get an idea of the impact of larger oscillations around minima, we attempted initialising at redshift 2.02, where the walls were dangerously close to colliding, but where separated just enough.

It was not until later that we decided to tweak the initial conditions to our advantage, and performed the analysis in Section 5.1.2. Now we could initialise as close to phase transition as we wanted. The catch was now that maybe the surface tension was too different from what we used in Section 4.3, so we spent some time adjusting the expression for σ_w and studying the effect on ε . The result was that only when the fifth-force oscillations are exaggeratedly large was there significant changes in ε .

If we were to do it all over again, it might make sense to set for example $a_* = 2/5$ and $\mathfrak{z}_i = \mathfrak{z}_* = 3/2$, and use the initial conditions $\tilde{\chi} = \chi_*$ and $\tilde{q} = q_*$ from Appendix C, with $\varepsilon = \varepsilon_*$ and $\dot{\varepsilon} = 0$. The advantage that $\dot{z}_w = 0$ is not only that q is less complicated, but we avoid having to include it in χ as well. To account for a moving wall, we should technically perform a Lorentz transformation on the argument to the hyperbolic tangent [6, 35]. In the kink scenario from Section 3.1.1, Eq. (3.3) becomes [35]

$$\phi_k(t, x) = \eta \tanh \left(\sqrt{\frac{\lambda}{2}} \eta \frac{x - vt}{\sqrt{1 - v^2}} \right), \quad (6.4)$$

where v is the speed of the moving defect.

Unsure where this section is best placed.

IF TIME? DESCRIBE PLATEAU IN BEGINNING, AND THE REASONING FOR DISCARDING THOSE RESULTS. EXPLAIN HOW THIS PLATEAU SHOWED UP AGAIN IN THE THIN-WALL LIMIT WHEN CHANGING THE SURFACE TENSION.

Chapter 7

TITLE (Ifs, buts and maybes)

We provide a general discussion of the project—both methodically and result-wise—in Section 7.1 with regrets and proposed methods of verification. In Section 7.2 we address the framework as is, agnostic to any potential (in)validations, and discuss its implications and potential.

7.1 Project reflection

Simulations give substance to the proposed equation of motion for a linear perturbation to the planar wall normal coordinate, Eq. (4.32), in a matter-dominated, conformally flat spacetime. The difference between the analytical and numerical solution to this is insignificant. The anomaly between the Nambu–Goto and full field-theoretical results is more or less consistent in-between simulations, which speaks against any numerical explanations.

With more time, we could have massaged the expression for \tilde{h}_+ more so that we might have obtained an analytical approximation for $\rho_{\text{gw}}(\tau)$ in the thin-wall limit to compare with Fig. 6.6. We elaborate on this in Section 7.1.3.

IDK where to put this: One thing we simply did not have the time or space to do, was to go into detail about how the gravitational waves were computed, and how this might affect the way we interpret the components of $\tilde{\mathbf{h}}_+$. **Write short about this problem!** In doing this analysis properly, we might have gained insight on the fact that $\tilde{\mathbf{h}}_+^{\mathfrak{S}} \sim \tilde{h}_+^{\phi}$ and $\tilde{\mathbf{h}}_+^{\mathfrak{N}} \not\sim \tilde{h}_+^{\phi}$. **For the record, since**

$$\tilde{\mathbf{h}}_{ij}^{\text{new}}(\tilde{\mathbf{n}}) = e^{-i\pi(\tilde{\mathbf{n}}_i + \tilde{\mathbf{n}}_j)/N_{\#}} \tilde{\mathbf{h}}_{ij}(\tilde{\mathbf{n}}),$$

we get

$$\tilde{\mathbf{h}}_{xx}^{\text{new}}(0, \mathbf{v}, \mathbf{w}) = \tilde{\mathbf{h}}_{xx}(0, \mathbf{v}, \mathbf{w})$$

our analysis should be unaffected by this

7.1.1 Open questions

Is the surface tension important? We have seen that time-varying surface tension of domain walls complicates the thin-wall dynamics. The defect formation process is quite quick, in the sense that the system asserts a quasi-static state after a short non-adiabatic phase. The expression we used for the time-varying surface tension in the symmetron model, when inserted into the equation of motion for the wall perturbation, captures the main properties of the damped harmonic oscillatory movement seen in simulations. We established that the discrepancies are not likely due to **blah blah [...]** **no, there was no time ...**

Is there a pure analytic expression for the gravitational waves? It is hard to imagine there exists a pure analytical formula for gravitational waves in the thin-wall limit in our setup, at least for time-dependent surface tension. We could imagine that the **blah blah [...]**

IF TIME: DISCUSSION.

What is the effect of an energy bias? **IF TIME:** DISCUSSION.

7.1.2 Flat-space analogy

Let us review the corresponding scenario in flat spacetime with constant surface tension. The equation of motion for the perturbation to the wall normal coordinate is the simple wave equation $\partial_t^2 \epsilon = (\partial_x^2 + \partial_y^2) \epsilon$. **IF TIME:** DISCUSSION.

7.1.3 Continued assessment

Gravitational waves

The gravitational-wave energy density is given by [29]

$$\rho_{\text{gw}}(\tau) = \frac{1}{16\pi G_N a^4(\tau)} \sum_{P=+, \times} \left\langle \left(\dot{\psi}_P - \mathcal{H} \psi_P \right)^2(\tau, \mathbf{x}) \right\rangle \quad (7.1)$$

For sub-horizon modes

$$\rho_{\text{gw}}(\tau) \simeq \frac{1}{16\pi G_N a^4(\tau)} \sum_{P=+, \times} \left\langle \dot{\psi}^2(\tau, \mathbf{x}) \right\rangle. \quad (7.2)$$

The spatial average [16]

$$\frac{1}{V} \int_{V \gg \lambda^3} d^3x e^{i(\mathbf{k}-\mathbf{k}') \cdot \mathbf{x}} = \frac{(2\pi)^3}{V} \delta^{(3)}(\mathbf{k} - \mathbf{k}') \quad (7.3)$$

where $\lambda \sim 1/k, 1/k'$, we obtain

$$\rho_{\text{gw}}(\tau) \simeq \frac{1}{16\pi G_N a^4(\tau)} \frac{1}{V} \sum_{P=+, \times} \int \frac{d^3k}{(2\pi)^3} \left| \dot{\psi}(\tau, \mathbf{k}) \right|^2. \quad (7.4)$$

One way to use this result is to discretise the above; $dk \rightarrow k_{\#}$, and loop through all possible modes $\tilde{\mathbf{n}}$. Agnostically, this involves solving two integrals numerically $N_{\#}^3$ times for each τ . This brute-force experiment is computationally very inefficient, and it would be much more insightful to find an approximate expression for ρ_{gw} that is analytical, or at least with only fewer computation steps. Such an expression may exist through asymptotic evaluations of Bessel functions, among other things. Not only would this offer an efficient verification strategy, but would also help put this framework into the context of actual gravitational-wave observations.

In-depth gravitational-wave analysis. An interesting analysis would be to systematically change various parameters in the source $\tilde{\pi}_+$ and see what effect this has on the resulting tensor perturbations. From what we gather, it appears that in letting σ_w and/or δ_w be defined from oscillating asymptotic fields $\pm\tilde{\chi}$ instead of χ_{\pm} , \tilde{h}_+ becomes noisier, i.e. with small oscillations around the original result. Changing ε seems to shift the phase of the oscillations. This analysis is far from thorough, which is why we do not present it as a result. To get actual insights, the analysis is huge as \tilde{h}_+ depends on time and a two-dimensional wave vector, and a bunch of other parameters. This is another reason for further attempts at summary statistics that would reduce the dimensionality of the problem drastically.

Simulative experiments

It was indeed very unfortunate that the simulations that were supposed to be updated with optimised initial conditions (cf. simulation 7), were run with a bug that was not detected soon enough. With extended time (and computer) resources, we would have run simulations as described in Section 6.4, preferably with better spatial resolution. Below we describe possible analyses that could come from such fine-grained experiments.

- Actually resolving the Compton wavelength L_C might have shed some light on the contribution from the symmetron field itself to the gravitational radiation. On the other hand, gravitational waves from scalar field fluctuations are expected to peak around the frequency corresponding to L_C^{-1} [24], which is necessarily larger than the Nyquist frequency if $\Delta_\# > 2L_C$. Thus, this contribution should not be relevant for the scales we have been discussing.
- Our attempt to decrease the width of the wall (simulation 6) was not particularly successful. Had we done it again, we would have run the same simulation with better spatial resolution. This could have given insight to the dependence on the wall width in the wall evolution and in turn the gravitational waves.
- Better spatial resolution would allow for smaller initial perturbation amplitude, and thereby help us understand if the discrepancy between the thin-wall approximation and the full theory is due to the perturbation being too large.

There are several other simulation designs that might help isolate important artefacts from the not-so important features. We list a few of these ideas.

- We could look at already-formed walls for which $\tilde{\chi} \simeq 1$ and $\sigma \simeq \sigma_\infty$ to see if and how the time-dependence of the surface tension affects the wall displacement field and metric tensor perturbations. Constant surface tension allows cleaner expressions and model-independence.
- If we change the “nature” of the wall perturbation from a sine to a cosine, this might help in understanding the unpredicted imaginary component of the gravitational waves discussed in Section 6.3.2. This we actually did, but did not prioritise saving and presenting these results. The reader may take my word for it, that the trend was alternating real and imaginary modes, arranged oppositely from the Jacobi–Anger expansion. This is what we would expect. [Maybe this is better placed in Section 6.3.2?](#)
- If we had written the code to also output the Fourier-space SE tensor, we could have compared simulative results to purely analytical expressions. This would make debugging much simpler, and it could help us understand the difference magnitude, among other things. The memory-efficiency of `gevolution` comes at the expense of simplicity and perhaps flexibility, and it is not a completely straight-forward task to make this happen.

7.2 Limitations and possibilities

We review the equations this thin-wall approximation is built on. Let us consider three steps that are not completely independent, but describe a certain order of things.

Step one: Choose a background spacetime, particularly a conformally flat four-dimensional manifold, with conformal factor $a \propto \tau^\alpha$, where $\tau = x^0$ is the conformal time. **Here:** Set $\alpha = 2$ to get matter domination.

Step two: Invoke a (first-order) phase transition at $\tau = \tau_*$, and a scalar boson ϕ responsible for said PT. Choose a scalar-field or scalar–tensor theory with a suitable symmetry-breaking (effective) potential $V_{\text{eff}}(\phi)$. **Here:** Specify that ϕ is the (a)symmetron field, and consider $\kappa = 0$ (symmetron).

Step three: Consider a topological defect that is the product of the aforementioned symmetry break. The defect with vanishing thickness possess dynamics derived from the Nambu–Goto action. Add a perturbation to the wall normal coordinate. We find the TT-part of the corresponding stress–energy tensor and consider this as a source of gravitational waves. **Here:** We consider the domain wall scenario, specifically a planar wall. The equation of motion for this perturbation is expended into eigenvalues and solved thereafter. We use this as input to the Nambu–Goto SE tensor, which in turn source tensor perturbations.

Desired level of analytical solvability is maximum one numerical integration in the resulting tensor perturbation. That is, we want everything up to the defect’s SE tensor in Fourier space to have an analytical expression.

Write about drawbacks?

7.2.1 Improvements

Generalisation

With the above elaboration, we comprise the steps in the following “hierarchy”:

1. Background: four-dimensional spacetime
 - (a) Metric $g_{\mu\nu} = a^2(\tau)\eta_{\mu\nu}$
 - (b) Scale factor $a \propto \tau^\alpha$
 - (c) Matter domination, i.e. $\alpha = 2$
2. Phase transition: quintessence
 - (a) Asymmetron potential
 - (b) Symmetron potential
3. Topological defect: vanishing thickness
 - (a) Domain wall of vanishing thickness
 - (b) Planar wall
 - (c) Wall position trivial, consider small perturbation to wall normal coordinate
 - (d) Choose $\epsilon = \varepsilon(\tau) \sin(py)$

Generalisation from Item 1c to 1b should be uncomplicated. Considering N spatial dimensions is straight-forward, as long as the topological defect is of codimension one (with $D = N - 1$ spatial dimensions). **Comment about coordinates.**

It would have been interesting to study the effect of non-degenerate vacua, e.g. the asymmetron (Item 2b to 2a). Our symmetron results suggest that minor changes in ϕ_\pm —the limits of the integral on the surface tension—do not drastically alter the overall behaviour of the perturbation on the wall. One can imagine that a similar expression for σ would hold for the asymmetron as well. Then there is just the matter of a non-zero vacuum energy difference $v = v_+ - v_-$, but this will also generally be time-dependent, $v = V(\phi_+) - V(\phi_-)$. In Minkowski spacetime and the limit where σ and v are constants, the solution to the equation of motion

corresponding to our setup is the hyperbola [18], and we should expect solution the conformally related flat, FLRW ambient spacetime to inhabit similar features.

We mention that to solve the equation of motion for the (unperturbed) wall normal coordinate would remove the restriction that $\varepsilon_* \ll \tau_*$ (Item 3c to 3a). We address Item 3d below.

Different wall perturbation

We take a look at a scenario in which the solution to Eq. (4.24) is

$$\epsilon = \sum_k \epsilon_k = \sum_k \varepsilon_k \sin(p_k y); \quad p_k = \pi k/L, \quad (7.5)$$

where L is some length scale. We let a_k be weights such that $\sum_k |a_k| = \varepsilon_*$ and $\varepsilon_k = a_k \varepsilon(\tau; p_k)/\varepsilon(\tau_*; p_k)$, where $\varepsilon(\tau; p_k)$ solves Eq. (4.33) for $p = p_k$. Following Section 4.4.2, the xx -component of the stress–energy tensor goes as

$$\tilde{T}_{xx} \sim \delta(k_x) I_s = \delta(k_x) \int dy e^{ik_z \sum_k \epsilon_k} e^{ik_y y}. \quad (7.6)$$

By the same argumentation as in Appendix B.4, we get

$$I_s = 2\pi \sum_{n_1} J_{n_1}(k_z \varepsilon_1) \sum_{n_2} J_{n_2}(k_z \varepsilon_2) \sum_{n_3} J_{n_3}(k_z \varepsilon_3) \cdots \times \delta(k_y + \pi[1n_1 + 2n_2 + 3n_3 + \dots]/L) \quad (7.7)$$

where $n_k \in \mathbb{Z}$. We use the property $J_n(0) = \delta_{n0}$ to check that this reduces to Eq. (B.16a) when there is only one nonzero weight (e.g. $a_1 = \varepsilon_*$).

More compactly, we can write the contribution as

$$I_s = 2\pi \sum_{n_1, n_2, n_3, \dots} J_{n_1}^1 J_{n_2}^2 J_{n_3}^3 \cdots \times \delta(k_y + p_1 \sum_k k n_k) \quad (7.8)$$

where we defined $J_n^k \triangleq J_n(k_z \varepsilon_k)$. Now say a_1 and a_3 are the only non-zero weights. The expression becomes

$$\sum_{n_1, n_3} J_{n_1}^1 J_{n_3}^3 \times \delta(k_y + p_1[n_1 + 3n_3]). \quad (7.9)$$

This means that for modes say $k_y = -10p_1$, the term contributes to the source with $J_{10}^1 J_0^3 + J_6^1 J_4^3 + J_4^1 J_2^3 + J_1^1 J_{-2}^3 + \dots$, i.e. an infinite series of factors $J_{n_1}^1 J_{n_3}^3$ for combinations $n_1 + 3n_3 = 10$, $n_k \in \mathbb{Z}$. Thus,

$$I_s = 2\pi \delta(k_y + Np_1) \sum_{m \in \mathbb{Z}} J_{N-3m}^1 J_m^3 \quad (7.10)$$

for this setup.

Some words about this. This result is regrettable, but not necessarily catastrophic. It is perhaps possible to make use of some identities to simplify I_s , such as

$$\sum_{m \in \mathbb{Z}} J_m(x) J_{n \mp m}(y) = J_n(\pm x + y), \quad (7.11)$$

but time limitations make us have to leave this for another time. To get the full picture, one would have to consider I_a as well, and keep in mind that the TT-projection we did before (Section 4.4.2) was a result of the single Dirac delta, which gave $I_a \propto I_s$ (Eq. (B.16b)). If proven that this blows up, there is reason to believe that the simplified analysis (Appendix B.4) does not hold either.

Comment on why we extract the summation from the integration.

Summary

Chapter 8

Conclusion and Outlook

The Nambu–Goto formulation with time-varying surface tension gives rise to an analytically solvable equation of motion for the planar-wall perturbation in the flat FLRW universe dominated by non-relativistic matter. Simulations show relatively good correspondence with the full theory. There exists loose restrictions for the maximum amplitude of the perturbation and of the scalar field fluctuations.

Validations of the gravitational-wave calculations are inconclusive. Our simulation results show patterns in the gravitational signature that are directly connected to the nature of the wall displacement field, but the exact relations are unclear.

There is a substantial amount of work left if we ever want to compare this to actual gravitational-wave observations.

The results overall are intriguing, and show promise of future analytical estimations of gravitational waves from topological defects. The time-varying surface tension is effectively an additional damping in the equation of motion for the wall displacement field, and during a symmetron phase-transition, there exists explicit solutions to this equation.

8.1 Applications

Similar lines-of-thought should hold for phase transitions in a variety of systems, amongst others the very early universe and particle-physics scenarios. IF TIME! WRITE MORE.

8.2 Future work

Additional validations and analyses are necessary. IF TIME! WRITE MORE.

Bibliography

- [1] B. P. Abbott, R. Abbott, T. D. Abbott, M. R. Abernathy, F. Acernese, K. Ackley, C. Adams, T. Adams, P. Addesso, R. X. Adhikari, V. B. Adya, C. Affeldt, M. Agathos, K. Agatsuma, N. Aggarwal, O. D. Aguiar, L. Aiello, A. Ain, P. Ajith, B. Allen, A. Allocca, P. A. Altin, S. B. Anderson, W. G. Anderson, K. Arai, M. A. Arain, M. C. Araya, C. C. Arceneaux, J. S. Areeda, N. Arnaud, K. G. Arun, S. Ascenzi, G. Ashton, M. Ast, S. M. Aston, P. Astone, P. Aufmuth, C. Aulbert, S. Babak, P. Bacon, M. K. M. Bader, P. T. Baker, F. Baldaccini, G. Ballardín, S. W. Ballmer, J. C. Barayoga, S. E. Barclay, B. C. Barish, D. Barker, F. Barone, B. Barr, L. Barsotti, M. Barsuglia, D. Barta, J. Bartlett, M. A. Barton, I. Bartos, R. Bassiri, A. Basti, J. C. Batch, C. Baune, V. Bavigadda, M. Bazzan, B. Behnke, M. Bejger, C. Belczynski, A. S. Bell, C. J. Bell, B. K. Berger, J. Bergman, G. Bergmann, C. P. L. Berry, D. Bersanetti, A. Bertolini, J. Betzwieser, S. Bhagwat, R. Bhandare, I. A. Bilenko, G. Billingsley, J. Birch, I. A. Birney, O. Birnholtz, S. Biscans, A. Bisht, M. Bitossi, C. Biwer, M. A. Bizouard, J. K. Blackburn, C. D. Blair, D. G. Blair, R. M. Blair, S. Bloemen, O. Bock, T. P. Bodiya, M. Boer, G. Bogaert, C. Bogan, A. Bohe, P. Bojtos, C. Bond, F. Bondu, R. Bonnand, B. A. Boom, R. Bork, V. Boschi, S. Bose, Y. Bouffanais, A. Bozzi, C. Bradaschia, P. R. Brady, V. B. Braginsky, M. Branchesi, J. E. Brau, T. Briant, A. Brillet, M. Brinkmann, V. Brisson, P. Brockill, A. F. Brooks, D. A. Brown, D. D. Brown, N. M. Brown, C. C. Buchanan, A. Buikema, T. Bulik, H. J. Bulten, A. Buonanno, D. Buskulic, C. Buy, R. L. Byer, M. Cabero, L. Cadonati, G. Cagnoli, C. Cahillane, J. Calderón Bustillo, T. Callister, E. Calloni, J. B. Camp, K. C. Cannon, J. Cao, C. D. Capano, E. Capocasa, F. Carbognani, S. Caride, J. Casanueva Diaz, C. Casentini, S. Caudill, M. Cavaglià, F. Cavalier, R. Cavalieri, G. Cella, C. B. Cepeda, L. Cerboni Baiardi, G. Cerretani, E. Cesarini, R. Chakraborty, T. Chalermongsak, S. J. Chamberlin, M. Chan, S. Chao, P. Charlton, E. Chassande-Mottin, H. Y. Chen, Y. Chen, C. Cheng, A. Chincarini, A. Chiummo, H. S. Cho, M. Cho, J. H. Chow, N. Christensen, Q. Chu, S. Chua, S. Chung, G. Ciani, F. Clara, J. A. Clark, F. Cleva, E. Coccia, P. F. Cohadon, A. Colla, C. G. Collette, L. Cominsky, M. Constancio, A. Conte, L. Conti, D. Cook, T. R. Corbitt, N. Cornish, A. Corsi, S. Cortese, C. A. Costa, M. W. Coughlin, S. B. Coughlin, J. P. Coulon, S. T. Countryman, P. Couvares, E. E. Cowan, D. M. Coward, M. J. Cowart, D. C. Coyne, R. Coyne, K. Craig, J. D. E. Creighton, T. D. Creighton, J. Cripe, S. G. Crowder, A. M. Cruise, A. Cumming, L. Cunningham, E. Cuoco, T. Dal Canton, S. L. Danilishin, S. D'Antonio, K. Danzmann, N. S. Darman, C. F. Da Silva Costa, V. Dattilo, I. Dave, H. P. Daveloza, M. Davier, G. S. Davies, E. J. Daw, R. Day, S. De, D. DeBra, G. Debreczeni, J. Degallaix, M. De Laurentis, S. Deléglise, W. Del Pozzo, T. Denker, T. Dent, H. Dereli, V. Dergachev, R. T. DeRosa, R. De Rosa, R. DeSalvo, S. Dhurandhar, M. C. Díaz, L. Di Fiore, M. Di Giovanni, A. Di Lieto, S. Di Pace, I. Di Palma, A. Di Virgilio, G. Dojcinoski, V. Dolique, F. Donovan, K. L. Dooley, S. Doravari, R. Douglas, T. P. Downes, M. Drago, R. W. P. Drever, J. C. Driggers, Z. Du, M. Ducrot, S. E. Dwyer, T. B. Edo, M. C. Edwards, A. Effler, H. B. Eggenstein, P. Ehrens,

J. Eichholz, S. S. Eikenberry, W. Engels, R. C. Essick, T. Etzel, M. Evans, T. M. Evans, R. Everett, M. Factourovich, V. Fafone, H. Fair, S. Fairhurst, X. Fan, Q. Fang, S. Farinon, B. Farr, W. M. Farr, M. Favata, M. Fays, H. Fehrmann, M. M. Fejer, D. Feldbaum, I. Ferrante, E. C. Ferreira, F. Ferrini, F. Fidecaro, L. S. Finn, I. Fiori, D. Fiorucci, R. P. Fisher, R. Flaminio, M. Fletcher, H. Fong, J. D. Fournier, S. Franco, S. Frasca, F. Frasconi, M. Frede, Z. Frei, A. Freise, R. Frey, V. Frey, T. T. Fricke, P. Fritschel, V. V. Frolov, P. Fulda, M. Fyffe, H. A. G. Gabbard, J. R. Gair, L. Gammaitoni, S. G. Gaonkar, F. Garufi, A. Gatto, G. Gaur, N. Gehrels, G. Gemme, B. Gendre, E. Genin, A. Gennai, J. George, L. Gergely, V. Germain, Abhirup Ghosh, Archisman Ghosh, S. Ghosh, J. A. Giaime, K. D. Giardina, A. Giazotto, K. Gill, A. Glaefke, J. R. Gleason, E. Goetz, R. Goetz, L. Gondan, G. González, J. M. Gonzalez Castro, A. Gopakumar, N. A. Gordon, M. L. Gorodetsky, S. E. Gossan, M. Gosselin, R. Gouaty, C. Graef, P. B. Graff, M. Granata, A. Grant, S. Gras, C. Gray, G. Greco, A. C. Green, R. J. S. Greenhalgh, P. Groot, H. Grote, S. Grunewald, G. M. Guidi, X. Guo, A. Gupta, M. K. Gupta, K. E. Gushwa, E. K. Gustafson, R. Gustafson, J. J. Hacker, B. R. Hall, E. D. Hall, G. Hammond, M. Haney, M. M. Hanke, J. Hanks, C. Hanna, M. D. Hannam, J. Hanson, T. Hardwick, J. Harms, G. M. Harry, I. W. Harry, M. J. Hart, M. T. Hartman, C. J. Haster, K. Haughian, J. Healy, J. Heefner, A. Heidmann, M. C. Heintze, G. Heinzl, H. Heitmann, P. Hello, G. Hemming, M. Hendry, I. S. Heng, J. Hennig, A. W. Heptonstall, M. Heurs, S. Hild, D. Hoak, K. A. Hodge, D. Hofman, S. E. Hollitt, K. Holt, D. E. Holz, P. Hopkins, D. J. Hosken, J. Hough, E. A. Houston, E. J. Howell, Y. M. Hu, S. Huang, E. A. Huerta, D. Huet, B. Hughey, S. Husa, S. H. Huttner, T. Huynh-Dinh, A. Idrisy, N. Indik, D. R. Ingram, R. Inta, H. N. Isa, J. M. Isac, M. Isi, G. Islas, T. Isogai, B. R. Iyer, K. Izumi, M. B. Jacobson, T. Jacqmin, H. Jang, K. Jani, P. Jaranowski, S. Jawahar, F. Jiménez-Forteza, W. W. Johnson, N. K. Johnson-McDaniel, D. I. Jones, R. Jones, R. J. G. Jonker, L. Ju, K. Haris, C. V. Kalaghatgi, V. Kalogera, S. Kandhasamy, G. Kang, J. B. Kanner, S. Karki, M. Kasprzack, E. Katsavounidis, W. Katzman, S. Kaufer, T. Kaur, K. Kawabe, F. Kawazoe, F. Kéfélian, M. S. Kehl, D. Keitel, D. B. Kelley, W. Kells, R. Kennedy, D. G. Keppel, J. S. Key, A. Khalaidovski, F. Y. Khalili, I. Khan, S. Khan, Z. Khan, E. A. Khazanov, N. Kijbunchoo, C. Kim, J. Kim, K. Kim, Nam-Gyu Kim, Namjun Kim, Y. M. Kim, E. J. King, P. J. King, D. L. Kinzel, J. S. Kissel, L. Kleybolte, S. Klimenko, S. M. Koehlenbeck, K. Kokeyama, S. Koley, V. Kondrashov, A. Kontos, S. Koranda, M. Korobko, W. Z. Korth, I. Kowalska, D. B. Kozak, V. Kringel, B. Krishnan, A. Królak, C. Krueger, G. Kuehn, P. Kumar, R. Kumar, L. Kuo, A. Kutynia, P. Kwee, B. D. Lackey, M. Landry, J. Lange, B. Lantz, P. D. Lasky, A. Lazzarini, C. Lazzaro, P. Leaci, S. Leavey, E. O. Lebigot, C. H. Lee, H. K. Lee, H. M. Lee, K. Lee, A. Lenon, M. Leonardi, J. R. Leong, N. Leroy, N. Letendre, Y. Levin, B. M. Levine, T. G. F. Li, A. Libson, T. B. Littenberg, N. A. Lockerbie, J. Logue, A. L. Lombardi, L. T. London, J. E. Lord, M. Lorenzini, V. Loriette, M. Lormand, G. Losurdo, J. D. Lough, C. O. Lousto, G. Lovelace, H. Lück, A. P. Lundgren, J. Luo, R. Lynch, Y. Ma, T. MacDonald, B. Machenschalk, M. MacInnis, D. M. Macleod, F. Magaña-Sandoval, R. M. Magee, M. Mageswaran, E. Majorana, I. Maksimovic, V. Malvezzi, N. Man, I. Mandel, V. Mandic, V. Mangano, G. L. Mansell, M. Manske, M. Mantovani, F. Marchesoni, F. Marion, S. Márka, Z. Márka, A. S. Markosyan, E. Maros, F. Martelli, L. Martellini, I. W. Martin, R. M. Martin, D. V. Martynov, J. N. Marx, K. Mason, A. Masserot, T. J. Massinger, M. Masso-Reid, F. Matichard, L. Matone, N. Mavalvala, N. Mazumder, G. Mazzolo, R. McCarthy, D. E. McClelland, S. McCormick, S. C. McGuire, G. McIntyre, J. McIver, D. J. McManus, S. T. McWilliams, D. Meacher, G. D. Meadors, J. Meidam, A. Melatos, G. Mendell, D. Mendoza-Gandara, R. A. Mercer, E. Merilh, M. Merzougui, S. Meshkov, C. Messenger,

C. Messick, P. M. Meyers, F. Mezzani, H. Miao, C. Michel, H. Middleton, E. E. Mikhailov, L. Milano, J. Miller, M. Millhouse, Y. Minenkov, J. Ming, S. Mirshekari, C. Mishra, S. Mitra, V. P. Mitrofanov, G. Mitselmakher, R. Mittleman, A. Moggi, M. Mohan, S. R. P. Mohapatra, M. Montani, B. C. Moore, C. J. Moore, D. Moraru, G. Moreno, S. R. Morris, K. Mossavi, B. Mours, C. M. Mow-Lowry, C. L. Mueller, G. Mueller, A. W. Muir, Arunava Mukherjee, D. Mukherjee, S. Mukherjee, N. Mukund, A. Mullavey, J. Munch, D. J. Murphy, P. G. Murray, A. Mytidis, I. Nardecchia, L. Naticchioni, R. K. Nayak, V. Necula, K. Nedkova, G. Nelemans, M. Neri, A. Neunzert, G. Newton, T. T. Nguyen, A. B. Nielsen, S. Nissanke, A. Nitz, F. Nocera, D. Nolting, M. E. N. Normandin, L. K. Nuttall, J. Oberling, E. Ochsner, J. O'Dell, E. Oelker, G. H. Ogin, J. J. Oh, S. H. Oh, F. Ohme, M. Oliver, P. Oppermann, Richard J. Oram, B. O'Reilly, R. O'Shaughnessy, C. D. Ott, D. J. Ottaway, R. S. Ottens, H. Overmier, B. J. Owen, A. Pai, S. A. Pai, J. R. Palamos, O. Palashov, C. Palomba, A. Pal-Singh, H. Pan, Y. Pan, C. Pankow, F. Pannarale, B. C. Pant, F. Paoletti, A. Paoli, M. A. Papa, H. R. Paris, W. Parker, D. Pascucci, A. Pasqualetti, R. Passaquieti, D. Passuello, B. Patricelli, Z. Patrick, B. L. Pearlstone, M. Pedraza, R. Pedurand, L. Pekowsky, A. Pele, S. Penn, A. Perreca, H. P. Pfeiffer, M. Phelps, O. Piccinni, M. Pichot, M. Pickenpack, F. Piergiovanni, V. Pierro, G. Pillant, L. Pinard, I. M. Pinto, M. Pitkin, J. H. Poeld, R. Poggiani, P. Popolizio, A. Post, J. Powell, J. Prasad, V. Predoi, S. S. Premachandra, T. Prestegard, L. R. Price, M. Prijatelj, M. Principe, S. Privitera, R. Prix, G. A. Prodi, L. Prokhorov, O. Puncken, M. Punturo, P. Puppo, M. Pürner, H. Qi, J. Qin, V. Quetschke, E. A. Quintero, R. Quitzow-James, F. J. Raab, D. S. Rabeling, H. Radkins, P. Raffai, S. Raja, M. Rakhmanov, C. R. Ramet, P. Rapagnani, V. Raymond, M. Razzano, V. Re, J. Read, C. M. Reed, T. Regimbau, L. Rei, S. Reid, D. H. Reitze, H. Rew, S. D. Reyes, F. Ricci, K. Riles, N. A. Robertson, R. Robie, F. Robinet, A. Rocchi, L. Rolland, J. G. Rollins, V. J. Roma, J. D. Romano, R. Romano, G. Romanov, J. H. Romie, D. Rosińska, S. Rowan, A. Rüdiger, P. Ruggi, K. Ryan, S. Sachdev, T. Sadecki, L. Sadeghian, L. Salconi, M. Saleem, F. Salemi, A. Samajdar, L. Sammut, L. M. Sampson, E. J. Sanchez, V. Sandberg, B. Sandeen, G. H. Sanders, J. R. Sanders, B. Sassolas, B. S. Sathyaprakash, P. R. Saulson, O. Sauter, R. L. Savage, A. Sawadsky, P. Schale, R. Schilling, J. Schmidt, P. Schmidt, R. Schnabel, R. M. S. Schofield, A. Schönbeck, E. Schreiber, D. Schuette, B. F. Schutz, J. Scott, S. M. Scott, D. Sellers, A. S. Sengupta, D. Sentenac, V. Sequino, A. Sergeev, G. Serna, Y. Setyawati, A. Sevigny, D. A. Shaddock, T. Shaffer, S. Shah, M. S. Shahriar, M. Shaltev, Z. Shao, B. Shapiro, P. Shawhan, A. Sheperd, D. H. Shoemaker, D. M. Shoemaker, K. Siellez, X. Siemens, D. Sigg, A. D. Silva, D. Simakov, A. Singer, L. P. Singer, A. Singh, R. Singh, A. Singhal, A. M. Sintès, B. J. J. Slagmolen, J. R. Smith, M. R. Smith, N. D. Smith, R. J. E. Smith, E. J. Son, B. Sorazu, F. Sorrentino, T. Souradeep, A. K. Srivastava, A. Staley, M. Steinke, J. Steinlechner, S. Steinlechner, D. Steinmeyer, B. C. Stephens, S. P. Stevenson, R. Stone, K. A. Strain, N. Straniero, G. Stratta, N. A. Strauss, S. Strigin, R. Sturani, A. L. Stuver, T. Z. Summerscales, L. Sun, P. J. Sutton, B. L. Swinkels, M. J. Szczepańczyk, M. Tacca, D. Talukder, D. B. Tanner, M. Tápai, S. P. Tarabrin, A. Taracchini, R. Taylor, T. Theeg, M. P. Thirugnanasambandam, E. G. Thomas, M. Thomas, P. Thomas, K. A. Thorne, K. S. Thorne, E. Thrane, S. Tiwari, V. Tiwari, K. V. Tokmakov, C. Tomlinson, M. Tonelli, C. V. Torres, C. I. Torrie, D. Töyrä, F. Travasso, G. Traylor, D. Trifirò, M. C. Tringali, L. Trozzo, M. Tse, M. Turconi, D. Tuyenbayev, D. Ugolini, C. S. Unnikrishnan, A. L. Urban, S. A. Usman, H. Vahlbruch, G. Vajente, G. Valdes, M. Vallisneri, N. van Bakel, M. van Beuzekom, J. F. J. van den Brand, C. Van Den Broeck, D. C. Vander-Hyde, L. van der Schaaf, J. V. van Heijningen, A. A. van Veggel, M. Vardaro, S. Vass, M. Vasúth, R. Vaulin, A. Vecchio, G. Vedovato, J. Veitch, P. J. Veitch, K. Venkateswara, D. Verkindt,

- F. Vetrano, A. Viceré, S. Vinciguerra, D. J. Vine, J. Y. Vinet, S. Vitale, T. Vo, H. Vocca, C. Vorvick, D. Voss, W. D. Voudsen, S. P. Vyatchanin, A. R. Wade, L. E. Wade, M. Wade, S. J. Waldman, M. Walker, L. Wallace, S. Walsh, G. Wang, H. Wang, M. Wang, X. Wang, Y. Wang, H. Ward, R. L. Ward, J. Warner, M. Was, B. Weaver, L. W. Wei, M. Weinert, A. J. Weinstein, R. Weiss, T. Welborn, L. Wen, P. Weßels, T. Westphal, K. Wette, J. T. Whelan, S. E. Whitcomb, D. J. White, B. F. Whiting, K. Wiesner, C. Wilkinson, P. A. Willems, L. Williams, R. D. Williams, A. R. Williamson, J. L. Willis, B. Willke, M. H. Wimmer, L. Winkelmann, W. Winkler, C. C. Wipf, A. G. Wiseman, H. Wittel, G. Woan, J. Worden, J. L. Wright, G. Wu, J. Yablon, I. Yakushin, W. Yam, H. Yamamoto, C. C. Yancey, M. J. Yap, H. Yu, M. Yvert, A. Zadrożny, L. Zangrando, M. Zanolin, J. P. Zendri, M. Zevin, F. Zhang, L. Zhang, M. Zhang, Y. Zhang, C. Zhao, M. Zhou, Z. Zhou, X. J. Zhu, M. E. Zucker, S. E. Zuraw, J. Zweizig, LIGO Scientific Collaboration, and Virgo Collaboration. Observation of Gravitational Waves from a Binary Black Hole Merger. *Physical Review Letters*, 116:061102, February 2016. ISSN 0031-9007. doi: 10.1103/PhysRevLett.116.061102. URL <https://ui.adsabs.harvard.edu/abs/2016PhRvL.116f1102A>.
- [2] Julian Adamek, David Daverio, Ruth Durrer, and Martin Kunz. Gevolution: A cosmological N-body code based on General Relativity. *Journal of Cosmology and Astroparticle Physics*, 2016(07):053–053, July 2016. ISSN 1475-7516. doi: 10.1088/1475-7516/2016/07/053. URL <http://arxiv.org/abs/1604.06065>.
- [3] Adeela Afzal, Gabriella Agazie, Akash Anumalapudi, Anne M. Archibald, Zaven Arzoumanian, Paul T. Baker, Bence Bécsy, Jose Juan Blanco-Pillado, Laura Blecha, Kimberly K. Boddy, Adam Brazier, Paul R. Brook, Sarah Burke-Spolaor, Rand Burnette, Robin Case, Maria Charisi, Shami Chatterjee, Katerina Chatziioannou, Belinda D. Cheeseboro, Siyuan Chen, Tyler Cohen, James M. Cordes, Neil J. Cornish, Fronefield Crawford, H. Thankful Cromartie, Kathryn Crowter, Curt J. Cutler, Megan E. Decesar, Dallas Degan, Paul B. Demorest, Heling Deng, Timothy Dolch, Brendan Drachler, Richard von Eckardstein, Elizabeth C. Ferrara, William Fiore, Emmanuel Fonseca, Gabriel E. Freedman, Nate Garver-Daniels, Peter A. Gentile, Kyle A. Gersbach, Joseph Glaser, Deborah C. Good, Lydia Guertin, Kayhan Gültekin, Jeffrey S. Hazboun, Sophie Hourihane, Kristina Islo, Ross J. Jennings, Aaron D. Johnson, Megan L. Jones, Andrew R. Kaiser, David L. Kaplan, Luke Zoltan Kelley, Matthew Kerr, Joey S. Key, Nima Laal, Michael T. Lam, William G. Lamb, T. Joseph W. Lazio, Vincent S. H. Lee, Natalia Lewandowska, Rafael R. Lino Dos Santos, Tyson B. Littenberg, Tingting Liu, Duncan R. Lorimer, Jing Luo, Ryan S. Lynch, Chung-Pei Ma, Dustin R. Madison, Alexander McEwen, James W. McKee, Maura A. McLaughlin, Natasha McMann, Bradley W. Meyers, Patrick M. Meyers, Chiara M. F. Mingarelli, Andrea Mitridate, Jonathan Nay, Priyamvada Natarajan, Cherry Ng, David J. Nice, Stella Koch Ocker, Ken D. Oloom, Timothy T. Pennucci, Benetge B. P. Perera, Polina Petrov, Nihan S. Pol, Henri A. Radovan, Scott M. Ransom, Paul S. Ray, Joseph D. Romano, Shashwat C. Sardesai, Ann Schmiedekamp, Carl Schmiedekamp, Kai Schmitz, Tobias Schröder, Levi Schult, Brent J. Shapiro-Albert, Xavier Siemens, Joseph Simon, Magdalena S. Siwek, Ingrid H. Stairs, Daniel R. Stinebring, Kevin Stovall, Peter Stratmann, Jerry P. Sun, Abhimanyu Susobhanan, Joseph K. Swiggum, Jacob Taylor, Stephen R. Taylor, Tanner Trickle, Jacob E. Turner, Caner Unal, Michele Vallisneri, Sonali Verma, Sarah J. Vigeland, Haley M. Wahl, Qiaohong Wang, Caitlin A. Witt, David Wright, Olivia Young, Kathryn M. Zurek, and Nanograv Collaboration. The NANOGrav 15 yr Data Set: Search for Signals from New Physics. *The Astrophysical Journal*, 951:L11, July 2023. ISSN 0004-637X. doi: 10.3847/2041-8213/acdc91. URL <https://ui.adsabs.harvard.edu/abs/2023ApJ...951L..11A>.

- [4] Gabriella Agazie, Akash Anumalapudi, Anne M. Archibald, Zaven Arzoumanian, Paul T. Baker, Bence Bécsey, Laura Blecha, Adam Brazier, Paul R. Brook, Sarah Burke-Spolaor, Rand Burnette, Robin Case, Maria Charisi, Shami Chatterjee, Katerina Chatziioannou, Belinda D. Cheeseboro, Siyuan Chen, Tyler Cohen, James M. Cordes, Neil J. Cornish, Fronefield Crawford, H. Thankful Cromartie, Kathryn Crowter, Curt J. Cutler, Megan E. Decesar, Dallas Degan, Paul B. Demorest, Heling Deng, Timothy Dolch, Brendan Drachler, Justin A. Ellis, Elizabeth C. Ferrara, William Fiore, Emmanuel Fonseca, Gabriel E. Freedman, Nate Garver-Daniels, Peter A. Gentile, Kyle A. Gersbach, Joseph Glaser, Deborah C. Good, Kayhan Gültekin, Jeffrey S. Hazboun, Sophie Hourihane, Kristina Islo, Ross J. Jennings, Aaron D. Johnson, Megan L. Jones, Andrew R. Kaiser, David L. Kaplan, Luke Zoltan Kelley, Matthew Kerr, Joey S. Key, Tonia C. Klein, Nima Laal, Michael T. Lam, William G. Lamb, T. Joseph W. Lazio, Natalia Lewandowska, Tyson B. Littenberg, Tingting Liu, Andrea Lommen, Duncan R. Lorimer, Jing Luo, Ryan S. Lynch, Chung-Pei Ma, Dustin R. Madison, Margaret A. Mattson, Alexander McEwen, James W. McKee, Maura A. McLaughlin, Natasha McMann, Bradley W. Meyers, Patrick M. Meyers, Chiara M. F. Mingarelli, Andrea Mitridate, Priyamvada Natarajan, Cherry Ng, David J. Nice, Stella Koch Ocker, Ken D. Olum, Timothy T. Pennucci, Benetge B. P. Perera, Polina Petrov, Nihan S. Pol, Henri A. Radovan, Scott M. Ransom, Paul S. Ray, Joseph D. Romano, Shashwat C. Sardesai, Ann Schmiedekamp, Carl Schmiedekamp, Kai Schmitz, Levi Schult, Brent J. Shapiro-Albert, Xavier Siemens, Joseph Simon, Magdalena S. Siwek, Ingrid H. Stairs, Daniel R. Stinebring, Kevin Stovall, Jerry P. Sun, Abhimanyu Susobhanan, Joseph K. Swiggum, Jacob Taylor, Stephen R. Taylor, Jacob E. Turner, Caner Unal, Michele Vallisneri, Rutger van Haasteren, Sarah J. Vigeland, Haley M. Wahl, Qiaohong Wang, Caitlin A. Witt, Olivia Young, and Nanograv Collaboration. The NANOGrav 15 yr Data Set: Evidence for a Gravitational-wave Background. *The Astrophysical Journal*, 951:L8, July 2023. ISSN 0004-637X. doi: 10.3847/2041-8213/acdac6. URL <https://ui.adsabs.harvard.edu/abs/2023ApJ...951L...8A>.
- [5] E. Babichev, D. Gorbunov, S. Ramazanov, R. Samanta, and A. Vikman. NANOGrav spectral index $\gamma=3$ from melting domain walls, July 2023. URL <http://arxiv.org/abs/2307.04582>.
- [6] Jose J. Blanco-Pillado, Daniel Jiménez-Aguilar, Jose M. Queiruga, and Jon Urrestilla. The dynamics of Domain Wall Strings. *Journal of Cosmology and Astroparticle Physics*, 2023(05):011, May 2023. ISSN 1475-7516. doi: 10.1088/1475-7516/2023/05/011. URL <http://arxiv.org/abs/2209.12945>.
- [7] Clare Burrage, Bradley March, and Aneesh P. Naik. Accurate computation of the screening of scalar fifth forces in galaxies. *Journal of Cosmology and Astroparticle Physics*, 2024:004, April 2024. ISSN 1475-7516. doi: 10.1088/1475-7516/2024/04/004. URL <https://ui.adsabs.harvard.edu/abs/2024JCAP...04..004B>.
- [8] Sean M. Carroll. *Spacetime and Geometry: An Introduction to General Relativity*. Cambridge University Press, July 2019. ISBN 978-0-8053-8732-2 978-1-108-48839-6 978-1-108-77555-7.
- [9] Øyvind Christiansen. *Cosmological Simulations of Phase Transitions in Screened Scalar-Tensor Gravity: Cosmic Acceleration, Topological Defects, Gravitational Waves and Relativistic Observables*. Doctoral thesis, 2024. URL <https://www.duo.uio.no/handle/10852/113638>.

- [10] Øyvind Christiansen, Farbod Hassani, Mona Jalilvand, and David F. Mota. Asevolution: A relativistic N-body implementation of the (a)symmetron. *Journal of Cosmology and Astroparticle Physics*, 2023(05):009, May 2023. ISSN 1475-7516. doi: 10.1088/1475-7516/2023/05/009. URL <https://iopscience.iop.org/article/10.1088/1475-7516/2023/05/009>.
- [11] Øyvind Christiansen, Julian Adamek, Farbod Hassani, and David F. Mota. Gravitational waves from dark domain walls, January 2024. URL <https://ui.adsabs.harvard.edu/abs/2024arXiv240102409C>.
- [12] Øyvind Christiansen, Farbod Hassani, and David F. Mota. Asimulation: Domain formation and impact on observables in resolved cosmological simulations of the (a)symmetron. *Astronomy and Astrophysics*, 689:A6, September 2024. ISSN 0004-6361. doi: 10.1051/0004-6361/202449188. URL <https://ui.adsabs.harvard.edu/abs/2024A&A...689A...6C>.
- [13] Daniel Cutting, Elba Granados Escartin, Mark Hindmarsh, and David J. Weir. Gravitational waves from vacuum first-order phase transitions. II. From thin to thick walls. *Physical Review D*, 103(2):023531, January 2021. doi: 10.1103/PhysRevD.103.023531. URL <https://link.aps.org/doi/10.1103/PhysRevD.103.023531>.
- [14] M. P. Dąbrowski, J. Garecki, and D. B. Blaschke. Conformal transformations and conformal invariance in gravitation. *Annalen der Physik*, 521:13–32, February 2009. ISSN 0003-3804. doi: 10.1002/andp.2009521010510.1002/andp.200810331. URL <https://ui.adsabs.harvard.edu/abs/2009AnP...521...13D>.
- [15] David Daverio, Mark Hindmarsh, and Neil Bevis. Latfield2: A c++ library for classical lattice field theory, January 2016. URL <http://arxiv.org/abs/1508.05610>.
- [16] Jean Francois Dufaux, Amanda Bergman, Gary N. Felder, Lev Kofman, and Jean-Philippe Uzan. Theory and Numerics of Gravitational Waves from Preheating after Inflation. *Physical Review D*, 76(12):123517, December 2007. ISSN 1550-7998, 1550-2368. doi: 10.1103/PhysRevD.76.123517. URL <http://arxiv.org/abs/0707.0875>.
- [17] Sébastien Fumeron and Bertrand Berche. Introduction to topological defects: From liquid crystals to particle physics. *European Physical Journal Special Topics*, 232:1813–1833, September 2023. ISSN 1951-6355. doi: 10.1140/epjs/s11734-023-00803-x. URL <https://ui.adsabs.harvard.edu/abs/2023EPJST.232.1813F>.
- [18] Jaume Garriga and Alexander Vilenkin. Perturbations on domain walls and strings: A covariant theory. *Physical Review D*, 44:1007–1014, August 1991. ISSN 1550-79980556-2821. doi: 10.1103/PhysRevD.44.1007. URL <https://ui.adsabs.harvard.edu/abs/1991PhRvD..44.1007G>.
- [19] Jemal Guven. Perturbations of a topological defect as a theory of coupled scalar fields in curved space interacting with an external vector potential. *Physical Review D*, 48:5562–5569, December 1993. ISSN 1550-79980556-2821. doi: 10.1103/PhysRevD.48.5562. URL <https://ui.adsabs.harvard.edu/abs/1993PhRvD..48.5562G>.
- [20] Kurt Hinterbichler and Justin Khoury. Screening Long-Range Forces through Local Symmetry Restoration. *Physical Review Letters*, 104:231301, June 2010. ISSN 0031-9007. doi: 10.1103/PhysRevLett.104.231301. URL <https://ui.adsabs.harvard.edu/abs/2010PhRvL.104w1301H>.

- [21] Kurt Hinterbichler, Justin Khoury, Aaron Levy, and Andrew Matas. Symmetron cosmology. *Physical Review D*, 84(10):103521, November 2011. doi: 10.1103/PhysRevD.84.103521. URL <https://link.aps.org/doi/10.1103/PhysRevD.84.103521>.
- [22] Akihiro Ishibashi and Hideki Ishihara. Equation of motion for a domain wall coupled to gravitational field. *Physical Review D*, 60(12):124016, November 1999. ISSN 0556-2821, 1089-4918. URL <http://arxiv.org/abs/gr-qc/9802036>.
- [23] Niko Jokela, K. Kajantie, and Miika Sarkkinen. Gravitational wave memory and its tail in cosmology. *Physical Review D*, 106:064022, September 2022. ISSN 1550-7998/0556-2821. doi: 10.1103/PhysRevD.106.064022. URL <https://ui.adsabs.harvard.edu/abs/2022PhRvD.106f4022J>.
- [24] Masahiro Kawasaki and Ken'ichi Saikawa. Study of gravitational radiation from cosmic domain walls. *Journal of Cosmology and Astroparticle Physics*, 2011(09):008–008, September 2011. ISSN 1475-7516. doi: 10.1088/1475-7516/2011/09/008. URL <http://arxiv.org/abs/1102.5628>.
- [25] Edward W. Kolb. *The Early Universe*, volume 69 of *Frontiers in Physics*. Addison-Wesley, Redwood City, Calif, 1990. ISBN 978-0-201-11603-8.
- [26] Xiu-Fei Li. Probing the high temperature symmetry breaking with gravitational waves from domain walls, July 2023. URL <https://ui.adsabs.harvard.edu/abs/2023arXiv230703163L>.
- [27] Claudio Llinares and Levon Pogosian. Domain walls coupled to matter: The symmetron example. *Physical Review D*, 90(12):124041, December 2014. doi: 10.1103/PhysRevD.90.124041. URL <https://link.aps.org/doi/10.1103/PhysRevD.90.124041>.
- [28] Michele Maggiore. *Gravitational Waves. Vol. 1: Theory and Experiments*. Oxford University Press, 2007. ISBN 978-0-19-171766-6 978-0-19-852074-0. doi: 10.1093/acprof:oso/9780198570745.001.0001.
- [29] Michele Maggiore. *Gravitational Waves. Vol. 2: Astrophysics and Cosmology*. Oxford University Press, March 2018. ISBN 978-0-19-857089-9.
- [30] Leandros Perivolaropoulos and Foteini Skara. Gravitational transitions via the explicitly broken symmetron screening mechanism. *Physical Review D*, 106(4):043528, August 2022. ISSN 2470-0010, 2470-0029. doi: 10.1103/PhysRevD.106.043528. URL <http://arxiv.org/abs/2203.10374>.
- [31] William H. Press, Barbara S. Ryden, and David N. Spergel. Dynamical Evolution of Domain Walls in an Expanding Universe. *The Astrophysical Journal*, 347:590, December 1989. ISSN 0004-637X. doi: 10.1086/168151. URL <https://ui.adsabs.harvard.edu/abs/1989ApJ...347..590P>.
- [32] S. Ramazanov, E. Babichev, D. Gorbunov, and A. Vikman. Beyond freeze-in: Dark matter via inverse phase transition and gravitational wave signal. *Physical Review D*, 105(6):063530, March 2022. ISSN 2470-0010, 2470-0029. doi: 10.1103/PhysRevD.105.063530. URL <https://link.aps.org/doi/10.1103/PhysRevD.105.063530>.
- [33] Ken'ichi Saikawa. A Review of Gravitational Waves from Cosmic Domain Walls. *Universe*, 3(2):40, May 2017. ISSN 2218-1997. doi: 10.3390/universe3020040. URL <http://www.mdpi.com/2218-1997/3/2/40>.

Bibliography

- [34] The Sage Developers. *SageMath, the Sage Mathematics Software System (Version 10.1)*, 2023.
- [35] Tanmay Vachaspati. *Kinks and Domain Walls: An Introduction to Classical and Quantum Solitons*. Cambridge University Press, Cambridge, 2006. ISBN 978-0-521-83605-0. doi: 10.1017/CBO9780511535192. URL <https://www.cambridge.org/core/books/kinks-and-domain-walls/98D525CCD885D53F51BDFC3B08A711A6>.
- [36] Alexander Vilenkin and E. Paul S. Shellard. *Cosmic Strings and Other Topological Defects*. January 1994. URL <https://ui.adsabs.harvard.edu/abs/1994csot.book....V>.

Appendices

Appendix A

TITLE (Cylinder Functions)

We will in the following define the first and second kinds of the (regular) Bessel functions, spherical Bessel functions and Riccati–Bessel functions, collectively denoted Z , z and R , respectively. The second kinds are also called the Neumann, spherical Neumann and Riccati–Neumann functions. Conventions are shown in Table A.1, and we use $\nu \in \mathbb{C}$ and $n \in \mathbb{Z}$ to denote the order.

Type	Combination	1st kind	2nd kind	i th kind
Bessel functions	Z_ν	J_ν	Y_ν	$Z_\nu^{(i)}(x)$
Spherical Bessel functions	z_n	j_n	y_n	$z_n^{(i)}(x) = \sqrt{\pi/(2x)} \cdot Z_{n+1/2}^{(i)}(x)$
Riccati–Bessel functions	R_n	S_n	C_n	$R_n^{(i)}(x) = -(-1)^i x \cdot Z_n^{(i)}(x)$

Table A.1: Types of Bessel functions and conventions. Here, $\nu \in \mathbb{C}$ and $n \in \mathbb{Z}$ are constants, and $x \in \mathbb{C}$ is a variable. Linear combinations of the first and second kinds are denoted in the second column. Subscripts mean order, and parenthesised superscripts refer to kind.

The general solution to Bessel’s differential equation ($' \equiv d/dx$)

$$x^2 y'' + xy' + (x^2 - \nu^2)y = 0 \quad (\text{A.1})$$

is $y(x) = Z_\nu(x)$; a linear combination of the (regular) ν th-order **Bessel** (first kind, J_ν) and **Neumann** (second kind, Y_ν) **functions**.

The solution to a similar equation

$$x^2 y'' + x(1 - 2a)y' + [(bcx^c)^2 + (a^2 - \nu^2 c^2)]y = 0 \quad (\text{A.2})$$

is $y(x) = x^a Z_\nu(bx^c)$. A variation of this is the spherical Bessel’s equation

$$x^2 y'' + 2xy' + (x^2 - n(n + 1))y = 0 \quad (\text{A.3})$$

has the general solution $y(x) = z_n(x)$; a linear combination of the **spherical Bessel** (first kind, j_n) and **Neumann** (second kind, y_n) **functions**. Another useful class of solutions is the general solution to

$$x^2 y'' + (x^2 - n(n + 1))y = 0, \quad (\text{A.4})$$

which is $y(x) = R_n(x)$; a linear combination of the **Riccati–Bessel** (first kind, S_n) and **Riccati–Neumann** (second kind, C_n) **functions**.

A.1 Explicit formulas

A.1.1 Integer order

Bessel functions of integer order, the Z_n 's are given by

$$J_n(x) = \frac{1}{\pi} \int_0^\pi dy \cos(ny - x \sin y) \quad (\text{A.5a})$$

and

$$Y_n(x) = \lim_{\nu \rightarrow n} Y_\nu(x), \quad (\text{A.5b})$$

where

$$Y_\nu(x) = \frac{J_\nu(x) \cos \pi \nu - J_{-\nu}(x)}{\sin \pi \nu}; \quad \nu \notin \mathbb{Z}. \quad (\text{A.5c})$$

Furthermore,

$$Z_{-n}(x) = (-1)^n Z_n(x). \quad (\text{A.6})$$

A.1.2 Half-integer order

If $\nu = n + \frac{1}{2}$, we have $Z_{n+1/2}(x) = \sqrt{2x/\pi} Z_n(x)$ where

$$j_n(x) = +x^n \left(-\frac{1}{x} \frac{d}{dx} \right)^n \left(\frac{\sin x}{x} \right), \quad (\text{A.7a})$$

$$y_n(x) = -x^n \left(-\frac{1}{x} \frac{d}{dx} \right)^n \left(\frac{\cos x}{x} \right). \quad (\text{A.7b})$$

Observe that

$$j_n(x) = (-1)^n y_{-(n+1)}(x), \quad (\text{A.8a})$$

$$y_n(x) = (-1)^{n+1} j_{-(n+1)}(x). \quad (\text{A.8b})$$

$$(\text{A.8c})$$

We have

$$S_n(x) = +x j_n(x) = +\sqrt{\frac{\pi x}{2}} J_{n+1/2}(x), \quad (\text{A.9a})$$

$$C_n(x) = -x y_n(x) = -\sqrt{\frac{\pi x}{2}} Y_{n+1/2}(x). \quad (\text{A.9b})$$

A.2 Properties

A.2.1 Some notable identities

We list some notable recurrence relations:

$$\frac{2\nu}{x} Z_\nu(x) = Z_{\nu-1}(x) + Z_{\nu+1}(x), \quad (\text{A.10a})$$

$$2Z'_\nu(x) = Z_{\nu-1}(x) - Z_{\nu+1}(x), \quad (\text{A.10b})$$

$$Z'_\nu(x) = Z_{\nu-1}(x) - \frac{\nu}{x} Z_\nu(x), \quad (\text{A.10c})$$

$$(x^\nu Z_\nu(x))' = x^\nu Z_{\nu-1}(x), \quad (\text{A.10d})$$

$$Z'_n(x) = \frac{n}{x} Z_n(x) - Z_{n+1}(x). \quad (\text{A.10e})$$

The **Jacobi–Anger expansion** reads

$$e^{ia \sin bx} = \sum_{n=-\infty}^{\infty} J_n(a) e^{inbx}, \quad (\text{A.11a})$$

$$e^{ia \cos bx} = \sum_{n=-\infty}^{\infty} i^n J_n(a) e^{inbx}. \quad (\text{A.11b})$$

A.2.2 Asymptotic behaviour

$$\lim_{x \rightarrow \infty} J_\nu(x) = \sqrt{\frac{2}{\pi x}} \cos(x - \nu\pi/2 - \pi/4), \quad (\text{A.12a})$$

$$\lim_{x \rightarrow \infty} Y_\nu(x) = \sqrt{\frac{2}{\pi x}} \sin(x - \nu\pi/2 - \pi/4), \quad (\text{A.12b})$$

Appendix B

Derivations

We provide derivations relevant for

- Section 2.4 in Appendix B.1,
- Section 4.2.2 in Appendix B.2,
- **blah blah** [...] in Appendix B.3 and
- Section 4.4.2 in Appendix B.4.

B.1 Linearised gravity

Relevant for Section 2.4

DELETE ME: (We go through the derivation of the first order tensor perturbations—the gravitational waves—on a flat FRW background. We begin with the general background metric $g_{\mu\nu}$ and look at perturbations up to second order, $\check{g}_{\mu\nu} = g_{\mu\nu} + \delta^{(1)}g_{\mu\nu} + \delta^{(2)}g_{\mu\nu}$)

[23] **IF TIME:** WRITE THIS (OR REMOVE)!

B.2 Surface tension of thin domain walls

The variation of the quintessence action Eq. (3.8) gives the time-time component of the stress–energy tensor

$${}^{(\phi)}\widetilde{T}^0_0 = \tag{B.1}$$

in the Jordan frame. The surface energy density becomes

$$\sigma = - \int dz. \tag{B.2}$$

We

B.2.1 Symmetron example

B.2.2 Adjusting the boundaries

We assume that $\pm\phi_\infty\check{\chi}$ better tracks the minima than ϕ_\pm . We can change the limits

B.3 Variation of Nambu–Goto action

Following Section 4.2, we have the thin domain wall in four-dimensional expanding, flat spacetime, represented by the hypersurface Σ located at $x^\mu = X^\mu(\xi^a)$, given by

$$X^\mu(\xi^a) = \delta_a^\mu \xi^a + \delta_3^\mu X_\perp, \quad (\text{B.3})$$

where Greek indices take values 0, 1, 2, 3 and Latin a, b, c take 0, 1, 2. Note that Latin indices i, j, k, \dots still represent indices in the spatial sector.

We go about the variation in a slightly less rigorous, yet more intuitive manner. Consider the Nambu–Goto action for the domain wall in expanding spacetime

$$S_{\text{NG}} = - \int_{\Sigma} d^3\xi \sqrt{-\gamma} \sigma, \quad (\text{B.4})$$

where we keep the surface tension generally dependent on time, and the induced metric is

$$\gamma_{ab} = g_{\mu\nu} \partial_a X^\mu \partial_b X^\nu, \quad (\text{B.5})$$

with determinant

$$\gamma \equiv \det(\gamma) = \tilde{\epsilon}^{abc} \gamma_{a0} \gamma_{b1} \gamma_{c2}, \quad (\text{B.6})$$

where $\tilde{\epsilon}$ is the Levi–Civita symbol. For $X_\perp \rightarrow \dot{X}_\perp = X_\perp + \epsilon$, where ϵ is a small perturbation, we get

$$\sqrt{-\gamma} = a^3 \sqrt{1 + \eta_{ab} \partial^a \epsilon \partial_b \epsilon} = a^3 \left\{ 1 + \frac{1}{2} \eta_{ab} \partial^a \epsilon \partial_b \epsilon \right\} + \mathcal{O}(\epsilon^3). \quad (\text{B.7})$$

We vary the action with respect to small changes in ϵ , giving

$$\frac{\delta S_{\text{NG}}}{\delta \epsilon} \delta \epsilon = - \int_{\Sigma} d^3\xi \sigma a^3 \frac{1}{2} [\eta_{ab} \partial^a \epsilon \partial_b (\delta \epsilon)] \cdot 2 + \mathcal{O}((\delta \epsilon)^2) \quad (\text{B.8})$$

With $\partial_a \epsilon \partial_b (\delta \epsilon) = \partial_a (\partial_b \epsilon \cdot \delta \epsilon) - \partial_b \partial_a \epsilon \cdot \delta \epsilon$, where the under-bar signifies that it is not a summation, and vanishing surface terms, we get

$$-\frac{\delta S_{\text{NG}}}{\delta \epsilon} \delta \epsilon = \int d^3\xi \left[-\beta^3 \eta_{ab} \partial^a \partial_b \epsilon + \beta^3 3(\partial_0 \beta / \beta) \partial_0 \epsilon \right] \delta \epsilon, \quad (\text{B.9})$$

where $\beta^3 \equiv \sigma a^3$. The equation of motion becomes

$$\partial_0^2 \epsilon + 3(\partial_0 \beta / \beta) \partial_0 \epsilon - (\partial_1^2 + \partial_2^2) \epsilon = 0. \quad (\text{B.10})$$

B.3.1 Stress–energy tensor

We rewrite the variation

$$\frac{\delta \sqrt{-\gamma}}{\delta g_{\mu\nu}} = \frac{-1}{2\sqrt{-\gamma}} \frac{\delta \gamma}{\delta g_{\mu\nu}}. \quad (\text{B.11})$$

To leading order in ϵ , we get

$$\frac{\delta \gamma}{\delta g_{ab}} = -a^4 \eta_{ab}, \quad \frac{\delta \gamma}{\delta g_{a3}} = -a^4 \partial_a \epsilon, \quad \frac{\delta \gamma}{\delta g_{33}} = 0. \quad (\text{B.12})$$

Inserted into Eq. (4.16), we get

B.4 Fourier space stress–energy tensor: sinusoidal

Relevant for Section 4.4.2

We look at $\mathcal{E}(y) = \sin py$ in $\epsilon = \varepsilon(\tau)\mathcal{E}(y)$.

The trick is to identify the Jacobi–Anger expansion, Eq. (A.12a),

$$f(x) \equiv e^{ia \sin bx} = \sum_{n=-\infty}^{\infty} J_n(a) e^{inbx}. \quad (\text{B.13})$$

We postulate that the Fourier transform $\tilde{f}(\omega) \equiv \int dx \sum_n F_n(x; \omega)$ is

$$\begin{aligned} \tilde{f}(\omega) &= \sum_n J_n(a) \int dx e^{i(\omega+nb)x} \\ &= 2\pi \sum_n J_n(a) \delta(\omega + nb). \end{aligned} \quad (\text{B.14})$$

We assumed that the integration and summation operators commute, which is known to be true for $\int dx \sum_n |F_n(x)| < \infty$ (Fubini’s theorem). **Comment.** For $g(x) \equiv cb \cos bx \cdot f(x) = \frac{1}{2}cb(e^{ibx} + e^{-ibx})f(x)$, we find

$$\begin{aligned} \tilde{g}(\omega) &= \frac{cb}{2} \sum_n J_n(a) \int dx [e^{i(\omega+(n+1)b)x} + e^{i(\omega+(n-1)b)x}] \\ &= \pi cb \sum_n [J_{n+1}(a) + J_{n-1}(a)] \delta(\omega + nb) \\ &= \frac{2\pi cb}{a} \sum_n n J_n(a) \delta(\omega + nb), \end{aligned} \quad (\text{B.15})$$

where in the last line we use the identity XXX.

We use this to find the relevant expressions in Section 4.4.2:

$$I_s = 2\pi \sum_n J_n(k_z \varepsilon) \delta(k_y + np), \quad (\text{B.16a})$$

$$I_a = 2\pi \frac{p}{k_z} \sum_n n J_n(k_z \varepsilon) \delta(k_y + np) = -\frac{k_y}{k_z} I_s, \quad (\text{B.16b})$$

Appendix C

TITLE (Stable Symmetron)

We go through the steps leading to the solution of the asymptotic equation for the symmetron field Eq. (5.5) with the least possible oscillations around the asymptotic true minima χ_{\pm} . We follow Section 5.1.2, and recall that the normal picture in the expanding universe is

$$\chi_w(a, z - z_w) = \chi_{\pm} \tanh\left(\frac{a\chi_+(z - z_w)}{2L_c}\right). \quad (\text{C.1})$$

C.1 Idealised path

- effect on σ, δ
- also initialisation of q

We can rewrite Eq. (5.5) in terms of the time coordinate $\chi_+ = \sqrt{1 - v}$,

$$\frac{d^2\check{\chi}}{d\chi_+^2} - \frac{1}{\chi_+(1 - \chi_+^2)} \frac{d\check{\chi}}{d\chi_+} + m_*^2 \frac{\chi_+^2(\check{\chi}^2 - \chi_+^2)}{(1 - \chi_+^2)^3} \check{\chi} = 0, \quad (\text{C.2})$$

where

$$m_* = \frac{2\mu}{3\mathcal{H}_*(1 + \mathfrak{z}_*)} = \frac{\sqrt{2}a_*^{3/2}}{3\xi_*}. \quad (\text{C.3})$$

The idea is to use this solution as boundary conditions for χ :

$$\chi|_{z \rightarrow \pm\infty} = \pm\check{\chi} \quad \wedge \quad \dot{\chi}|_{z \rightarrow \pm\infty} = \pm\dot{\check{\chi}}. \quad (\text{C.4})$$

This generally alters the blah blah [...] **Maybe rest in appendix?** We solve in two regimes, each solution expanded around $(\text{I}) \chi_+ = 0$ and $(\text{II}) \chi_+ = 1$:

$$\check{\chi}^{(\text{I})} = \chi_* + \frac{C}{2}\chi_+^2 + \frac{C - \chi_*^3 m_*^2}{8}\chi_+^4, \quad (\text{C.5a})$$

$$\check{\chi}^{(\text{II})} = \chi_+ + \frac{8(3 - m_*^2)}{m_*^4}(\chi_+ - 1)^3 + \frac{1440 - 636m_*^2 + 41m_*^4}{2m_*^6}(\chi_+ - 1)^4. \quad (\text{C.5b})$$

We determine χ_* and C by matching these expressions at χ_+^{match} , i.e. solving

$$\begin{aligned} \check{\chi}^{(\text{I})}\big|_{\chi_+ = \chi_+^{\text{match}}} &= \check{\chi}^{(\text{II})}\big|_{\chi_+ = \chi_+^{\text{match}}} \\ \frac{d\check{\chi}^{(\text{I})}}{d\chi_+}\big|_{\chi_+ = \chi_+^{\text{match}}} &= \frac{d\check{\chi}^{(\text{II})}}{d\chi_+}\big|_{\chi_+ = \chi_+^{\text{match}}} \end{aligned} \quad (\text{C.6})$$

The initial conditions best suited for the smallest oscillations possible are given by

$$\check{\chi} = \check{\chi}^{\text{ideal}} \equiv \begin{cases} \check{\chi}^{(\text{I})} & \text{if } \chi_+ \leq \chi_+^{\text{match}}, \\ \check{\chi}^{(\text{II})} & \text{if } \chi_+ \geq \chi_+^{\text{match}}. \end{cases} \quad (\text{C.7})$$

Solving this for the fiducial symmetron parameters $m_* \simeq 268.36$, we get $\chi_* \simeq 0.09656$, $C \simeq 5.837$ and $\chi_+^{\text{match}} \simeq 0.2568$. We update the domain wall profile

$$\chi_w = \check{\chi} \tanh\left(\frac{a\check{\chi}(z - z_w)}{2L_c}\right) \quad (\text{C.8})$$

and in turn the surface tension and thickness

$$\sigma_w = \sigma_\infty \frac{1}{2} (3\chi_+^2 - \check{\chi}^2) \check{\chi} \quad \text{and} \quad a\delta_w = \frac{\delta_\infty}{\check{\chi}}. \quad (\text{C.9})$$

Note that both of these affect the thin-wall analysis in Chapter 4.

C.1.1 Optimal path

We make the distinction [blah blah \[...\]](#)

C.2 Field initialisation

At SSB $\check{\chi} = \chi_*$ and $\check{q} = q_* = a_*^2 3C/\tau_*$. To get the most precise initial configuration, we need to determine the full fields χ and q at $a = a_i \gtrsim a_*$. Note that $\epsilon \neq 0$ in general. Define $u_w = a\check{\chi}(z - z_w)/2L_c$. Now,

$$\chi_{w\#} = \check{\chi} \tanh u_w, \quad (\text{C.10a})$$

$$a^{-2}\tau_* q_{w\#} = \check{\chi}' \tanh u_w + \check{\chi} u_w' \text{sech}^2 u_w, \quad (\text{C.10b})$$

where

$$\check{\chi}' = \chi_+' \frac{d\check{\chi}}{d\chi_+}, \quad (\text{C.10c})$$

$$2L_c u_w' = [a'\check{\chi} + a\check{\chi}'](z - z_w) - a\check{\chi} z_w', \quad (\text{C.10d})$$

and $z_w' = \epsilon' \mathcal{E}$. Similar configuration, $\bar{\chi}_{w\#}$ and $\bar{q}_{w\#}$, is used for the unperturbed anti-wall by substituting $u_w, z_w \rightarrow \bar{u}_w, \bar{z}_w$ and swapping signs. Note that $\bar{z}_w' = 0$.

To assign values to χ and q , we can go through the lattice coordination-wise, “pick” the nearest wall and evaluate the aforementioned expressions at $\tau = \tau_i$. [Maybe figure?!](#) The product scheme (Eq. (3.4)) works as well.